Optimization of GMR Array Sensor based Magnetic Flux Leakage Techniques using Finite Element Modeling

By

WAIKHOM SHARATCHANDRA SINGH

(Enrollment No: PHYS02200704005)

Indira Gandhi Centre for Atomic Research, Kalpakkam

A Thesis submitted to the
Board of Studies in Physical Sciences

In partial fulfillment of requirements
For the degree of
DOCTOR OF PHILOSOPHY
of

HOMI BHABHA NATIONAL INSTITUTE

July, 2013

Homi Bhabha National Institute

Recommendations of the Viva Voce Board

As members of the Viva Voce Board, we certify that we have read the dissertation prepared by **Waikhom Sharatchandra Singh** entitled "**Optimization of GMR Array Sensor based Magnetic Flux Leakage Techniques using Finite Element Modeling**" and recommend that it may be accepted as fulfilling the dissertation requirement for the Degree of Doctor of Philosophy.

____**Date:**

Chairman-**Dr. R. S. Keshavamurthy**

____**Date:**

Guide / Convener-**Dr. B. Purna Chandra Rao**

____**Date:**

Examinar: **Dr. G. Rajaram**

____**Date:**

Member 1-**Dr. G. Amarendra**

____**Date:**

Member 2- **Dr. B. K. Panigrahi**

Final approval and acceptance of this dissertation is contingent upon the candidate's submission of the final copies of the dissertation to HBNI.

CERTIFICATE

I hereby certify that I have read this dissertation prepared under my direction and recommend that it may be accepted as fulfilling the dissertation requirement.

I also certify that the thesis submitted to the examiners has been revised after incorporating their suggestions. The revised thesis has been rebound and submitted to the HBNI for the award of Degree of Doctor of Philosophy.

Guide - **Dr. B. Purna Chandra Rao**

Date:

Place: Kalpakkam

STATEMENT BY AUTHOR

This dissertation has been submitted in partial fulfillment of requirements for an advanced degree at Homi Bhabha National Institute (HBNI) and is deposited in the Library to be made available to borrowers under rules of the HBNI.

Brief quotations from this dissertation are allowable without special permission, provided that accurate acknowledgement of source is made. Requests for permission for extended quotation from or reproduction of this manuscript in whole or in part may be granted by the Competent Authority of HBNI when in his or her judgment the proposed use of the material is in the interests of scholarship. In all other instances, however, permission must be obtained from the author.

(**W. Sharatchandra Singh**)

Date:

Place: Kalpakkam

DECLARATION

I, hereby declare that the investigation presented in the thesis entitled "***Optimization of GMR Array Sensor based Magnetic Flux Leakage Techniques using Finite Element Modeling***" submitted to **Homi Bhabha National Institute (HBNI)**, Mumbai, India, for the award of **Doctor of Philosophy** in **Physical Sciences** is the record of work carried out by me under the guidance of **Dr. B. Purna Chandra Rao**, Head, Non-Destructive Evaluation Division, Metallurgy and Materials Group, Indira Gandhi Centre for Atomic Research, Kalpakkam. The work is original and has not been submitted earlier as a whole or in part for a degree / diploma at this or any other Institution / University.

(**W. Sharatchandra Singh**)

Date:

Place: Kalpakkam

Solely dedicated to my Parents

Shri W. Shangaijaoba Singh

And (Late) Smt. W. Mema Devi

ACKNOWLEDGEMENT

I owe my deep sense of gratitude to my research supervisor and mentor **Dr. B. Purna Chandra Rao,** Head, Non-Destructive Evaluation Division (NDED), Indira Gandhi Centre for Atomic Research (IGCAR) for his whole hearted support, encouragement and guidance during the research work. Without his untiring mentorship, constant inspiration, valuable discussions and suggestions, this thesis wouldn't have been possible. I am deeply obliged to his meticulous planning, effective approach and perfections in all the research works.

I express my sincere gratitude to **Dr. T. Jayakumar**, Director, Metallurgy and Materials Group, IGCAR for his inspiration, encouragement and most importantly providing direction during the course of thesis work. I would like to extend my heartfelt thanks to **Dr. Baldev Raj** and **Shri S. C. Chetal,** the former Directors, IGCAR and **Dr. P. R. Vasudeva Rao,** the present Director, IGCAR for permitting me to pursue research in this reputed centre.

My sincere thanks to my Doctoral Committee members **Dr. R. S. Keshavamurthy, Dr. B. Purna Chandra Rao, Dr. G. Amarendra** and **Dr. B. K. Panigrahi** for regular evaluation of the research work and giving many useful suggestions.

I take this opportunity to thank **Dr. C. K. Mukhopadhyay, Shri S. Mahadevan, Shri S. Thirunavukkarasu, Smt. B. Sasi** and **Shri A. Viswanath**, NDE Division who helped me to learn various technical ingredients for analysis of the results. I am grateful to **Shri P. Krishnaiah** for helping me to wind the coils and to make the magnetisation units. Thanks to all the staffs of NDE Division for all the helpful assistance.

My special thanks to my friend **Dr. Satender Kataria** and his family members for encouragement and precious help to my family, in many times. I also thank to my friends **Dr. S. Ayyapan, Dr. C. Pandian** and **Dr. Satyaprakash Sahoo** for valuable discussions and suggestions during their stay at Kalpakkam. I also would like to acknowledge **Dr. K. Sathpathy**, **Shri Shuaib Ahmed**, **Dr. N. Joyshankar**, **Shri C. Kisan** and **Shri L. Herojit** for their kind helps in many situations.

My appreciation is also offered to my wife **Smt. W. Langlentombi Devi** and daughters **Kum. W. Santirani, Kum. W. Babyrani** and **Kum. W. Kriparani** for their understanding, support and patience during my research work.

(**W. Sharatchandra Singh**)

CONTENTS

		Page No.
Synopsis……………………………………………………………………..		i
List of Figures………………………………………………………………		iii
List of Tables…………………………………………………..………..		xi
List of Abbreviations…………………………………..……………..		xii
List of Publications and Awards…………………………………..……		xv
Chapter 1	**Introduction**…………………………………………...	1
1.1	**Introduction to Nondestructive Testing (NDT)**…………..	1
1.2	**Introduction to Magnetic Flux Leakage (MFL) Testing**……………………………………………………	5
	1.2.1 Working Principle…………………………………...	5
	1.2.2 Capabilities……………………………………….	7
	1.2.3 Applications…………………………………...........	7
1.3	**Magnetisation Techniques in MFL Testing**……………...	9
	1.3.1 Permanent Magnets………………………………	9
	1.3.2 Electromagnets……………………………………...	10
	1.3.2.1 Electromagnetic Yoke………………………	10
	1.3.2.2 Solenoid Coil………………………………..	11
	1.3.2.3 Helmholtz Coils……………………………..	12
	1.3.3 Electric Current……………..………………………	13
1.4	**Magnetic Field Sensors for MFL Testing**………………...	14
	1.4.1 Induction Coils………………………………………..	14

1.4.2 Hall Sensors ……………………………………………… 15

1.4.3 SQUID Sensors ………………………………………….. 16

1.4.4 AMR Sensors …………………………………………….. 16

1.4.5 GMR Sensors …………………………………………….. 17

Chapter 2 Literature Review and Motivation …………….. 21

2.1 Literature Review ………………………………………… 21

2.1.1 Modeling of MFL Testing ………………………….. 22

2.1.1.1 Theoretical Modeling……………………….. 23

2.1.1.2 Numerical Modeling………………………... 28

2.2 Motivation …………………………………………………….. 34

2.3 Objective of the Thesis ……………………………………. 35

2.4 Organization of the Thesis ………………………………... 36

Chapter 3 Finite Element Modeling of MFL Technique …... 38

3.1 Introduction to Finite Element Modeling ………………... 38

3.1.1 Discretization of Domain ……………………………… 39

3.1.2 Selection of Interpolation Functions ………………….. 40

3.1.3 Formulation of System of Equations …………………. 41

3.1.4 Solution of System of Equations ……………………. 41

3.1.5 Post-processing of Data ……………………………….. 42

3.2 Finite Element Modeling of MFL Technique …………… 43

3.2.1 Construction of Model Geometry …………………... 43

3.2.2 Mathematical Formulation …………………………….. 44

3.2.2.1 Governing Equation………………………... 44

3.2.2.2 Boundary Conditions………………………. 48

3.2.3 Meshing…………………………………………….. 49

3.2.4 Solver……………………………………………….. 50

3.2.5 Post-processing and Prediction of GMR Signal….. 51

3.3 Validation of Model…………………………………... 52

Chapter 4 Optimization of MFL Technique for Cuboid Geometry…………………………………………. 55

4.1 Introduction………………………………………………... 55

4.2 MFL Technique for Cuboid Geometry…………………. 57

4.3 Modeling………………………………………………….... 57

4.4 Experimental Setup…………………………………….. 67

4.5 Reference Defects……………………………………….... 68

4.6 Experimental Results…………………………………… 71

4.6.1 Surface Defects……………………………………... 71

4.6.2 Sub-surface Defects……………………………… 73

4.6.3 Influence of Lift-off on MFL Signals………………... 76

4.6.4 Influence of Inclined Defects on MFL Signals……... 76

4.6.5 Influence of Interacting Defects on MFL Signals….. 79

4.6.6 Validation………………………………………… 80

4.7 Development of 2-dimensional 16 Element GMR Array Sensors…………………………………………………... 82

4.8 Conclusions………………………………………………… 84

Chapter 5 Optimization of MFL Technique for Solid Cylindrical Geometry…………………………… 86

5.1 Introduction………………………………………………... 86

5.2 **MFL Technique for Solid Cylindrical Geometry**……….. 89

5.3 **Modeling**……………………………………………………… 90

5.4 **Experimental Setup**……………………………………….. 94

5.5 **Reference Defects**………………………………………… 95

5.6 **Experimental Results**……………………………………… 96

5.6.1 *Local Flaws*………………………………………… 96

5.6.2 *Loss of Metallic Cross-sectional Area*……………… 101

5.6.3 *Validation*…………………………………………… 102

5.6.4 *Comparative Performance of Saddle Coils and Helmholtz Coil Magnetisations*…………………….. 104

5.7 **Development of Flexible 12 Element GMR Array Sensors**…………………………………………………... 106

5.8 **Conclusions**………………………………………………… 110

Chapter 6 **Optimization of MFL Technique for Hollow Cylindrical Geometry**…………………………… 112

6.1 **Introduction**……………………………………………….. 112

6.2 **MFL Technique for Hollow Cylindrical Geometry**……... 116

6.3 **Modeling**……………………………………………………… 117

6.4 **Experimental Setup**……………………………………….. 125

6.5 **Reference Defects**………………………………………… 126

6.6 **Experimental Results**……………………………………… 127

6.6.1 *Localised Defects*…………………………………… 127

6.6.2 *Influence of Support Plate on MFL Signals*………... 131

6.6.3 *Validation*…………………………………………… 133

6.7	**Development of Flexible 5 Element GMR Array Sensors**.	134
6.8	**Conclusions**……………………………………………………	136
Chapter 7	**Generalized Approach Proposed for Model based Optimization**……………………..……….	138
7.1	**Comparative Performance of MFL Techniques for the Three Different Geometries**……………………………….	138
7.2	**Generalized Approach**…………………………………….	140
Chapter 8	**Conclusions**………………………………………………	142
Chapter 9	**Future Work**………………………………………..	145
	References……………………………………………...	147

SYNOPSIS

This thesis presents the three dimensional finite element (3D-FE) model based optimization of magnetic flux leakage (MFL) techniques for high sensitive, fast and reliable non-destructive detection of defects in ferromagnetic components of three different geometries viz. 1) cuboid geometry, 2) solid cylindrical geometry and 3) hollow cylindrical geometry. Carbon steel plates, track ropes of Heavy Water Plant (HWP) and steam generator (SG) tubes of Prototype Fast Breeder Reactor (PFBR) have been considered for cuboid, solid cylindrical and hollow cylindrical geometries, respectively. Experiments have been conducted to confirm the effectiveness of the model based optimization of MFL techniques using giant magneto-resistive (GMR) sensors connected to low-noise differential amplifiers and to develop array sensors for rapid imaging of defects.

Optimization of MFL technique for carbon steel plates (thickness, 12 mm) has been carried out by optimizing the leg spacing, height and magnetizing current of the electromagnetic yoke used in the technique. Confirming experiments have been conducted. GMR sensor with a low-noise differential amplifier have enabled successful detection of a sub-surface notch (depth, 0.9 mm) located at 11.1 mm below the surface. The MFL signal parameters namely, skewness and B_x-B_z locus patterns have been found to be useful for enhanced detection and classification of inclined and interacting defects in cuboid geometry.

MFL technique that uses saddle coils and GMR array sensors has been developed, for the first time, for inspection of track ropes (outer diameter, 64 mm) representing solid cylindrical geometry. The magnetizing current, inter-coil spacing of the saddle coils and locations of GMR sensors between the two coils have been optimized using the 3D-FE model. The experimental results clearly confirmed the reliable detection of both localized flaw (LF) and loss of metallic area (LMA) type defects and resolution (3.2 mm) of multiple flaws in the track rope. Further, a novel flexible 12 element GMR array sensor has been developed and successfully used for rapid imaging to obtain the spatial information of both LF and LMA type defects.

For optimization of MFL technique for testing SG tubes (outer diameter, 17.2 mm and wall thickness, 2.3 mm) using GMR array sensors, the magnetisation unit comprising of two bobbin coils wound on a ferrite core has been optimized for achieving optimum inter-coil spacing of the bobbin coils. The number of GMR sensors and their locations have been optimized by predicting the uniform magnetic flux density region between the two bobbin coils. A 5-element GMR array sensor has been fabricated and the performance of the GMR array sensor has been evaluated for successful detection and imaging of 1 mm diameter localized hole in the tube. The influence of support plate and sodium deposits on the tube outer surface and in defect regions on the MFL signals has been analysed, for the first time.

This thesis finally proposes a generalized approach for optimization of MFL techniques using finite element modeling for enhanced detection and fast imaging of defects in ferromagnetic components, without the need for extensive physical testing.

LIST OF FIGURES

Fig. No.	Fig. Caption	Page No.
Fig. 1.1	A generic NDE system……………………………………..	2
Fig. 1.2	(a) Typical magnetisation curve and (b) ferromagnetic test object with defect illustrating MFL method……………….….	6
Fig. 1.3	Online MFL inspection of pipelines using PIGs……………………………………………………...	8
Fig. 1.4	GMR multilayer structures……………………………………	18
Fig. 1.5	GMR effect……………………………………………………	19
Fig. 2.1	(a) Two-dimensional rectangular defect below the specimen surface and (b) its modified double dipole model…………….	26
Fig. 2.2	Computed leakage magnetic field signals for (a) tangential and (b) normal components of surface and sub-surface slots in ferromagnetic material……………………………………..	26
Fig. 2.3	MFL signal peak-to-peak amplitudes as functions of (a) defect width (length 10 mm, depth 10 mm) in a 14 mm thick plate and (b) defect depth (length 10 mm, width 10 mm) in a 10 mm thick plate at various lift-offs…………………………	31
Fig. 3.1	(a) One-dimensional, (b) two-dimensional and (c) three-dimensional basic finite elements…………………………….	40
Fig. 3.2	3D-FE model geometry for MFL NDE of steel plate………..	44
Fig. 3.3	Typical meshing for 3D-FE modeling of MFL technique of	50

	steel plate………………………………………………………...	
Fig. 3.4	FE model predicted arrow contour plots for (a) surface slot of 3.32 mm depth and (b) sub-surface slot located at 6.24 mm below the measurement surface………………………………	51
Fig. 3.5	Magnetization curve for steam generator tube ….………….	54
Fig. 3.6	Comparison of model predicted and experimentally obtained (a) MFL signals for circumferential notches and (b) its signal peak amplitudes………………………………………………	54
Fig. 4.1	Three different structures of C-core electromagnetic yoke for MFL NDE of cuboid geometry………………………………	58
Fig. 4.2	Model predicted contour lines of B_x component of magnetic flux density from the surface groove for (a) structure 1 (b) structure 2 and (c) structure 3………………………………....	62
Fig. 4.3	Model predicted B_x component of MFL signals for (a) surface groove and (b) sub-surface groove of the three yoke structures…………………………………………………...	62
Fig. 4.4	Model predicted B_x^{peak} amplitudes for surface and sub-surface grooves of the three yoke structures…………………………..	63
Fig. 4.5	Model predicted variation of B_x^{peak} amplitudes with (a) height, (b) leg spacing of yoke, (c) lift-off and (d) plate thickness for the surface and sub-surface groove……………	64
Fig. 4.6	Model predicted B_x^{peak} amplitudes of MFL signals as a function of magnetising current …………………….…..	66

Fig. 4.7	Schematic of experimental setup used for MFL measurements on carbon steel plate…………………………..	67
Fig. 4.8	(a) Functional block diagram of GMR bridge sensor and (b) GMR sensor response characteristic………………………….	68
Fig. 4.9	Carbon steel plate specimen with EDM notches……………..	69
Fig. 4.10	Schematic showing (a) surface notch (near-side) and (b) sub-surface notch (far-side)……………………………………….	71
Fig. 4.11	GMR sensor signal output for various surface notches of (a) 0.5 mm width and (b) 1.0 mm width……………………….....	72
Fig. 4.12	GMR signal amplitude as a function of depth for surface notches (dotted line shows the approximated two-slope behavior)…………………………………………………...	73
Fig. 4.13	GMR sensor signal response for sub-surface notches of (a) 0.5 mm width and (b) 1.0 mm width located at different depths below surface………………………………………….	75
Fig. 4.14	GMR sensor signal amplitude for sub-surface notches as a function of notch location below the surface………………...	75
Fig. 4.15	Variation of GMR signal amplitude with lift-off for different sub-surface notches …………………………………………	76
Fig. 4.16	(a) Measured GMR sensor signal response for inclined notches, (b) parameters determined from the measured MFL signals, (c) signal asymmetry and (d) differential skewness as a function of angle of inclination of notches………………….	79

Fig. 4.17	(a) Measured GMR sensor signal response for interacting notches and (b) ratio of peak amplitudes of outer and inner flanks as a function of notch-to-notch separations……………	80
Fig. 4.18	Comparison between the model and experimentally obtained (a) MFL signal amplitude as a function of notch location below the surface for sub-surface notches and (b) differential skewness as a function of angle of inclination for inclined notches……………………………………………………....	81
Fig. 4.19	(a) Model predicted magnetic flux density between the legs of the electromagnetic yoke (b) the photograph of fabricated 2D array of 4x4 GMR sensors………………………………..	83
Fig. 4.20	(a) 16 element 2D GMR array sensor response for a 3.32 mm deep surface notch and (b) its corresponding MFL image......	84
Fig. 5.1	The cross-section and design details of double locked track rope……………………………………………………………	88
Fig. 5.2	(a) Photograph of the track rope system with bucket carrying coal and (b) local flaws and loss of metallic cross-sectional area on the outer surface of the track rope…………………..	89
Fig. 5.3	Breakage of wires at the outer surface of the track rope……..	89
Fig. 5.4	Three different structures of coil based magnetising unit for MFL NDE of track ropes…………………………………..	90
Fig. 5.5	(a) 3D finite element mesh and model predicted magnetic flux line contours between the two saddle coils for (b)	92

	clockwise and (c) anticlockwise directions of electric currents	
Fig. 5.6	Optimization of (a) magnetising current and (b) inter-coil spacing between the two saddle coils………………………..	94
Fig. 5.7	Experimental setup for the MFL testing of track ropes………	95
Fig. 5.8	Schematic of the track rope having axial and circumferential machined artificial notches………………………………...	96
Fig. 5.9	MFL signals for (a) axial notches and (b) circumferential notches………………………………………………………..	97
Fig. 5.10	FWHM and signal amplitude for axial and circumferential notches………………………………………………………..	98
Fig. 5.11	(a) Photograph of the saw cut in the track rope and (b) the corresponding GMR sensor output…………………………...	99
Fig. 5.12	(a) Photograph of 5 saw cuts (23.2 mm length, 1.0 mm width and 2.0 mm depth) separated by 13.5 mm, 10.0 mm, 5.5 and 3.2 mm distances and (b) the corresponding GMR sensor measured MFL signals……………………………………..	100
Fig. 5.13	Photograph of LMA (42.0 mm length, 9.2 mm width and 3.0 mm depth) machined in the track rope and its GMR sensor response scanned along dotted line *AA* direction……………	101
Fig. 5.14	(a) Model predicted MFL signals from the axial notch, C and the circumferential notch, G and (b) the corresponding experimentally measured GMR sensor response…………….	102
Fig. 5.15	Comparison of model predicted and experimentally measured	103

	(a) normalised MFL signal amplitude of circumferential LFs and (b) MFL signal of LMA………………………………..	
Fig. 5.16	Schematic of Helmholtz coil magnetisation based MFL testing set-up………………………………………………..	105
Fig. 5.17	MFL signals for (a) axial notches and (b) circumferential notches using Helmholtz coil magnetisation…...…………….	106
Fig. 5.18	(a) Model predicted magnetic flux density between the saddle coils along half of circumferential distance and (b) the fabricated flexible sensor array of 12 GMR sensors…………	107
Fig. 5.19	Photographs of (a) axial LF, (b) circumferential LF, (c) axial LMA and (d) circumferential LMA type defects in the track rope…………………………………………………………	108
Fig. 5.20	GMR sensor array response for a 5.5 mm long circumferential LF………………………………………….	108
Fig. 5.21	MFL images for (a) axial and (b) circumferential LFs……….	109
Fig. 5.22	MFL images of (a) axial LMA (42.0 x 9.0 x 3.0 mm^3) and (b) circumferential LMA (33.5 x 14.2 x 4.9 mm^3)……………….	110
Fig. 6.1	(a) Schematic of steam generator and (b) photograph of tube bundle assembly……………………………………………	113
Fig. 6.2	MFL technique proposed for small diameter SG tubes of hollow cylindrical geometry………………………………….	117
Fig. 6.3	Three different core structures of bobbin coils based magnetising unit for MFL NDE of small diameter hollow	119

	cylinder……………………………………………………….	
Fig. 6.4	Surface and arrow plots of magnetic flux density from a 1.15 mm deep OD notch for (a) air core, (b) ferrite core and (c) ferrite core with flux guide (d) air core (near defect), (e) ferrite core (near defect) and (f) ferrite core with flux guide (near defect)……………………………..………………...	121
Fig. 6.5	Model predicted B_a component of MFL signals for (a) ID notch and (b) OD notch of three magnetising coil structures...	122
Fig. 6.6	Model predicted B_a^{peak} amplitudes of MFL signals for ID and OD notches of three magnetising coil structures……………..	123
Fig. 6.7	Optimization of (a) inter-coil spacing between the two bobbin coils and (b) magnetising current…………………………….	124
Fig. 6.8	(a) Experimental setup for MFL testing of SG tube and (b) photograph of GMR sensor based MFL probe………………	126
Fig. 6.9	GMR sensor response for outer side (a) EDM circumferential notches, (b) flat bottom holes and (c) through holes in SG tube…………………………………………………………	129
Fig. 6.10	GMR sensor signal amplitude as a function of volume of defects…………………………………………………...	130
Fig. 6.11	(a) Photograph of the SG tube with support plate (Inconel-718) and (b) comparison of experimentally obtained and model predicted MFL signals for a 1.08 mm diameter hole in tube with and without the support plate……………………..	132

Fig. 6.12	Model predicted contour plots of magnetic flux density (a) with and (b) without the support plate………………………..	133
Fig. 6.13	Comparison of experimentally obtained and model predicted MFL signal amplitude of circumferential notches.	134
Fig. 6.14	(a) Model predicted magnetic flux density between the two bobbin coils (b) the photograph of fabricated flexible array of 5 element GMR sensors………………………………………	135
Fig. 6.15	Response of 5 element GMR array sensor for through holes of 1.1, 2.0, 2.8 and 3.1 mm diameter………………………....	135
Fig. 7.1	Flowchart of the generalized approach for model based optimization of MFL techniques………………………..….....	141

List of Tables

Table No.	Table Caption	Page No.
Table 1.1	Comparison of commonly used sensors in MFL testing….	19
Table 3.1	Parameters used in the FE modeling……………………….	53
Table 4.1	Parameters used in the FE modeling of MFL technique for carbon steel plate………………………………………...	59
Table 4.2	Details of surface and sub-surface notches in 12 mm thick carbon steel plates……………………………………….	70
Table 5.1	Details of artificial EDM notches machined in the track rope (length 5.5 mm and width 2.0 mm)…………………...	96
Table 6.1	Parameters used in the FE modeling of MFL technique…..	119
Table 6.2	Depths of reference defects in SG tubes…………………...	127
Table 7.1	Comparative performance of MFL techniques for the three different geometries………………………………………..	139

List of Abbreviations

Symbol	Abbreviation
1D, 2D, 3D	One-dimension, two-dimension, three-dimension
Φ	Magnetic flux
σ	Surface magnetic charge density
ρ	Volume magnetic charge density
μ_0	Magnetic permeability of free space
μ_r	Relative permeability
a_0, a_1	Coefficients
A	Magnetic vector potential
A_x, A_y and A_z	Components of vector potential
AC	Alternating current
AMR	Anisotropic magneto-resistive
AST	Above ground storage tank
{b}	Global source vector
$\{b_x^e\}$, $\{b_y^e\}$, $\{b_z^e\}$	Vectors of an element e
B_x, B_y, B_z	Tangential, circumferential and normal components of leakage flux density
B_x^{peak}, B_z^{peak}	MFL peak amplitudes
B_{xl}^{peak} - B_{xr}^{peak}	Difference in peak amplitudes w. r. t. left and right minima
BEM	Boundary element method
CG	Conjugate gradient
DC	Direct current
ECT	Eddy current testing
EDM	Electro-discharge machining
$F(A)$	Functional
FDM	Finite difference method
FE	Finite element
FEM	Finite element method
FGMRES	Flexible generalised minimum residual

FWHM	Full width at half maximum
GMR	Giant magneto-resistive
GMRES	Generalised minimum residual
h	Defect location below the specimen surface
h_y	Height of yoke
H_0	Applied magnetic field
H_x, H_z	Tangential and normal components of leakage field intensity
H_s^*	Effective magnetic field in the specimen
HWAC	Half wave rectified current
HWP	Heavy water plant
I	Magnetising current
ID	Internal diameter
ILI	In-line inspection
IRIS	Internal rotary ultrasonic inspection
ISI	In-service inspection
J	Current density
[K]	Global matrix (or stiffness matrix)
$[K_{xx}^e]$, $[K_{xy}^e]$, $[K_{xz}^e]$	Matrices of an element e
LF	Local flaws
LMA	Loss of metallic cross-sectional area
LPT	Liquid Penetrant testing
M	Magnetisation
MFL	Magnetic flux leakage
MPT	Magnetic particle testing
MR	Magneto-resistive
N	Number of copper winding turns
N_j^e	Interpolation function of element e at node j
NDE	Non-destructive evaluation
NDT	Non-destructive testing
NVE	Non volatile electronics

OD	Outer diameter
PCB	Printed circuit board
PFBR	Prototype fast breeder reactor
PIG	Pipe inspection gauge
PSEC	Partial saturation eddy current
R_H	Hall coeffcient
RFEC	Remote field eddy current
RMS	Root mean square error
RT	Radiographic testing
s_c	Inter-coil spacing of bobbin coils
s_s	Inter-coil spacing of saddle coils
s_y	Leg spacing of yoke
SG	Steam generator
SQUID	Superconducting quantum interface device
SNR	Signal-to-noise ratio
UT	Ultrasonic testing
V_H	Hall voltage
VT	Visual testing
WT	Wall thickness

List of Publications

Publications in Journals

1. **W. Sharatchandra Singh**, B. P. C. Rao, S. Thirunavukkarasu, C. K. Mukhopadhyay and T. Jayakumar, "Design and optimization of GMR array based magnetic flux leakage probe for imaging of defects in small diameter steam generator tubes", Sensors and Actuators A (Communicated).

2. **W. Sharatchandra Singh**, B. P. C. Rao, S. Thirunavukkarasu, C. K. Mukhopadhyay and T. Jayakumar, "GMR based magnetic flux leakage technique for detection of localized outer side defects in small diameter ferromagnetic steam generator tubes", IEEE Transactions on Magnetics (Communicated).

3. **W. Sharatchandra Singh**, B. P. C. Rao, S. Thirunavukkarasu and T. Jayakumar, "Flexible GMR sensor array for magnetic flux leakage testing of steel track ropes", Journal of Sensors, vol. 2012, article ID 129074, 6 pages, March 2012.

4. **W. Sharatchandra Singh**, B. P. C. Rao, S. Thirunavukkarasu, S. Mahadevan, C. K. Mukhopadhyay and T. Jayakumar, "3-D finite element modeling of leakage magnetic fields from inclined cracks in carbon steel plates", Studies in Applied Electromagnetics and Mechanics, Electromagnetic Nondestructive Evaluation (XV), vol. 36, pp. 175-182, January 2012.

5. **W. Sharatchandra Singh**, B. P. C. Rao, C. K. Mukhopadhyay and T. Jayakumar, "GMR based magnetic flux leakage technique for condition monitoring of steel track rope", Insight, vol. 53, no. 7, pp. 377-381, July 2011.

6. **W. Sharatchandra Singh**, B. P. C. Rao, S. Mahadevan, T. Jayakumar and Baldev Raj, “Giant magneto-resistive sensor based magnetic flux leakage technique for inspection of track ropes”, Studies in Applied Electromagnetics and Mechanics, Electromagnetic Nondestructive Evaluation (XIV), vol. 35, pp. 256-263, June 2011.

7. **W. Sharatchandra Singh**, B. P. C. Rao, T. Jayakumar and Baldev Raj, “Simultaneous measurement of tangential and normal components of leakage magnetic flux using giant magneto-resistive sensors”, Journal of Non-Destructive Testing & Evaluation, vol. 8, no. 2, pp. 23-28, September 2009.

8. **W. Sharatchandra Singh**, B. P. C. Rao, S. Vaidyanathan, T. Jayakumar and Baldev Raj, “Detection of leakage magnetic flux from near-side and far-side defects in carbon steel plates using giant magneto-resistive sensor”, Measurement Science and Technology, vol. 19, no. 1, 015702 (8pp), January 2008.

Conference Proceedings

1. **W. Sharatchandra Singh**, B. P. C. Rao, C. K. Mukhopadhyay and T. Jayakumar, “Giant magneto-resistive sensor array for non-destructive detection of leakage magnetic flux from surface defects in ferromagnetic materials”, International Conference On Sensors and Related Networks (SENNET 12), VIT University, India, pp. 71-73, January 2012.

2. **W. Sharatchandra Singh**, S. Thirunavukkarasu, S. Mahadevan, B. P. C. Rao, C. K. Mukhopadhyay and T. Jayakumar, “Three-dimensional finite element modeling of magnetic flux leakage technique for detection of defects in carbon steel plates”, Proc. of COMSOL Conference-2010, Bangalore, India, October 2010 (CD released).

3. **W. Sharatchandra Singh**, K. Krishna Nand, B. P. C. Rao, T. Jayakumar and Baldev Raj, "Magnetic flux leakage NDE using giant magneto-resistive sensors", Review of Progress in Quantitative NDE, AIP Press, vol. 27B, pp. 857-864, March 2008.

4. **W. Sharatchandra Singh**, B. P. C. Rao, B. Sasi, S. Vaidyanathan, T. Jayakumar and Baldev Raj, "Giant magneto-resistive sensors for non-destructive detection of magnetic flux leakage from sub-surface defects in steels", International Conference On Sensors and Related Networks (SENNET 07), VIT University, India, pp. 11-14, December 2007.

Awards

1. **Best oral presentation award** for presenting a paper entitled "Three-dimensional finite element modeling of magnetic leakage flux from inclined and interacting defects", W. Sharatchandra Singh, S. Thirunavukkarasu, S. Mahadevan, B. P. C. Rao, C. K. Mukhopadhyay and T. Jayakumar, NDE Seminar-2010, Kolkata, India, December 2010.

2. **Best oral presentation award** for presenting a paper entitled "Three-dimensional finite element modeling of magnetic flux leakage technique for detection of defects in carbon steel plates", W. Sharatchandra Singh, S. Thirunavukkarasu, S. Mahadevan, B. P. C. Rao, C. K. Mukhopadhyay and T. Jayakumar, COMSOL Conference-2010, Bangalore, India, October 2010.

Chapter 1: Introduction

1.1 Introduction to Non-Destructive Testing

Assessment of structural integrity of engineering components and structures in many industries is essential for ensuring their safe and economical operations. In general, components and structures fail due to the presence and growth of inherent or service-induced defects. Sometimes failures can occur without any prior notice. This has motivated the search for techniques for detection and quantitative characterization of defects to take corrective actions to prevent failures of catastrophic consequences. Very often, assessment of structural integrity of a component is performed through mechanical destructive tests which measure properties such as hardness, tensile strength and ductility. However, inspection of installed components such as steam generator (SG) in nuclear plants, pipelines in petrochemical industries, etc. demands techniques that are non-destructive.

Non-destructive testing (NDT) is a branch of material science that deals with the assessment of soundness and structural integrity of a component or structure through detection of defects without causing any damage to it [1-2]. This mere detection of defects is not sufficient to take the decision of acceptance/rejection of the component. This has lead to the emergence of non-destructive evaluation (NDE) as a new discipline which does detection as well as quantification of defects with respect to its shape, size, location, and orientation. NDE also involves characterization of microstructures, residual stresses and degradation of mechanical properties of components or structures.

NDE is being routinely used in nuclear power plants, transportation, aerospace and petrochemical industries to ensure reliability, safety and structural integrity of critical components such as heat exchangers, railroads, aircraft engines, wire ropes, gas pipelines and others where failures can effect availability factors, productivity and profitability[3-4]. The NDE of installed critical components is becoming increasingly important for both safety and economic reasons. There is a tremendous demand for new and improved NDE techniques that are efficient, reliable and economical to use in many industries.

Figure 1.1 shows a generic NDE system consisting of a specimen under test, an excitation source and a receiving sensor array. The excitation source interacts with the test specimen. If any defect is present in the specimen, the interaction of the field is different for defective and healthy regions of the specimen. This difference in interaction response is measured using the sensor array. The sensor array output in the form of signals or images is further analyzed using signal or image processing techniques to display the useful information of the defect.

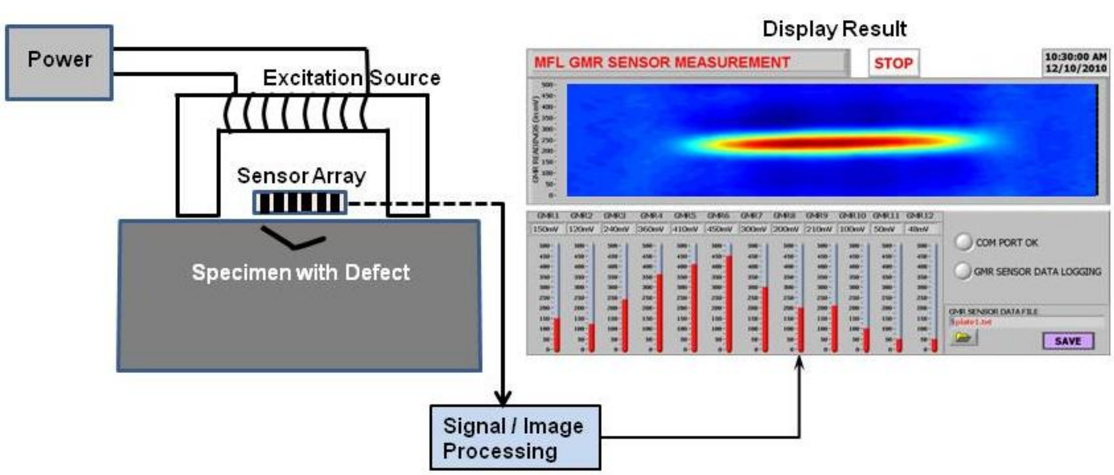

Figure 1.1 A generic NDE system.

There are several established NDE methods which are based on various physical principles. Commonly used NDE methods include the following:

- ❖ Visual Testing (VT)
- ❖ Liquid Penetrant Testing (LPT)
- ❖ Ultrasonic Testing (UT)
- ❖ Radiographic Testing (RT)
- ❖ Eddy Current Testing (ECT)
- ❖ Magnetic Particle Testing (MPT)

Among these methods, visual testing is the oldest and the least expensive method which is generally used as the first step for assessing the overall general health of a component and for detection of surface-breaking defects. A variety of aids such as magnifying glass, fibrescopes, cameras and video equipments are often used to enhance the capability of VT method. The basic principle of liquid penetrant testing is to increase the visibility contrast between defect and background by applying a liquid of high mobility and penetrating power to the region of interest, and then allowing the liquid to emerge from the developer to reveal the defect pattern under white light or ultraviolet light. The LPT method is applicable to all types of materials and component geometries. Ultrasonic testing uses high frequency (0.5 - 25 MHz) sound waves to detect imperfections or changes in material properties within a specimen. It is a volumetric technique and can detect cracks, laminations, shrinkage, cavities, pores and inclusions in plates, pipes, welds, castings and forgings [5]. Radiographic testing uses an x-ray tube or radioactive isotope as a source of radiation which passes through the material and captures the radiation on a film or digital device placed on the opposite side. Possible imperfections are identified in radiographic images through density changes. RT is widely used for volumetric inspection of castings, welds, bonded structures and composite materials. Eddy current testing method works on the principle of electromagnetic induction and measures changes in coil impedance due to variations in electrical conductivity and magnetic permeability in metallic materials. ECT method is widely used for materials sorting, defect detection in tubes, sheets and rods and coating thickness measurements [6-8]. It is also possible to assess heat treatment adequacy and microstructure degradation [6]. In magnetic particle testing (MPT) method, the test component is magnetised and local magnetic flux leakage due to presence of defects is detected using fine magnetic particles [9]. MPT is widely used for inspection of cracks in crankshafts, fly wheels, crank hooks in transportation industries, butt welds of pressure vessels and steam turbine rotors in power plants, etc. [5, 9]. However, it fails to test parts such as inner diameter defects of long tubes and pipes etc., which are not easily accessible for visual examination [10]. Often demagnetisation and cleaning of the object is required after carrying out the MPT. It does not provide permanent and quantitative records of inspection and its capability is limited for detection of sub-surface defects located beyond 5 mm from surface.

Selection of NDE method is important. The material, component geometry, characteristics of the expected defects, manufacturing process, environment surrounding the component, accessibility, and cost as well as capability of the method are all important factors which decide the NDE method to be used for a particular application [8]. Apart from improving the existing NDE techniques, newer techniques are also being constantly researched and developed to solve the increasing demands on quality, safety and stringent specifications of critical components and newly developed materials. The effectiveness and efficiency of many established NDE techniques have been enhanced by modeling, better sensor technologies and novel signal and image processing methodologies.

1.2 Introduction to Magnetic Flux Leakage Testing

Magnetic flux leakage (MFL) method is the advance form of magnetic particle testing and in this method magnetic field sensors are used, in place of magnetic particles, to enable permanent and quantitative recording of leakage magnetic fields. Further, the use of sensors enables incorporation of the latest advances in the magnetic field sensing devices for enhancing the detection sensitivity of the existing MFL technique for the detection and sizing of defects in ferromagnetic materials. The working principle, capabilities and applications of MFL testing for different geometries are given in the following sections:

1.2.1 Working Principle

In MFL method, the test object is uniformly magnetised close to magnetic saturation in magnetisation curve (Fig. 1.2a). If any defect is present in the object, the magnetic permeability is reduced at the defect region and this causes the distortion of magnetic field lines around the defects and leaking some of the magnetic fields out of the object as shown in Fig. 1.2(b). The leakage field is measured using a sensor or sensor arrays by scanning the object surface. The leakage field components in three directions viz.

tangential, B_x (along the measurement surface and perpendicular to the length of defect), circumferential, B_y (along the measurement surface and parallel to the length of defect) and normal, B_z (perpendicular to the measurement surface) can be measured, although in practice only one component is usually measured [10]. The sensor output is used to estimate the shape and size of the defect [7]. Apart from defects, stress and lift-off (spacing between MFL system and object surface) and velocity of MFL system influence the sensor output.

Success of MFL testing method depends on the following:

- proper magnetisation of object
- detection of leakage flux using a suitable sensor
- processing raw data to enhance signal-to-noise ratio (SNR) and
- interpretation of test results

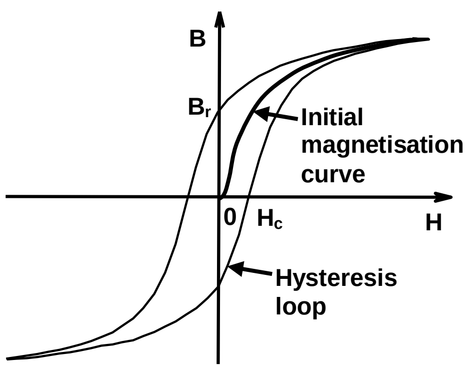

(a)

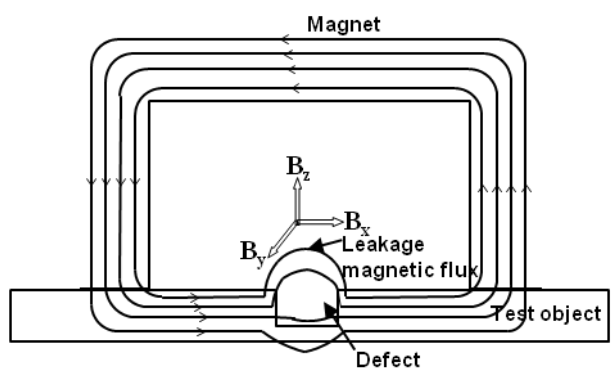

(b)

Figure 1.2 (a) Typical magnetisation curve and (b) leakage magnetic flux from a defect in ferromagnetic test object.

1.2.2 Capabilities

MFL method provides a high degree of certainty for detection of localized surface or near-surface defects in ferromagnetic materials, even on rough surfaces methods [2]. It is capable of detecting corrosion, cracks, gouges and dents in pipelines and storage tank floors. Automated MFL testing is possible in production line, due to the use of sensor, to ensure the quality and uniformity of final products such as steel blooms, billets, rods, tubes and bars during manufacturing [3]. It is also possible to reconstruct defect profiles from the measured sensor output using inversion techniques [11-12]. However, MFL signal is influenced by stress and velocity of the MFL unit.

1.2.3 Applications

MFL method is widely used in industry for assessing the quality and structural integrity of ferromagnetic objects such as underground oil and gas pipelines, oil-storage tank floors, wire ropes, etc. [2, 13-14] of different geometries. MFL is commonly used in-line inspection technique for finding metal-loss regions in oil and gas transmission pipelines [15-16]. About 80% of the pipeline inspection is carried out using the MFL method. Pipe Inspection Gauge (PIG) is commonly used for this purpose (Figure 1.3). The PIG is propelled inside the pipe under the pressure of natural gas or fluid. A strong permanent magnet or electromagnet in the PIG nearly saturates the pipe wall. Defects distort the applied field, producing the flux leakage. An array of Hall sensors is placed around the circumference of the pipe to measure the leakage flux. The measured data is acquired and stored in a computerized data acquisition system and subsequently analyzed. MFL method can reliably detect metal loss due to corrosion and, sometimes, gouging in the gas-pipelines.

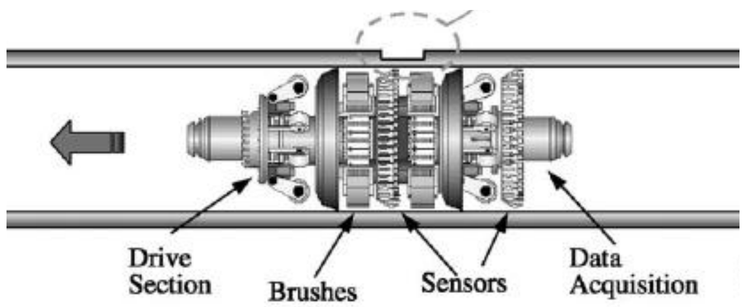

Figure 1.3 Online MFL inspection of pipelines using PIGs [16].

MFL method is also found to use in petrochemical and refinery industries for detecting flaws in cuboid geometry components such as carbon steel plates, storage tank floors, etc. [17-18]. Carbon steel plates are also used in the flooring of above ground storage tanks (AST) [17]. MFL for the inspection of AST floors was proposed in 1988 by Saunderson [18]. MFL method can reliably detect metal-loss defects or remaining wall thickness due to corrosion in tank floors [19-20].

Another application of MFL method is the inspection of wire ropes, of solid cylindrical geometry, which are used for material handling in mines and hauling of men in ski-lift operations [21-23]. MFL method can detect both types of defects viz. local flaw (LF) and loss of metallic cross-sectional area (LMA) which are generally occurred during service due to corrosion, abrasion and wear [21].

MFL method is also used in production line to ensure the quality and uniformity of final products such as steel blooms, billets, rods, tubes and bars during manufacturing time [24-25]. Several MFL devices viz. rotomat, tubomat and discomat systems employing rotating magnetising yokes and Hall sensor array are used for the automatic testing of tubes of diameters ranging from 10 to more than 500 mm [25]. All these devices are used for testing of tubes from outside of the tubes.

1.3 Magnetisation Techniques in MFL Testing

MFL testing of objects requires optimisation of the following:

- permanent magnets
- electromagnets
- electric current

1.3.1 Permanent Magnets

Permanent magnets are widely used in MFL testing especially, for inspection in underwater environments or other areas, such as explosive environments, where electromagnets cannot be used. Commonly used permanent magnets are bar magnets and horseshoe magnets which are made up of Neodymium Iron Boron (NdFeB) and Samarium Cobalt (SmCo) with high energy products. Among the permanent magnets, NdFeB can generate maximum magnetic fields (upto 1.43 T) [26]. They are low-cost, portable in size and they do not need external excitation energy for their operation. However, their use in MFL testing is limited due to lack of control of field strength and the difficulty in placing and removing strong permanent magnets from the component being tested. Another disadvantage with permanent magnets is that the magnetisation cannot be turned off when desired. As a result, they are least flexible among the magnetisation techniques [2].

1.3.2 Electromagnets

Several electromagnets such as electromagnetic yoke, solenoid and Helmholtz coils are extensively used depending upon the geometry and accessibility of the components. The magnitude of magnetising current can be varied so as to produce a wide range of induced flux density required depending upon the thickness of the test component, size and location of defects. Among the magnetisation techniques, electromagnets have the most flexibility to suit the geometry of the test components. However, it is essential to ensure good coupling with the component for better detection sensitivity and reliability when electromagnets are used. The different types of electromagnets commonly used in MFL testing are briefly discussed below:

1.3.2.1 Electromagnetic Yoke

Electromagnetic yoke consists of a soft iron C-core around which copper wire is uniformly wound. A strong longitudinal magnetic field between the north and south poles of the magnet is generated when electric current flows through the copper wire. A typical electromagnetic yoke can generate magnetic field upto 2 T [27]. Yokes with adjustable legs are commonly used in MFL testing for inspection of irregular shaped components and welds [28]. A switch is generally included in the electrical circuit so that the current and, therefore, the magnetisation can be turned on and off conveniently. The yokes can be powered with alternating current from a wall socket or with a battery pack.

Suppose L, A and μ are the magnetic path length, area of cross-section and relative permeability respectively of a specimen. Let N be the number of turns of copper wire carrying a current I. Then, the total magnetic force in the magnetic circuit of a yoke placed over the specimen with an air gap is given by [3],

$$NI = \frac{\Phi}{\mu_0}\left(\frac{L_s}{\mu_s A_s} + \frac{L_c}{\mu_c A_c} + \frac{L_a}{A_a}\right) \tag{1.1}$$

where the subscripts represent the test specimen (s), core (c) of the yoke and air gap (a) between the magnetising yoke and specimen surface. In ideal case where reluctances of the core and air gap are both zero, the effective magnetic field H_s^* in the test specimen is given by,

$$H_s^* = \frac{NI}{L_s} = \frac{\Phi}{\mu_0 L_s}\left(\frac{L_s}{\mu_s A_s} + \frac{L_c}{\mu_c A_c} + \frac{L_a}{A_a}\right) \tag{1.2}$$

Generally, industrial yokes are designed to provide at least 30-40 Oe tangentially at the surface of the specimen, midway between the legs [3]. This region of uniform surface field between the two legs can be checked by a gaussmeter. One important aspect with yokes is heating of coil at prolonged use as well as due to use of higher amperage.

1.3.2.2 Solenoid Coil

A solenoid is made by winding a large number of turns of insulated copper wire in a helical fashion on an elongated former. Solenoids are often cylindrical in shape and hence, they are suited for testing of cylindrical objects. When the length of a component is several times larger than its diameter, an axial magnetic field can be established in the component. If L is the length of the solenoid, D the diameter, I the current in the winding of *N* turns and *x* the distance from the centre of the solenoid, then the magnetic field at *x* is given by [27]

$$H = \left(\frac{NI}{L}\right)\left[\frac{(L+2x)}{2[D^2+(L+2x)^2]^{1/2}} + \frac{(L-2x)}{2[D^2+(L-2x)^2]^{1/2}}\right] \tag{1.3}$$

At the centre of the solenoid *x*=0 and hence

$$H_{centre} = \left(\frac{NI}{L}\right)\left[\frac{L}{(L^2+D^2)^{1/2}}\right] \tag{1.4}$$

For infinitely long (L is greater than at least 7 times the D) solenoid where L>>D and $(L^2 + D^2)^{1/2} = L$, the above equation (1.4) reduces to

$$H_{centre}(\infty) = \left(\frac{NI}{L}\right) \tag{1.5}$$

At the end of the solenoid, the field is equal to half the value of the solenoid at the centre.

When a cylindrical component with considerable length is magnetised using a solenoid, it is possible to obtain uniform axial magnetisation within and very near to the solenoid and MFL sensor is placed in this region [27]. At some distance from the solenoid, the magnetic lines of force will deviate from the axial direction and field sensing sensors would not be usually placed in this region.

1.3.2.3 Helmholtz Coils

A pair of Helmholtz coils can also be used to generate a fairly uniform axial field over a large volume of space in a component. They consist of two circular coils of the same radius and number of turns on a common axis and separated by a distance equal to the radius of the coil. The current flowing through the two coils of Helmholtz coils is in the same direction. Let *I* be the current flowing in each coils of *N* turns and radius *a* separated by a. Then, the axial component of magnetic field intensity at an axial point whose distance is x, is given by [3]

$$H = \left(\frac{NIa^2}{2}\right)\left[\frac{1}{(x^2+a^2)^{3/2}} + \frac{1}{\{(a-x)^2+a^2\}^{3/2}}\right] \tag{1.6}$$

At the middle of the Helmholtz coils, $x = a/2$ the axial component of magnetic field becomes

$$H = \left(\frac{NIa^2}{2}\right)\left[\frac{1}{\left(\frac{a^2}{4}+a^2\right)^{3/2}} + \frac{1}{\left(\frac{a^2}{4}+a^2\right)^{3/2}}\right] = \frac{0.7155NI}{a} \tag{1.7}$$

The radial component of magnetic field along axial direction is zero due to the symmetry. The axial component of magnetic field close to the centre of Helmholtz coils is also very weakly dependent on the radial distance from the axis. Therefore, the magnetic field strength is maintained fairly constant over a large volume of space between the two coils [3, 28]. The useful region of uniform field between the two coils can also be increased by making the coil spacing slightly larger than their common radius. Helmholtz coils are suited for magnetisation of cylindrical components.

1.3.3 Electric Current

Electric current can also be used for magnetisation of components through either directly injecting current into the components or indirectly sending current to separate conductors such as prods and central conductors. Various types of electric current sources such as direct current (DC), alternating current (AC), half wave rectified current (HWAC), etc. are used to obtain the required magnetisation of the part being inspected [9]. The direction of electric current should be in such a way that the presence of a discontinuity distorts the current flow as much as possible. Bars, billets and tubes are often magnetised with a direct electric current [2]. Prods, usually made from thick copper, are used for weld testing. Central conductors are used for circumferential magnetisation of hollow cylindrical tubes. The central conductors are usually solid copper bars and they are placed inside the tube to generate circular magnetic fields.

In all the magnetisation techniques, it is necessary to ensure that the magnetisation is perpendicular to the expected orientation of defects so as to get maximum leakage field at the object surface.

1.4 Magnetic Field Sensors for MFL Testing

Commonly used magnetic field sensors in MFL testing are induction coils and Hall sensors [29-31]. Coils measure the rate of change of a magnetic field, while Hall sensors measure the actual magnetic field strength. SQUID (Superconducting Quantum Interface Device) [32-33], anisotropic magneto-resistive (AMR) [34-35] and giant magneto-resistive (GMR) [36-37] sensors are also found to use in MFL testing. The characteristics and suitability of these magnetic sensors for MFL testing are discussed below:

1.4.1 Induction Coils

Induction coils consist of some turns of insulated copper wire wrapped around a core. When an induction coil is scanned across the defect, the magnetic flux linking with the coil changes and a voltage is induced across the terminals of the coil. This output voltage (E) is proportional to the number of turns (N) in the coil and the time rate of change of flux ($d\varphi/dt$) linking with the coil as given below:

$$E = -N\frac{d\varphi}{dt} = -NA\frac{dB}{dx}\frac{dx}{dt} \tag{1.8}$$

where A is the cross-sectional area, B is the flux density and x is the distance moved by the coil. Thus, the voltage induced in the coil is proportional to the gradient of flux density along the direction of coil motion and the speed at which coil moves. Induction coils are cheap, easy to manufacture and adaptable to any geometry. They do not require any excitation and also not saturate even at quite large magnetic field levels [3]. But, they are less sensitive and possess poor resolution. They also require encapsulation to minimize the *eddy current* effects.

1.4.2 Hall Sensors

Hall sensors are the most commonly used magnetic field sensors in MFL testing [38-39]. The fabrication material of Hall sensors is specially grown semiconductor such as indium arsenide, indium antimony, gallium arsenide or silicon. It works on the principle of *Hall Effect*. When a current I_x carrying semiconductor is placed perpendicular to the direction of an externally applied magnetic field B_z, a voltage V_H will be generated perpendicular to both the current and field given by

$$V_H = R_H I_x B_z / t \tag{1.9}$$

where R_H is the Hall coefficient that depends upon the charge carriers and t is the thickness of the semiconductor. Hall sensor measures the component of magnetic field perpendicular to its chip plane. Typical sensitivity of Hall sensors are 100-600 mV/T with excitation AC currents around 100 mA [40]. Their attractive features for MFL testing include high linearity, small size, low-cost, operate at room temperature, and possibility to fabricate sensor arrays for rapid inspection. Compared to induction coils, Hall sensors have very small active sensing area, so that they approximate to point sensors [3]. However, they suffer from less sensitivity and large offset [41].

1.4.3 SQUID Sensors

SQUID (Superconducting Quantum Interface Device) sensor consists of a superconducting ring closed by a Josephson junction. It works based on flux quantization in superconducting rings and the Josephson Effect [42]. Among the magnetic field sensors, SOUIDs has the highest sensitivity and can detect magnetic fields of a few fT. It enables measurement of weak magnetic fields even without applying a very large magnetising field [43]. It has the potential for detection of discontinuities, material degradations in materials even at large lift-offs [44]. However, it is necessary to use cryogenic liquid, generally liquid nitrogen and scan the cryostat to get the signals, if the object can not be moved. Further, SQUIDs cannot be used for applications in small diameter tubes.

1.4.4 AMR Sensors

Anisotropic magneto-resistance (AMR) sensors consist of thin ferromagnetic films (e.g. permalloy) with a magnetic anisotropy. The application of an external magnetic field will rotate the magnetisation with a resulting change in resistance. The resistance changes roughly as the square of the cosine of the angle between the magnetisation and the direction of current flow [34].The magneto-resistive (MR) ratio for AMR materials is typically a few percent (3-4%) [45]. They have the advantages of less noise as compared to GMR sensors. However, their output may flip or reverse at higher magnetic fields.

1.4.5 GMR Sensors

Giant magneto-resistance (GMR) is a quantum mechanical magneto-resistance effect observed in a few nm thick multilayer structures such as Fe/Cr/Fe, Co/Cu/Co, etc. in which ferromagnetic layers are separated by non-magnetic layers (Figure 1.4). The Nobel Prize for the year 2007 in physics was awarded to Albert Fert and Peter Grünberg for their discovery of GMR effect [46]. The GMR sensors work based on the GMR effect in which there is a large change in electrical resistance to an applied magnetic field due to the spin dependent scattering of electrons [47-48]. Ferromagnetic materials have two types of electrons viz. spin up electrons and spin down electrons as carriers. Spin up electrons are those electrons whose magnetic moments are parallel to the direction of magnetisation of the material while spin down electrons have magnetic moments antiparallel to the direction of magnetisation. The population of spin up electrons is higher than the population of spin down electrons. It is more difficult for a spin down electron to act as a carrier in the ferromagnetic film. This is the fundamental reason for different surface scattering of spin up and spin down electrons of magnetic materials used in GMR structures [49].

In order to exhibit the GMR effect, the mean free path of conduction electrons has to greatly exceed the thickness of thin films. The mean free path of electrons in many ferromagnetic alloys is on the order of 10 nm while the thickness of magnetic films used in GMR structures is on the order of 5 nm. For such sufficiently thin films, surface scattering from the surfaces of the films plays the major role for higher resistivity. It is also important that nonmagnetic film is lattice-matched to the magnetic films so that electrons can pass from a magnetic film into the nonmagnetic film without scattering. For example, Fe and Cr have the same crystal structure (body-centered cubic) and similar lattice spacing.

When the magnetisations are antiparallel (Figure 1.4a), there is more scattering i.e. the conduction electrons are not allowed to move freely and hence, they exhibit high resistance. When an external magnetic field (leakage magnetic field for MFL testing) is applied to this multilayer structure, the direction of magnetisation of the two magnetic layers becomes parallel (Figure 1.4b) In this situation, there is less scattering resulting to less resistance to conduction electrons. Since scattering has large effect on thin film resistance, the difference in resistance for the two magnetic states can be relatively large (Figure 1.5).

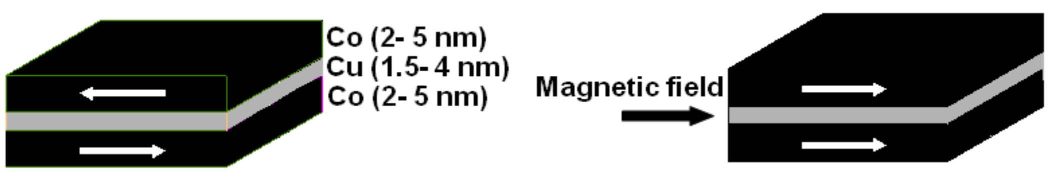

(a) (b)

Figure 1.4 GMR multilayer structures.

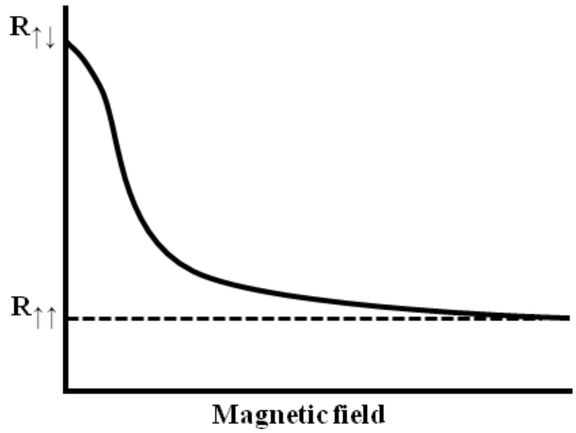

Figure 1.5 GMR effect.

GMR sensors offer high sensitivity at low magnetic fields and high spatial resolution [50-51]. Next to SQUID, GMR sensors are the most sensitive among the magnetic field sensors. They can also be integrated as arrays to facilitate rapid scanning of surfaces. But, they suffer from hysteresis effect and low saturation field. Table1.1 compares the performances of various magnetic field sensors used in MFL testing.

Table1.1 Comparison of commonly used sensors in MFL testing

Sensor	**Detectable field range (T)**	**Sensitivity (V/T)**	**Response Time**	**Sensor head size**	**Power Consumption**
Induction coil	10^{-4}- 10^{3}	0.25	0.1 MHz	2-10 mm	1 W
Hall	10^{-6}- 10^{2}	0.65	1 MHz	10 -100 µm	10 mW
SQUID	10^{-14}- 10^{-6}	10^{4}	1 MHz	10 -100 µm	10 mW
AMR	10^{-5}- 10^{0}	2.5	1 MHz	10 -100 µm	10 mW
GMR	10^{-12}- 10^{-2}	120	1 MHz	10 -100 µm	10 mW

GMR sensors are found widespread use in eddy current NDE applications in general [52-56] and for inspection of aging aerospace components, in particular [52-53]. Winchesky *et al.* [52] demonstrated the use of GMR sensors for the detection of deep fatigue cracks and Yashan *et al.* [53] use GMR sensors for the detection of hidden defects in a riveted aircraft structures. The GMR sensors can be used in eddy current testing over a wide range of frequencies from DC to MHz [54]. Chomsuwan *et al.* [55] used GMR based eddy current probe for inspection of Printed Circuit Boards (PCB). Sasi *et al.* [56] developed EC-GMR sensor that could reliably detect corrosion attack at 8 mm below surface as compared to 4 mm achieved by the conventional EC probes.

GMR sensors are also found to use in MFL NDE applications [36, 57-59]. Using the GMR sensor, Chen *et al.* [36] detected leakage magnetic fields from a 1.2 mm deep (length, 10 mm and width, 10 mm) surface notch in a 12 mm thick oil pipeline. Yashan *et al.* [57] used GMR sensors to detect small inclusions in thin steel sheets by MFL technique. Kreutzbruck *et al.* [58] used GMR sensors for detection of real fatigue cracks and artificial cracks of different depths and orientations in plates, bearings and rails. Cracks with a depth of 40 μm could be resolved with a SNR of about 20. GMR sensors are also useful for detection of stress and fatigue damage [59]. However, details on the use of GMR sensors for detection of leakage fields from deep sub-surface defects are scarce in the literature, although they find widespread use in eddy current testing.

Chapter 2: Literature Review and Motivation

2.1 Literature Review

Historically, magnetic non-destructive testing was first started in 1868 at the Institute of Naval Architects in England by Saxby [60]. He demonstrated the detection of defects and other geometry irregularities in magnetised cannon tubes by making use of a compass needle. In 1876, Hering was granted a patent for detection of discontinuities in railroad rails by using similar technique [61]. The technique of magnetic particle testing (MPT) was then developed by deForest [62] and Doane [63] around 1930. From then, MPT became an important tool for non-destructive detection of defects in steels and iron products. Later, as the subject of defect detection became more quantitative, magnetic flux leakage (MFL) technique was derived from MPT by using field sensor, instead of magnetic particles to enable the quantification of defects. The use of field sensors for detecting leakage fields was first suggested in 1933 by Zuschlag [64]. The use of sensor opened up new possibilities such as incorporation of latest advances in the field sensing devices and associated signal and image processing techniques, modeling of sensor response, etc. for enhancing the detection sensitivity of the existing MFL techniques, especially for detection of deep sub-surface defects which is not possible by MPT.

Several researchers [40, 65, 10] reported the state-of-art of NDE applications of the MFL technique. The subject of MFL technique as an NDE tool had been extensively reviewed by Beissner *et al.* [40]. They discussed the history of the development of the

MFL technique, the underlying theory for the analysis of leakage field results to characterize the defects and finally described its various applications for NDE of ferromagnetic pipes, tubes, rods and round billets. Review of the subject of magnetic leakage field calculations and interpretation of experimental measurements had been reported by Dobmann [65]. He discussed the problem of sizing of defects in MFL technique and attempted to solve it through an integral equation for field-defect interaction. Jiles [10] reviewed the theoretical calculations of leakage fields and applications of MFL technique for NDE of ferromagnetic tubes and pipes using rotomat, tubomat and discomat systems.

The detailed literature review on modeling and experimental studies reported on technique optimization, sensors and detectability for different components are given below:

2.1.1 Modeling of MFL testing

One attractive facet of MFL technique is the ability to theoretically model the physical phenomenon of leakage fields from defect region in a magnetised object. The modeling enables the calculation of field-defect interactions and thus, helps better understanding and more effective utilization of the MFL technique. The MFL modeling works reported in the literature can be broadly classified into two categories:

- Theoretical modeling
- Numerical modeling

2.1.1.1 Theoretical Modeling

Theoretical modeling of MFL technique is based on magnetic dipole method in which defects are assumed as magnetic dipoles developed on the walls of the defect. Magnetic moments of the dipoles are assumed opposite to the direction of the applied magnetic field. These magnetic dipoles generate a magnetic field outside the specimen which is equivalent to the leakage magnetic field. The theoretical modeling facilitates the understanding of several properties of MFL fields. It has the advantages over numerical modeling for offering a closed form solution, faster and convenient for simple geometries [66-67].

The theoretical basis for modeling of MFL technique is discussed below:

In the absence of free current, the magnetic field intensity $\vec{H}(\vec{x})$ at any arbitrary point $\vec{x}$ is given by [40]

$$\vec{H}\,(\vec{x}) = -\vec{\nabla}\emptyset(\vec{x}) \tag{2.1}$$

where the magnetic scalar potential $\phi(\vec{x})$ satisfies the following integral equation

$$\emptyset(\vec{x}) = \frac{1}{4\pi}\int \frac{\vec{M}.d\vec{S}}{|\vec{x}-\vec{x}'|} - \frac{1}{4\pi}\int \frac{\vec{\nabla}\cdot\vec{\mathrm{M}}}{|\vec{x}-\vec{x}'|}\,d\vec{V} \tag{2.2}$$

where $\vec{M}$ is the magnetisation (dipole moment per unit volume) of the magnetised object under test. The two terms on the right hand side of equation (2.2) correspond to two distinct sources of MFL signals associated with a defect. The first term (integral over the surface of object) is the induced surface magnetic charge density, $\sigma = \vec{M}\cdot d\vec{S}$, contributed due to the distribution of uncompensated magnetic poles on the defect surface. The second term (integral over the volume of the object) is the induced volume magnetic charge density, $\rho = -\vec{\nabla} \cdot \vec{M}$, arising due to variation in the permeability of the test object near the defect.

Zatsepin and Shcherbinin [68] pioneered the dipole modeling of the MFL technique for determination of leakage fields from two-dimensional (2D) surface-breaking defects. They proposed that MFL signal arises from induced magnetic polarization at the walls of a defect. They approximated 2D defects as line dipoles of constant magnetic charge density and derived the expressions for tangential and normal components of leakage magnetic fields due to the defect. Subsequently, Shcherbinin and Pashagin [69-70] improved this model by considering three-dimensional (3D) defects of rectangular cross-sections as surface dipoles. They also reported experimental evidence that the surface magnetic charge density on the defect walls is not uniform along the defect width. It is higher at the center of the walls than at the defect edges. Shcherbinin and Pashagin [71] also studied the effect of the proximity of sub-surface defects to the boundaries of the specimen on MFL fields.

Novikova and Miroshin [72] proposed that MFL signals are caused not only by surface magnetic charge on the defect walls, but also by volume magnetic charge close to the defect walls inside the bulk material. They approximated the volume magnetic charge for a 2D defect with rectangular cross-section by a single filament of dipoles. However, their theoretical equations are very complicated and modeling of real life defects expected in components is difficult.

Förster [73-74] analysed the same types of defects but accounted for the magnetic properties of the material and the applied magnetising field strength. The practical significance of the different sections of magnetisation curve and hysteresis loop to the magnetic flux leakage was also studied. Based on the double dipole model, Förster [74] proposed the approximate equations for tangential (H_x) and normal (H_z) components of leakage field for a surface-breaking slot of a finite depth d in a linear isotropic medium magnetised by a uniform magnetic field H_0 as

$$H_x = m\left\{\left[\frac{z}{(x^2+z^2)}\right] - \frac{(z+d)}{[x^2+(z+d)^2]}\right\} \tag{2.3}$$

$$H_z = -m\left\{\left[\frac{x}{(x^2+z^2)}\right] - \frac{x}{[x^2+(z+d)^2]}\right\} \tag{2.4}$$

The factor m is the induced dipole moment per unit length of slot given by

$$m = \frac{H_0(2d+w)}{(2\pi)} \tag{2.5}$$

where w is the width of the slot and assumption is that the permeability (μ) of the material is very much larger than that of air (μ_0). The origin of the x-z co-ordinate axes is at the centre of the top surface of the slot.

Using the idea of the Förster's dipole model and the image theory, Zhang *et al.* [75] derived expressions for the H_x and H_z components of leakage field for a rectangular defect (Figure 2.1) located at a depth h below the surface of the material magnetised by a uniform magnetic field H_0 as

$$H_x = m_1\left\{\frac{(z+h)}{[x^2+(z+h)^2]}\right\} - m_2\left\{\frac{(z+h+d)}{[x^2+(z+h+d)^2]}\right\} \tag{2.6}$$

$$H_z = -m_1\left\{\frac{x}{[x^2+(z+h)^2]}\right\} + m_2\left\{\frac{x}{[x^2+(z+h+d)^2]}\right\} \tag{2.7}$$

where

$$m_1 = \frac{H_0(2d+w)}{2\pi\left\{1-\left[\frac{(\mu-\mu_0)}{(\mu+\mu_0)}\right]^2\left(\frac{w}{4h}\right)^2\right\}^{-1}} \tag{2.8}$$

$$m_2 = \frac{H_0(2d+w)}{2\pi\left\{1-\left[\frac{(\mu-\mu_0)}{(\mu+\mu_0)}\right]^2\left[\frac{w}{2(xh+2h)}\right]^2\right\}^{-1}} \tag{2.9}$$

The typical H_x and H_z components of leakage fields computed using the above equations (2.3 to 2.9) for surface and sub-surface slots in 12 mm thick carbon steel plate are respectively shown in Figs. 2.2(a) and 2.2(b).

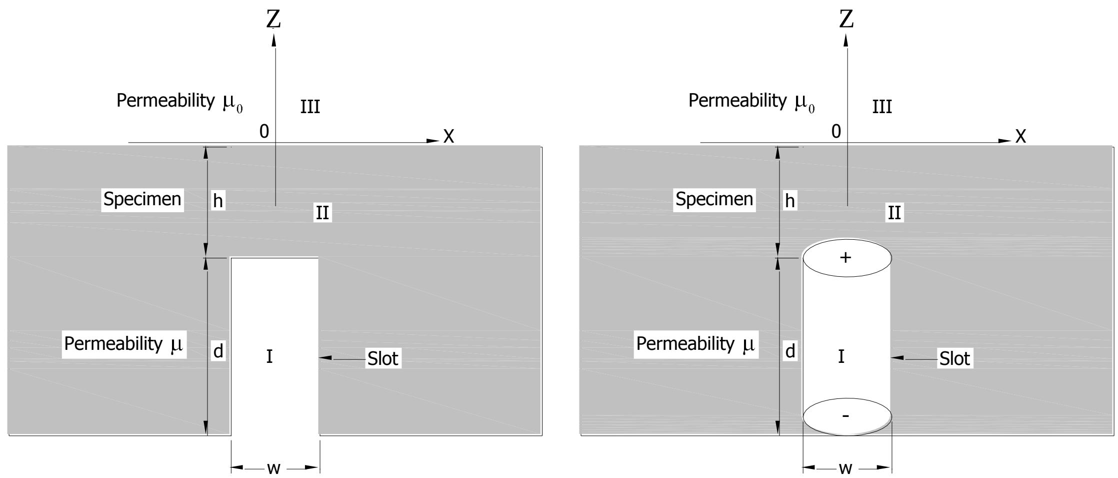

(a) (b)

Figure 2.1 (a) Two-dimensional rectangular defect below the specimen surface and (b) its modified double dipole model.

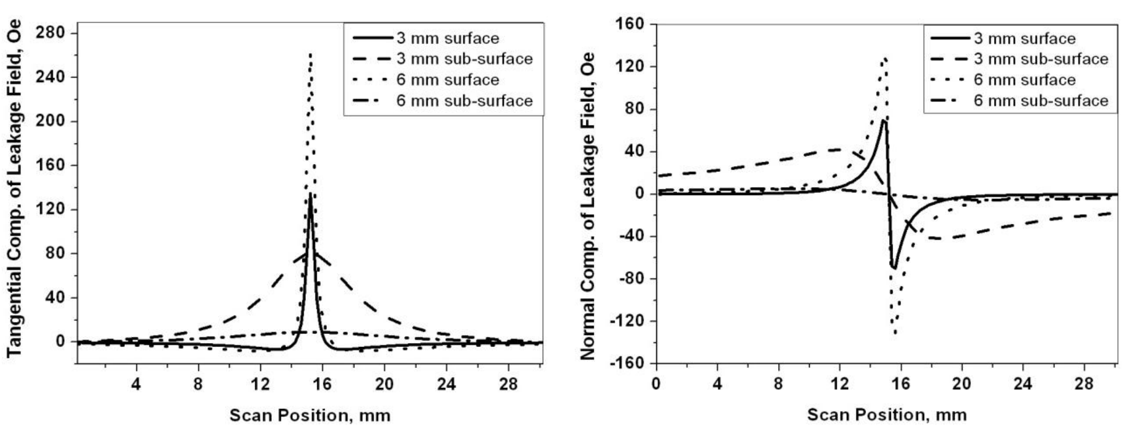

(a) (b)

Figure 2.2 Computed leakage magnetic field signals for (a) tangential and (b) normal components of surface and sub-surface slots in ferromagnetic material.

Edwards and Palmer [76] presented an analytical solution for the leakage field of surface-breaking cracks. They considered variations in the dipole strength with the magnetising conditions of the specimen. They showed that the relationships derived by Zatsepin and Shcherbinin [66] for infinitely long cracks were also valid for finite cracks, provided the magnetic leakage field was passed through the centre of the defect.

Minkov *et al.* [77-78] proposed that the surface magnetic charge density is not uniform along the defect depth - it is higher at the defect tip compared to defect mouth. They modeled this variation linearly. They also proposed a defect sizing scheme for complex surface breaking cracks, based on the minimization of the root mean square (RMS) error between the experimental Hall voltage measurement of leakage magnetic field and theoretical dipole modeling of the crack.

Lukyanets *et al.* [79] solved an integral equation to derive asymptotic solution for MFL signals from a single defect on the surface of a linear ferromagnetic half space by approximating only one saddle point of Kernel. They proposed that the density of defect-induced magnetic charges is directly related to the surface shape.

Mandache *et al.* [66] used the dipole model with constant surface magnetic charge density to analyze MFL signals due to single defect and multiple cylindrical pit defects situated close to each other. They used the locations of peaks of the normal component of MFL signals along the center of the defect to determine the length of the defect. The model result was also confirmed through comparison with experimental MFL signals from different defect geometries.

Dutta *et al.* [80-81] has recently proposed an analytical model by accounting the variation of surface magnetic charge density for defect surfaces oblique to the direction of applied field. The model was able to predict all the orthogonal components of 3D-MFL fields of a surface-breaking defect [80]. They also proposed that the use of the tangential (circumferential) component of MFL signal would be useful for determination of location of defects with respect to the sensor [81].

The above literature review indicates that almost all the theoretical modeling studies have been concentrated to the prediction of MFL signals from simple defect geometries located at the object surface. They pose difficulties for realistic defect shapes for most real life NDT problems and also lack generalization while making the necessary assumptions to obtain tractable analytical solutions. Therefore, use of theoretical modeling is limited for design of magnetisation systems and hence, optimization of the MFL techniques for diverse applications including complex geometries and defect shapes.

2.1.1.2 Numerical Modeling

Various numerical modeling methods have been reported for MFL NDE. They include finite difference method (FDM) [82], finite element method (FEM) [83-84], boundary element method (BEM) [85], hybrid method with FEM-BEM [86-87], meshless method [88], etc. for analyzing MFL signals from defects in ferromagnetic components. Among these, finite element (FE) method has been extensively used for study of leakage magnetic fields in MFL testing as it can handle nonlinear [89], time-dependent and circular geometry problems [90]. FE modeling has the advantages over theoretical modeling for enabling to model the complex boundary geometries and nonlinear material characteristics found in actual defects and ferromagnetic materials. In general, it requires intensive computer resources [91-92].

FE modeling of MFL technique was first carried out by Huang and Lord [93]. They could predict the field-defect interaction and this was a real breakthrough in the area of MFL science and technology. This was followed by a series of significant works by Lord *et al.* [94-95] and Atherton *et al.* [96-97]. The study showed that the FE modeling has a potential tool for the design and optimization of MFL techniques through analyzing MFL signals from defects [94-95]. In addition, it provides the possibility of sizing of defects from the leakage field profile. Atherton *et al.* [97] predicted the MFL signals from rectangular grooves of different depths in a pipe using Infolytica MagNet software. In these early works, only 2D-FE modeling with comparatively coarse mesh elements was employed and defects were treated as 2D profile instead of the actual 3D geometry. However, since the MFL signals are essentially three dimensional perturbations, 2D FE modeling of MFL technique appears less satisfactory for signal calculations from real defects.

Ida *et al.* [98] realized a 3D-FE modeling to predict the leakage field around a rectangular slot in a ferromagnetic bar. It could predict leakage fields of defects regardless of their shape or location. Various groups [17, 34, 99-104] extended 3D-FE modeling to study leakage fields for various test conditions. Naemi *et al.* [17] used Infolytica MagNet software for modeling of MFL technique for inspection of ferromagnetic plates and demonstrated that when modeling was extended to 3D, the magnitude of the saturation magnetisation within the test plate was reduced. They compared the predicted MFL signals from 2D and 3D models and showed that a signal obtained from 2D models is much larger than 3D models due to higher saturation level in the area of the defect in 2D models. Zuoying *et al.* [99] and Ji *et al.* [100] used ANSYS finite element software for 3D-FE modeling of pipeline MFL NDE to analyze the influence of dimensions (length, width and depth) of surface defects and lift-off of the sensor to the MFL signals. It was shown that the MFL signal amplitude increases with the increase in width (Figure 2.3a) and depth of defects (Figure 2.3b) while the MFL signal amplitude decreases with the increase in length of defects and lift-off of the sensor. Ji *et al.* [100] also studied the influence of intensity of applied magnetic field on MFL signals and observed that MFL signal amplitude increases initially with the intensity of magnetisation and then tends to stable when the intensity reaches the magnetic saturated condition. Chen *et al.* [101] performed 3D-FE modeling to investigate the effect of complex corrosion on MFL signals from a 12 mm thick steel plate and found that the relative positions of the complex corrosion pits affects the magnitude of MFL signals. The effects of different pit corner geometries on MFL signals were studied by Babbar *et al.* [102] and they reported that MFL signals are influenced by the sharpness of the pit corner. The interaction between nearby corrosion pits was studied by Mao *et al.* [103] using Infolytica MagNet 6 software and it was found that the alignment of the pits had significant effects on the absolute values of MFL signals. Li *et al.* [34] simulated 3D MFL signals from irregular shaped surface defects in magnetic specimens using FEMLAB software and showed the potential for improvement of defect characterization capabilities of existing MFL systems by sensing all the 3D magnetic fields, especially for defects having irregular geometries. Ireland *et* *al.* [104] simulated a circumferential magnetizer for in-line inspection (ILI) of pipelines under both static and moving tool conditions and highlighted the difficulties associated with maintaining a stable magnetic circuit for a moving ILI tool.

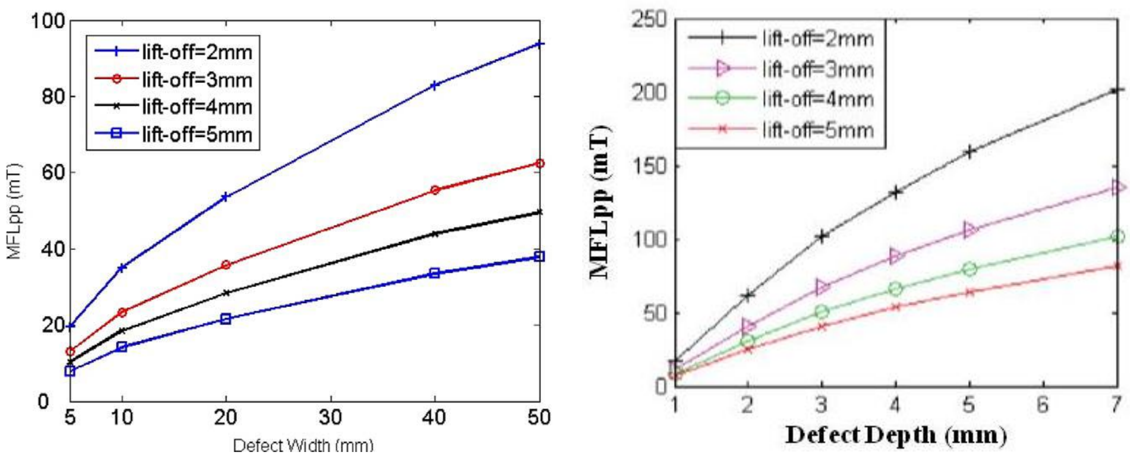

(a) (b)

Figure 2.3 MFL signal peak-to-peak amplitudes (MFL_{pp}) as functions of (a) defect width (length 10 mm, depth 10 mm) in a 14 mm thick plate [99] and (b) defect depth (length 10 mm, width 10 mm) in a 10 mm thick plate at various lift-offs [100].

Effect of velocity of MFL inspection tools (generally PIG) on MFL signals for testing of pipelines was extensively studied using FE modeling by various groups [89, 91, 105-106]. Li *et al.* [89] used ANSOFT Maxwell EM V10 software and showed that the shape and magnitude of the MFL signal changes with circumferential and axial MFL and the velocity at which it influences the MFL signal is much lower in the circumferential MFL than the axial MFL. Yang *et al.* [105] showed that the velocity-induced circumferential fields of PIGs could be used for detecting axial stress corrosion cracks in pipelines. Cui *et al.* [91] proposed a simplified FE modeling method to simulate the movement of MFL inspection tool inside the pipe in which the defect is fixed and the magnetic fields along the axial direction are considered as representative of the sensor signals from the MFL inspection tool.

Various group of researchers [107-110] paid significant scientific attention to the effect of operating line pressure induced stress of the steel pipelines on MFL signals. Leonard *et al.* [107] observed anisotropy on MFL signals, i.e., increase in MFL signal amplitude along axial direction and decrease along circumferential direction of pipes. Later, Ryu *et al.* [108] used Infolytica MagNet 6 software to investigate the effects of local anisotropies simulating the stress concentrations induced by tensile circumferential stress on MFL signals for various far- and near-side pit depths and they observed that bulk stress and corrosion pit depth have a significant effect on MFL signals. Babbar *et al.* [109-110] used Infolytica MagNet 6 software to analyze the effects of dent-induced localized residual stresses [109] and dent geometry [110] on MFL signals from a steel plate and found that the geometry effect signal is larger than the stress effect signal. Further, they reported that the MFL signal has greater sensitivity for compressive stresses than for tensile stresses.

Katoh *et al.* [28, 111] modeled the yoke magnetisation in MFL testing using 2D-FEM and analyzed the influence of air gap between the magnetising yoke and specimen and also specimen thickness on the detectability of flaw. They showed that MFL signal decreases with the increase in air gap as well as specimen thickness [127]. They also proposed an approach for estimation of intensity of magnetisation of the specimen by extrapolating the intensity of magnetic field measured near the specimen surface to that at lift-off being zero [28].

In the last decade, researchers [26, 112-115] pursued FE modeling to optimize the MFL techniques of tank floors [26] and pipelines [112-115]. Xiao-chun et al. [26] used OPERA-3D finite element analysis software to research the influence of magnet size (width, height, pole spacing), the air gap between the magnetic pole and specimen surface and the magnetic force in the MFL testing of tank floors. The modeling results indicated that variation of the magnet width affects the magnetisation much more than variation of the magnet thickness and when the floor has reached its magnetising saturation, the testing sensitivity and the SNR can improve with the increase in the magnet-pole spacing and the pole-piece thickness. Park *et al.* [112-113] optimized the magnetisation level of ferromagnetic pipes to obtain maximum change in leakage magnetic flux from the region of defects. Their research found that the MFL signal would be maximum if the magnetisation level is operated near to the saturation of B-H curve [112] and the sensitivity of the optimized MFL system could also be increased to 200% by placing a high permeable back yoke system close to the sensor [113]. Mackintosh *et al.* [114] studied the various MFL assemblies for improving the detection sensitivity in MFL testing of pipelines and obtained the highest improvement in the MFL assembly when opposing magnetising assemblies were added to each end of the primary magnetising assembly. Their result also indicated no improvement in the sensitivity with the increase in magnet size and addition of brushes to the pole-pieces in the traditional magnetising systems used in the pipeline testing. The research of Norouzi *et al*. [115] for optimization of length of magnetising yoke used in MFL testing of pipelines showed that longer yoke does not necessarily result uniform magnetic flux density in the sample under test. The optimum length of the yoke was found to be between 300 mm to 400 mm for achieving higher sensitivity of defects in pipelines (outer diameter 300 mm, wall thickness 10 mm).

In the above mentioned literature review, it is found that the majority of the studies are focused on MFL signals under different defects shapes, dimensions and locations. Effects of velocity of inspection tool and line pressure induced stress on MFL signals for ILI of pipelines have also been thoroughly investigated. However, only few studies have been carried out for the optimization of MFL techniques employed in pipes and tank bottom floors. Therefore, a systematic numerical model based study is needed to optimize the MFL techniques for various geometries used in different field applications.

2.2 Motivation

Although few modeling studies were reported for optimization of MFL techniques in pipes and tank bottom floors, there is no systematic study to generalize the model based optimization of the MFL techniques for different geometries. Apart from the pipelines and tank bottom floors, ferromagnetic components such as carbon steel plates, stranded track ropes, small diameter steam generator tubes, etc. are abundant in critical applications. Corrosion induced defects are the major concerns in steel plates and tank floors. Prolonged use of the ropes or wires is expected to cause abrasion and wear, resulting in loss of metallic cross-sectional area (LMA) or localized flaw (LF) type defects [21]. Detection of damage in the ropes or wires is essential as part of the condition monitoring and life management programs. Periodic in-service inspection (ISI) of steam generator tubes is essential to detect defects and size them [116]. NDE of thick walled ferromagnetic tubes is challenging as the leakage magnetic field from outer surface defect is very feeble. There is a need to develop high sensitive, fast and reliable NDE techniques for ISI of these critical components. As these components are made up of ferromagnetic materials, MFL technique is well suited and the use of GMR sensors is very attractive as they offer high sensitivity for low magnetic fields, good SNR and high spatial resolution [36, 50].

For fast inspection of the components, array sensors are essential to facilitate rapid scanning of the surfaces with large coverage. Further, optimization of MFL techniques for these ferromagnetic components is inevitable for enhanced and reliable detection of defects by increasing the MFL signal and at the same time, decreasing the background noise. However, the detailed optimizations of magnetisation units for various geometries, identification of number of sensors in an array and their optimal locations are essential and general guidelines do not exist for various geometries. Experimental based optimization is time consuming, cumbersome and sometimes, impractical. In this context, the use of finite element numerical modeling is very attractive.

2.3 Objective of the Thesis

The primary objective of the research work in the thesis is model based optimization of MFL techniques for high sensitive, fast and reliable detection of defects in ferromagnetic components in i) cuboid geometry, ii) solid cylindrical geometry and iii) hollow cylindrical geometry. The scope involves optimization of the magnetisation unit, number of GMR sensors and sensor locations for enhanced detection and fast imaging of defects as detailed below:

i) Optimization of GMR sensor based MFL technique for detection of shallow surface defects and deep sub-surface defects in 12 mm thick carbon steel plates (cuboid geometry)

ii) Optimization of GMR sensor based MFL technique for detection of localized flaws and loss of metallic cross-sectional area type of defects in 64 mm outer diameter steel ropes (solid cylindrical geometry)

iii) Optimization of GMR sensor based MFL technique for detection of localized defects in 17.2 mm outer diameter (wall thickness, 2.3 mm) SG tubes of PFBR (hollow cylindrical geometry).

The objective also includes proposing a generalized approach for model based optimization of MFL technique for different geometries, based on the experience gained from the studies on these three geometries.

2.4 Organization of the Thesis

The thesis consists of 9 chapters. The details of each chapter are summarized below:

Chapter 1 gives a brief introduction to MFL NDE and Chapter 2 provides a comprehensive literature survey as well as objectives of the present work.

Chapter 3 deals with the details of 3D-FE modeling of the MFL technique. It discusses the governing equations, boundary conditions applied, meshing and solver used in the model. It explains the post processing of the FE solution for prediction of MFL signal of a defect along the scan-line of the sensor at a definite lift-off.

Chapter 4 describes the optimization of GMR sensor based MFL technique for detection of leakage magnetic fields from surface and sub-surface defects in cuboid geometry i.e. a ferromagnetic steel plate. It explains how the FE modeling has been carried out to optimize the magnetising unit comprising of electromagnetic yoke for achieving its optimum leg spacing, height and magnetising current used in the MFL technique. Chapter 4 also discusses the influence of inclined and interacting defects on MFL signals as well as the optimization of locations of 2D arrays of 16 GMR sensors.

Chapter 5 describes the optimization of MFL technique for solid cylindrical geometry i.e. steel track ropes, essentially optimization of two saddle coils based magnetising unit and the development of a flexible GMR sensor array system.

Chapter 6 deals with the optimization of MFL technique for hollow cylindrical geometry i.e. ferromagnetic SG tubes of PFBR. It explains the development of bobbin coils and GMR tandem array sensors for imaging of localized defects in the tube.

Chapter 7 presents a generalized approach for model based optimization of MFL technique for three different geometries. Application of this approach for various geometries is discussed for fast and high sensitive detection of surface and sub-surface defects in ferromagnetic materials.

The chapter 8 summarizes the major conclusions drawn from the model based optimization studies as well as the experimental measurements. The chapter 9 gives the scope for further studies.

Chapter 3: Finite Element Modeling of MFL Technique

3.1 Introduction to Finite Element Modeling

The finite element modeling (FEM) is a numerical technique for finding approximate solutions to boundary value problems. It was first proposed in the 1940s [117] and its use began in the 1960s for structural and continuum mechanics and later found a wide variety of applications in electromagnetic field problems [118]. Subsequently, FEM has also been started using in NDE research community [119-120]. Today, the FEM has become a general tool for designing many engineering devices to improve their performances and efficiencies.

In FEM, the domain of interest is discretized into a finite number of sub-domains, usually referred as elements. The interconnecting points are called nodes. The exact variation of the unknown function (e.g. potential) is approximated by a simple interpolation functions with unknown coefficients at each nodes associated with the elements. In other words, the original boundary value problem with infinite degrees of freedom is transformed into a problem with finite degrees of freedom. Then, a system of algebraic equations is obtained by applying the Ritz variational or Galerkin procedure and solution of the boundary value problem is obtained by solving the system of equations. Finally, the desired parameters such as potential, field, etc. can be computed at the nodes situated within the region of interest. The steps involved in the FEM of a boundary value problem are as follows [117, 121]:

1) Discretization of the domain
2) Selection of the interpolation functions
3) Formulation of the system of equations
4) Solution of the system of equations
5) Post-processing of the data

3.1.1 Discretization of Domain

Domain discretization is the most important step in any FEM as it affects the computer storage requirements, the computation time and the accuracy of the modeling results. In this step, the entire domain is divided into a finite number of sub-domains, usually referred as elements. For one-dimensional (1D) modeling, the elements are often short line segments interconnected to approximate the original line (Fig. 3.1a). For two-dimensional (2D) modeling, the elements are usually small triangles and rectangles (Fig. 3.1b). The rectangular elements are well suited for discretization of rectangular geometry while, the triangular elements can be used for any geometries including the irregular geometries. For three-dimensional (3D) modeling, the possible elements are tetrahedral, triangular prisms and rectangular bricks (Fig. 3.1c). Among these, tetrahedral are the simplest and best suited for arbitrary geometries [117].

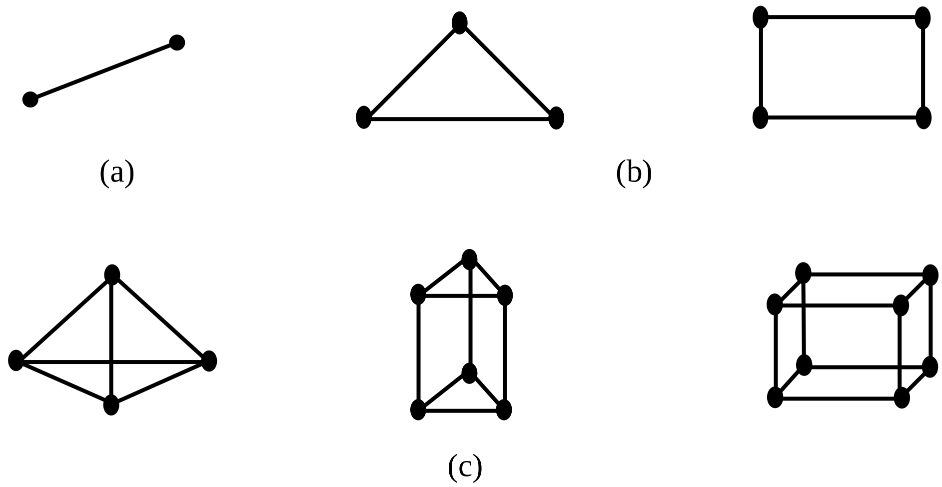

Figure 3.1 (a) One-dimensional, (b) two-dimensional and (c) three-dimensional basic finite elements.

3.1.2 Selection of Interpolation Functions

The second step of FEM is the selection of an interpolation function that approximates the unknown function within an element. The interpolation is generally selected to be a polynomial of first (linear), second (quadratic), or higher order. Higher order polynomials are usually more accurate compared to lower order polynomials. However, higher order polynomials result in a more complicated formulation than that of lower order polynomials. Therefore, the simple linear interpolation is still widely used in the FEM. The typical interpolation function of an element e at the node j in one dimension is given by,

$$N_j^e(x) = a_0^e + a_1^e x$$

where a_0 and a_1 are unknown coefficients or parameters of the expansion and x is the independent variable.

3.1.3 Formulation of System of Equations

In this step, the elemental equation is first formulated using either the Ritz variational method or Galerkin method. Then, all the elemental equations are assembled over all elements to form the system of equations. Finally, the boundary conditions are imposed to obtain the final form of the system of equations. There are two types of boundary conditions viz. Dirichlet boundary condition and Neumann boundary condition. Dirichlet boundary condition prescribes the unknown function at the boundary while the Neumann boundary condition sets the normal derivative of the function to vanish at the boundary.

3.1.4 Solution of System of Equations

In FEM, the system of equations is generally large set of algebraic equations. This set of equations is then solved for getting the field or potential at the nodes. The different formulations result in different matrices. These may be linear or nonlinear, sparse or dense, symmetric or non-symmetric. If the system of equation is linear, it has been solved using numerical linear algebra methods such as Gaussian elimination, LU decomposition, QR decomposition, single value decomposition, Eigen value, etc. Among these, Gauss elimination method is the most efficient method for solving a linear system of equations, particularly if there is no special property of the matrix to exploit (sparsity, symmetry, etc.). On the other hand, if the equation is nonlinear, it has been solved using the Newton-Raphson method, Bailey’s method, Chord method, etc. [118, 122]. Depending upon the size of the system of equations, two types of solvers viz. direct solver [123] and iterative solver [124] are available for solving the equations.

Direct solvers are mostly used for solving relatively small size systems. It provides the solution faster compared to iterative solver. However, for very large systems of equations, the memory requirements of direct solvers are too large. Therefore, iterative solvers are generally used in FEM. Iterative methods begin with an initial estimate for the solution and successively improve it until it converges to the solution as accurate as desired. In practice, the iteration terminates when some norm of the residual, or some other measure of error, is as small as desired. Commonly used iterative methods for solving systems of equations are conjugate gradient (CG), generalized minimum residual (GMRES) and flexible generalized minimum residual (FGMRES) [118, 125]. The CG method is used only for symmetric positive definite matrices while GMRES and FGMRES are used for general nonsymmetric problems. The GMRES method computes a sequence of orthogonal vectors that minimizes the residual norm in a least squares norm. Hence, the method leads to the smallest residual for a fixed number of iterations. However, it requires preconditioners to improve the convergence. FGMRES method can handle more general preconditioners which makes FGMRES method as the more effective iterative solver in several FE modeling [125].

3.1.5 Post-processing of Data

Once the system of equations has been solved, we can compute the desired parameters such as field or potential and display the results in the form of graphs or images which are more meaningful and interpretable.

3.2 Finite Element Modeling of MFL Technique

Finite element modeling has been extensively used for study of leakage magnetic fields in MFL testing. It enables study of field-defect interactions and thus, helps in better understanding of the MFL technique and enhances its applicability. FEM has the advantages of flexibility for modeling of irregular material geometry and boundaries. It yields a stable solution of required accuracy. It can also handle material nonlinearity and eddy currents well. However, the representation of open boundaries is difficult. The unknowns must be solved for throughout the whole domain even if the solution is required only at a few points. It also requires intense computational time and resources [118, 120]. Detailed literature review on FE modeling of MFL techniques for various test conditions were discussed in Chapter 2. Here, the important steps needed for FE modeling of MFL technique for various geometries are discussed.

3.2.1 Construction of Model Geometry

The first step in the FE modeling of MFL technique is to construct the model geometry. The FE model geometry consists of the test specimen with defect, magnetisation unit and a boundary black box. The typical geometry of 3D-FE model for MFL NDE of carbon steel plate constructed using COMSOL Multiphysics package [125] is shown in Figure 3.2. It consists of the steel plate with defect, electromagnetic yoke wounded with copper coils and a boundary box.

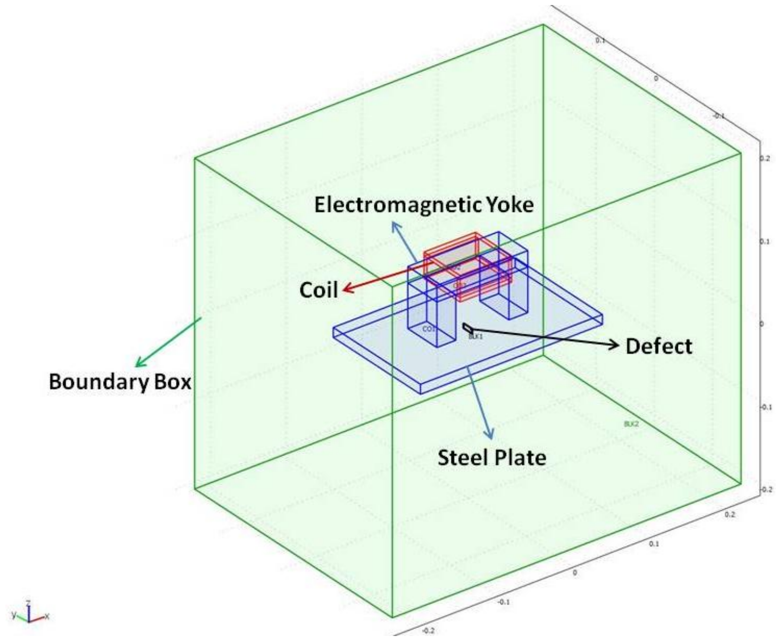

Figure 3.2. 3D-FE model geometry for MFL NDE of steel plate.

3.2.2 Mathematical Formulation

A complete description of the MFL phenomenon requires formulating both the governing differential equation and boundary conditions. The governing equations along with the boundary conditions imposed for FE modeling of MFL technique are discussed in the following sub-sections:

3.2.2.1 Governing Equation

Maxwell's magneto-static equations given below are used for FE modeling of MFL technique

$$\nabla \cdot B = 0 \tag{3.1}$$

$$\nabla \times H = J \tag{3.2}$$

along with the constitutive relation

$$B = \mu_0 \mu_r H = \mu_0 (H + M) \tag{3.3}$$

where B is the magnetic flux density,

H is the magnetic field intensity,

J is the current density,

μ_0 is the magnetic permeability of free space,

μ_r is the relative permeability of the ferromagnetic material under test,

M is the magnetisation level of the material

The flux density B is related to the magnetic potential A as

$$B = \nabla \times A \tag{3.4}$$

Assuming the magnetic permeability of test material is isotropic, equation (3.2) can be written as,

$$\nabla \times \left(\frac{1}{\mu_0 \mu_r} \nabla \times A\right) = J$$

or,

$$\nabla \times \left(\frac{1}{\mu_0 \mu_r} \nabla \times A\right) = \mathrm{J_s} - \sigma \frac{\partial \mathrm{A}}{\partial \mathrm{t}} + \sigma \vartheta \times (\nabla \times \mathrm{A}) \tag{3.5}$$

Here, $\mathrm{J_s}$ is the source current density; $\sigma \frac{\partial \mathrm{A}}{\partial \mathrm{t}}$, the eddy current generated by the applied magnetic field and $\sigma\vartheta\times(\nabla\times\mathrm{A})$, the current density resulting from the relative motion between the magnetizing unit (magnetic field) and the test specimen.

Equation (3.5) is the governing differential equation used in the FE modeling of MFL technique. In this study, the effects of the eddy current and the motion of the magnetizing unit are not considered.

In order to determine A uniquely in equation (3.5), Coulomb gauge condition as given by [126] is imposed

$$\nabla \cdot A = 0 \tag{3.6}$$

The solution to equation (3.5) can be obtained by minimizing the field energy related expression called functional (Ritz variational formulation) given as

$$F(A) = \frac{1}{2}\iiint_V \frac{1}{\mu_r}(\nabla \times A)\cdot(\nabla \times A)dV - \mu_0 \iiint_V J \cdot A\, dV \tag{3.7}$$

This can be written in terms of components of vector potential A_x, A_y and A_z as,

$$F = \frac{1}{2}\iiint_V \frac{1}{\mu_r}\left[\left(\frac{\partial A_z}{\partial y} - \frac{\partial A_y}{\partial z}\right)^2 + \left(\frac{\partial A_x}{\partial z} - \frac{\partial A_z}{\partial x}\right)^2 + \left(\frac{\partial A_y}{\partial x} - \frac{\partial A_x}{\partial y}\right)^2 - \mu_0\big(A_x J_x + A_y J_y + A_z J_z\big)\right] dV \tag{3.8}$$

The volume of the domain (boundary box) *V* is discretized into *M* small tetrahedral volume elements. For an e^{th} element of *n* nodes, the components of vector potential are given by,

$$A_x^e = \sum_{j=1}^{n} N_j^e A_{xj}^e = \{N^e\}^T\{A_x^e\} = \{A_x^e\}^T\{N^e\}$$

$$A_y^e = \sum_{j=1}^{n} N_j^e A_{yj}^e = \{N^e\}^T\{A_y^e\} = \{A_y^e\}^T\{N^e\} \tag{3.9}$$

$$A_z^e = \sum_{j=1}^{n} N_j^e A_{zj}^e = \{N^e\}^T\{A_z^e\} = \{A_z^e\}^T\{N^e\}$$

where N_j^e is the shape function of the e^{th} element. Substituting (3.9) into (3.8) gives the value of *F* associated with the e^{th} element and by taking its partial derivatives, we get

$$\left\{\frac{\partial F^e}{\partial A_x^e}\right\} = [K_{xx}^e]\{A_x^e\} + [K_{xy}^e]\{A_y^e\} + [K_{xz}^e]\{A_z^e\} - \{b_x^e\}$$

$$\left\{\frac{\partial F^e}{\partial A_y^e}\right\} = [K_{yx}^e]\{A_x^e\} + [K_{yy}^e]\{A_y^e\} + [K_{yz}^e]\{A_z^e\} - \{b_y^e\}$$

$$\left\{\frac{\partial F^e}{\partial A_z^e}\right\} = [K_{zx}^e]\{A_x^e\} + [K_{zy}^e]\{A_y^e\} + [K_{zz}^e]\{A_z^e\} - \{b_z^e\}$$

where the matrices and vectors are respectively given by,

$$[K_{xx}^e] = \iiint_{V^e} \frac{1}{\mu_r}\left(\frac{\partial\{N^e\}}{\partial y}\frac{\partial\{N^e\}^T}{\partial y} + \frac{\partial\{N^e\}}{\partial z}\frac{\partial\{N^e\}^T}{\partial z}\right) dV$$

$$\left[K_{yy}^e\right] = \iiint_{V^e} \frac{1}{\mu_r}\left(\frac{\partial\{N^e\}}{\partial z}\frac{\partial\{N^e\}^T}{\partial z} + \frac{\partial\{N^e\}}{\partial x}\frac{\partial\{N^e\}^T}{\partial x}\right) dV$$

$$[K_{zz}^e] = \iiint_{V^e} \frac{1}{\mu_r}\left(\frac{\partial\{N^e\}}{\partial x}\frac{\partial\{N^e\}^T}{\partial x} + \frac{\partial\{N^e\}}{\partial y}\frac{\partial\{N^e\}^T}{\partial y}\right) dV$$

$$\left[K_{pq}^e\right] = -\iiint_{V^e} \frac{1}{\mu_r}\left(\frac{\partial\{N^e\}}{\partial q}\frac{\partial\{N^e\}^T}{\partial p}\right) dV \qquad p, q = x, y, z; p \neq q$$

and

$$\{b_x^e\} = \iiint_{V^e} \{N^e\} J_x \, dV$$

$$\left\{b_y^e\right\} = \iiint_{V^e} \{N^e\} J_y \, dV$$

$$\{b_z^e\} = \iiint_{V^e} \{N^e\} J_z \, dV$$

Assembling of all the elements, the system of equations becomes

$$\left\{\frac{\partial F}{\partial A_x}\right\} = \sum_{e=1}^{M} [K_{xx}^e]\{A_x^e\} + \left[K_{xy}^e\right]\left\{A_y^e\right\} + [K_{xz}^e]\{A_z^e\} - \{b_x^e\}$$

$$\left\{\frac{\partial F}{\partial A_y}\right\} = \sum_{e=1}^{M} \left[K_{yx}^e\right]\{A_x^e\} + \left[K_{yy}^e\right]\left\{A_y^e\right\} + \left[K_{yz}^e\right]\{A_z^e\} - \left\{b_y^e\right\}$$

$$\left\{\frac{\partial F}{\partial A_z}\right\} = \sum_{e=1}^{M} [K_{zx}^e]\{A_x^e\} + \left[K_{zy}^e\right]\left\{A_y^e\right\} + [K_{zz}^e]\{A_z^e\} - \{b_z^e\}$$

Minimizing the functional with respect to the components of vector potential, we obtain

$$[K_{xx}]\{A_x\} + \left[K_{xy}\right]\left\{A_y\right\} + [K_{xz}]\{A_z\} = \{b_x\}$$

$$\left[K_{yx}\right]\{A_x\} + \left[K_{yy}\right]\left\{A_y\right\} + \left[K_{yz}\right]\{A_z\} = \left\{b_y\right\}$$

$$[K_{zx}]\{A_x\} + \left[K_{zy}\right]\left\{A_y\right\} + [K_{zz}]\{A_z\} = \{b_z\}$$

The system of equations can be written in the form of global matrix as,

$$\begin{bmatrix} K_{xx} & K_{xy} & K_{xz} \\ K_{yx} & K_{yy} & K_{yz} \\ K_{zx} & K_{zy} & K_{zz} \end{bmatrix} \begin{Bmatrix} A_x \\ A_y \\ A_z \end{Bmatrix} = \begin{Bmatrix} b_x \\ b_y \\ b_z \end{Bmatrix} \tag{3.10}$$

or,
$$[K]\{A\} = \{b\}$$

where $[K]$ is the [*3N X 3N*] global matrix (or stiffness matrix), $\{A\}$ is the (*3N X 1*) unknown vector, $\{b\}$ is the (*3N X 1*) global source vector, and *N* is the number of nodal points in the solution region [98].

At this stage, material properties such as magnetic permeability of the test specimen, number of turns of copper winding, magnetisation current of the coil, etc. are set for all the sub-domains used in the model. The next step is the application of boundary conditions to the global system of equations.

3.2.2.2 Boundary Conditions

The magnetic insulation ($n \times A = 0$) of Neumann boundary condition is applied to boundaries (black box) confining a surrounding region of air. This sets the tangential component of the magnetic potential or the normal component of the magnetic field to zero [125]. Ideally, this condition is valid at infinitely large distances from the specimen. However, in the interest of simplicity and computation time, the region of interest is shrunk to a minimum subject to the condition that a significant increase in the region of interest does not lead to any appreciable change in the spatial solution data.

3.2.3 Meshing

Meshing is the discretization of the model geometry into small elements. For 3D-FE modeling, the model geometry is discretized into tetrahedral mesh elements. The number of mesh elements is determined from the shape of the geometry and element order (linear, or of higher order) in the model. When the size of the elements is small, a more accurate solution can be expected. On the other hand, it increases the number of elements which leads to increase of the number of nodes and needs more computational time to solve the resulting bigger global matrix. Hence, proper meshing should been done wisely. One advantage of FEM is that meshing of various sizes can be done in different sub-domains. A finer mesh must be used in the sub-domain where high potential gradients (e.g. defect region) are expected. A courser meshing should be done in the sub-domain of uniform potential. This will provide a more reliable and accurate result in the reasonable computational time. If the meshing is refined further beyond a certain limit, the accuracy of the solution will not improve further, due to round-off errors associated with more number of computational operations for more number of elements. One typical example of mesh that consists of 214584 tetrahedral elements with corresponding 1380774 degrees of freedom is shown in Figure 3.3. The mesh element size near the defect is chosen to be small (0.00002 m) to obtain an accurate result in a reasonable computation time.

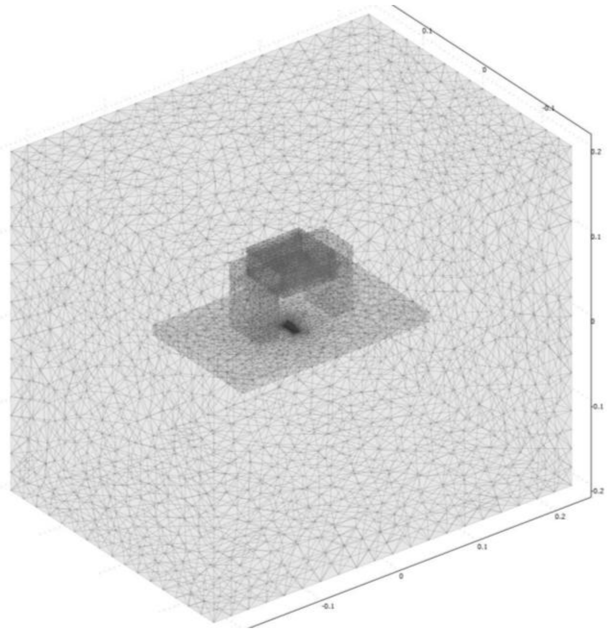

Figure 3.3 Typical meshing for 3D-FE modeling of MFL technique of steel plate.

3.2.4 Solver

Equation (3.9) is solved in three dimensions using either direct or iterative methods. For models with large degrees of freedom (more than 100,000), the direct solvers need too much memory [125]. In such cases, the more memory-efficient iterative solvers such as GMRES, FGMRES and CG perform better. However, iterative solvers are less stable than direct solvers in that they do not always converge at a solution. For 3D-FE modeling, the number of meshes and hence, the corresponding size of the system of equations is reasonably large. Therefore, iterative method is generally employed for solving the system of equations. Among the iterative solvers, FGMRES is more effective with fast convergence. The computation time for solving equation (3.10) using FGMRES solver is approximately 90 minutes in a dual core 64 bit processor with 8 GB RAM workstation.

3.2.5 Post-processing and Prediction of GMR Signal

Post-processing is performed to predict the desired parameters viz. magnetic flux density *B* and field *H* from the magnetic vector potential *A* using the equations (3.4) and (3.3) respectively. The flux density *B* is again post-processed to predict the B_x and B_z components of the leakage flux from a defect along scan line of the sensor at a definite lift-off. Various plotting methods such as surface, contour, streamline, etc. can be performed for visualization of MFL profiles from the defects. The model predicted MFL signals are further analyzed for design and optimization of the MFL techniques.

Typical magnetic flux density profiles of surface slot of 3.32 mm depth and sub-surface slot located at 6.24 mm below the surface in a 12 mm thick carbon steel plate are shown in Figure 3.4. One can easily visualize the leakage MFL profiles of the slots from the arrow contour plots. As expected, the leakage magnetic field at the surface for sub-surface slot is weaker than that of the surface slot.

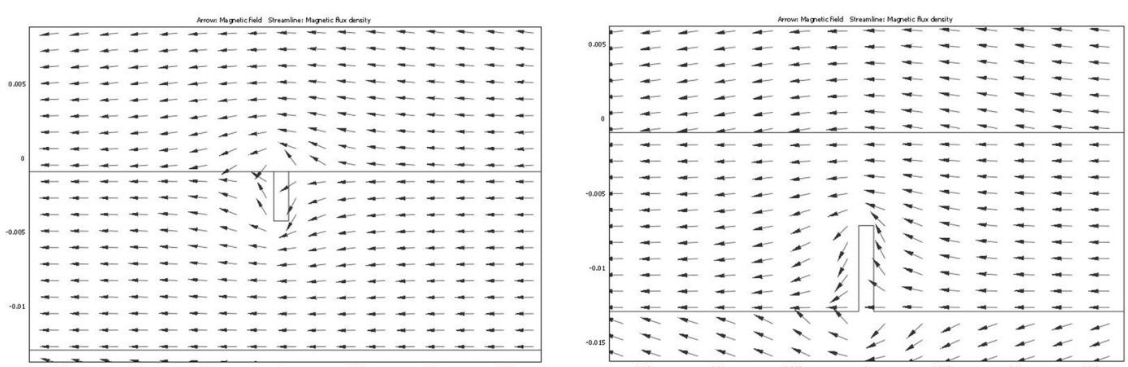

(a) (b)

Figure 3.4 FE model predicted arrow contour plots for (a) surface slot of 3.32 mm depth and (b) sub-surface slot located at 6.24 mm below the measurement surface.

3.3 Validation of Model

COMSOL 4.3 Multiphysics software package has been used for optimization of MFL techniques in the present thesis. Firstly, the model has been validated with the experimental MFL signals. For this purpose, a hollow cylindrical geometry steam generator tube (length 100 mm, outer diameter 17.2 mm and wall thickness 2.3 mm) with circumferential notches (length 5 mm, width 1 mm) of depths 0.50 mm to 1.25 mm in steps of 0.25 mm has been modeled. The tube has been magnetized with two bobbin coils (cross-sectional area 10 x 3 mm^2) wound on a ferrite core. Table 3.1 gives the parameters used in the 3D-nonlinear FE modeling. The μ_r value of the tube is taken from its magnetization curve as shown in Figure 3.5. Single GMR sensor positioned centrally over the defects has been considered for modeling. Figure 3.6(a) shows the comparison of model predicted and experimentally obtained (measured using a GMR sensor) axial component of MFL signals (B_a) from the notches. A good agreement is seen between the trends of model predicted and experimental MFL signal amplitudes. Further, MFL signal peak amplitudes (B_a^{peak}) of notches have been calculated by subtracting the background value (away from the notch) from the signal peak. In both the cases, the B_a^{peak} amplitude increases with the increase in notch depth due to increase in reluctance. The model predicted B_a^{peak} amplitude values are within 10% of the experimental values. The deviation between the model and experimental values can be attributed to the flux concentration intrinsically present in the GMR sensor.

Table 3.1 Parameters used in the FE model

Bobbin coils	No. of coils: 2 No. of turns of each coils: 70 Cross-sectional area: 10x3.4 mm ^{2} Current: 1.25 A Conductivity: 5.98x10^7 S/m
Ferrite core	Length: 40.2 mm, Diameter: 4.8 mm Relative permeability: 1000 Conductivity: 1.0x10^{-5} S/m
SG tube	Length: 100 mm, Outer diameter: 17.2 mm Wall thickness: 2.3 mm Relative permeability: Magnetization curve Conductivity: 4.03x10^6 S/m
Defect (notch) modeled	Length: 5 mm, Width: 1 mm, Depth: 0.50, 0.75, 1.00, 1.25 and 1.50 mm
Boundary condition assumed	Magnetic insulation (n×A=0)
No. of mesh elements	255739
Size of mesh element at defect	0.00002 m
Degrees of freedom	1629568
Computation time	25 minutes in dual core 64 bit processor workstation with 8 GB primary memory

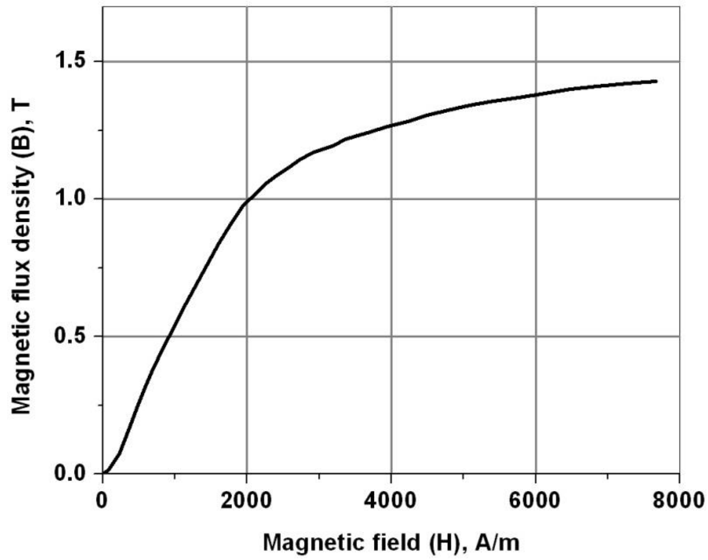

Figure 3.5 Magnetization curve for steam generator tube

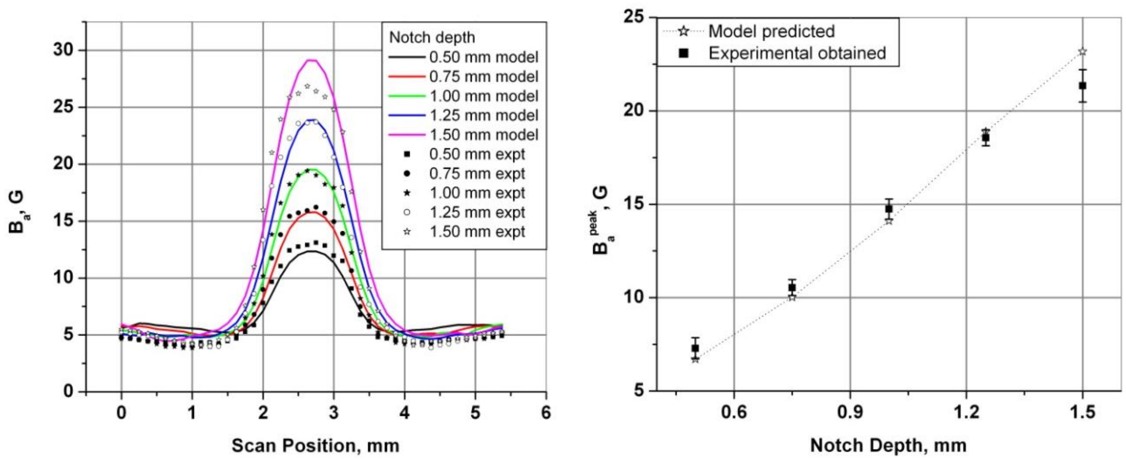

(a) (b)

Figure 3.6 Comparison of model predicted and experimentally obtained (a) MFL signals for circumferential notches and (b) its signal peak amplitudes

Chapter 4: Optimization of MFL Technique for Cuboid Geometry

4.1 Introduction

Ferromagnetic components of cuboid geometry are widely used in petrochemical and refinery industries. Common examples are carbon steel plates and storage tank floors. Carbon steel plates are also used in the flooring of above ground storage tanks (AST) [17]. Corrosion related defects are of major concern for the carbon steel floors used in these ASTs [127]. Defects can form on top and bottom surfaces of the tank floors. The defects that form on the top surface are called surface defects or near-side defects while the defects that form on the bottom surface are called sub-surface defects or far-side defects. Prolonged corrosion and growth of defects can cause leak of hazardous materials contained in the ASTs. Therefore, periodic inspection and maintenance of the floors is essential. Among NDE techniques, MFL technique is widely used to detect metal-loss defects or remaining wall thickness in the tank floors [20, 128-129]. This particular application of MFL involves locally magnetising the floor plate and measuring the leakage field just above the floor surface caused by a defect using magnetic field sensors.

Ramirez *et al.* [129] carried out experimental studies using Hall sensors to distinguish top and bottom defects of the tank floor and showed that there is a very high similarity between MFL signals belonging to the top and bottom defects. They suggested that it is not viable to use standard MFL based techniques to discriminate top and bottom defects. Liu *et al.* [20] studied the influence of specimen width on the local magnetisation and showed that different areas of tank floors do not affect the testing sensitivity, provided the thickness of the sample is same. Kasai *et al.* [14] used Hall sensor to measure both B_x and B_z components of leakage fields from flat-bottomed holes and rectangular grooves with various widths and depths in carbon steel plates of 12 mm and 22 mm thickness. They proposed a practical procedure that uses linear relationship between the MFL signal peak amplitude and defect cross-sectional area for determining the depth of the flaw or residual plate thickness in storage tank floors.

Xiao-chun *et al.* [26] used OPERA-3D FE analysis software to study the influence of permanent magnet size (width, height, pole spacing), the air gap between the magnetic pole and specimen surface in the MFL testing of tank floors. The modeling results indicated that variation of the magnet width affects the magnetisation much more than the magnet height. Also, when the floor has reached its magnetic saturation, the testing sensitivity and the SNR improve with the increase in the pole spacing and height of the magnet. Validation experiments were performed using permanent magnetic yoke and Hall sensors in 15 mm thick tank floors. Muzhitskii *et al.* [130] discussed the problems in determining the optimum sizes of magnetising systems based on permanent magnets as the strength of the magnetic fields depends on the size of the magnet. However, detailed optimization of electromagnetic yoke based MFL technique for cuboid geometry is still scarce and is required for enabling high sensitive detection of defects. In all the above mentioned studies, Hall sensors are used for detection of leakage magnetic fields from defects in cuboid shaped plates and floors.

However, since the defects can occur on the top as well as bottom surfaces of the floor, the sensitivity of the MFL technique employing Hall sensors is limited. In this context, GMR sensors are attractive, especially for detection of deep sub-surface defects.

This chapter discusses the optimization of GMR based MFL technique for high sensitive detection of surface and sub-surface defects in 12 mm thick carbon steel plates. In order to optimize the structure of the electromagnetic yoke used in the technique, 2D-FE modeling is performed. The number of GMR sensors and location of 2D GMR array sensors are optimized using 3D-FE model.

4.2 MFL Technique for Cuboid Geometry

The MFL technique proposed for cuboid geometry (steel plate) consists of a C-core electromagnetic yoke, GMR array sensor, ferromagnetic plate with defects, X-Y scanner, amplifier and personal computer. The yoke is used for uniform tangential magnetisation of the plate. GMR array sensor is used to measure the B_x component of the leakage magnetic flux by scanning the sensor array across the defect. The output from sensors is amplified and digitized for analysis and interpretation.

4.3 Modeling

2D-FE modeling has been performed to optimize the magnetising unit comprising of an electromagnetic yoke used in the MFL technique for cuboid geometry i.e. carbon steel plate. Firstly, the structure of the electromagnetic yoke has been optimized for enhanced detection of defects in the plate. Three different structures of C-core electromagnetic yoke are possible for magnetisation of the steel plate as shown in Figure 4.1. Structure 1

(Figure 4.1a) has one magnetising coil of 300 turns which is wound around the bow of the yoke. Structure 2 (Figure 4.1b) has two symmetric coils, each of 150 turns which are wound around the two legs of the yoke. Structure 3 (Figure 4.1c) has three coils- one coil of 100 turns at the bow and two coils, each of 100 turns at the legs of the yoke. The total number of turns in all the three structures is maintained the same i.e. 300 turns. In order to detect both the surface and sub-surface defects and for optimization of the yoke, 50% wall loss surface and sub-surface defects (6 mm deep in 12 mm thick plate) have been considered. The B_x component of MFL signal at the sensor location has been predicted for all the three structures and their peak amplitudes (B_x^{peak}) have been compared. The parameters used in the modeling are given in Table 4.1.

The following equation (4.1) has been solved in two dimensions using the FE method:

$$\nabla \times \left(\frac{1}{\mu_0 \mu_r} \nabla \times A \right) = J \tag{4.1}$$

where A is the magnetic vector potential, μ_r is the relative permeability and J is the current density.

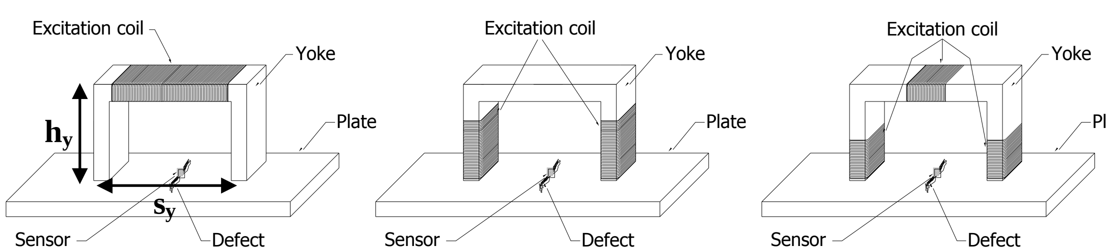

(a) Structure 1 (b) Structure 2 (c) Structure 3

Figure 4.1 Three different structures of C-core electromagnetic yoke for MFL NDE of cuboid geometry.

Table 4.1 Parameters used in the FE modeling of MFL technique for carbon steel plate.

Excitation coil	No. of turns: 300 Cross-sectional area: 50x6 mm ^{2} Current: 4 A Conductivity: 5.98x10^7 S/m
Yoke	Yoke height: 75 mm Leg spacing: 75 mm Relative permeability: 1000 Conductivity: 1.12x10^7 S/m
Steel plate	Dimensions: 240x12 mm ^{2} Relative permeability: B-H curve Conductivity: 1.71x10^7 S/m
Defect (groove)	Dimensions: 1x6 mm ^{2}
Boundary condition	Magnetic insulation (n×A=0)
No. of mesh elements	43632
Size of mesh element at defect	0.0002 m
Degrees of freedom	88723
Solver	MUMPS (direct solver)
Computation time	7.28 s in dual core 64 bit processor workstation with 8 GB primary memory

The magnetic vector potential A is computed for the model geometry and the B_x component of MFL signals for the surface and sub-surface grooves at different lift-offs are predicted. The model predicted contour lines of B_x component of magnetic flux density for the surface groove for the three structures 1, 2 and 3 are shown in Figures 4.2(a), 4.2(b) and 4.2(c) respectively. Among the three structures, structure 1 has the highest value of B_x as the direction of excitation coil is tangential resulting in higher magnetic flux density of the excitation coil along the tangential direction. In structure 2, the magnetic fields due to the excitation coils are mostly in the normal direction and cancel each other at the middle of the two poles due to the symmetrical structure of the excitation coils. Structure 3 has the magnetic fields in both the tangential and normal directions, although the field is dominant along the normal direction. Figures 4.3(a) and 4.3(b) show the model predicted B_x component of MFL signals for the surface groove and sub-surface groove respectively for the three yoke structures. The intensity of the MFL signal is found to be highest in the structure 1 and lowest in the structure 2 for both the defects. At the same time, the background magnetic field is also highest in the structure 1 and lowest in the structure 2. As expected, the intensity of MFL signal for the surface groove is higher compared to that of the sub-surface groove. However, the MFL signal for the sub-surface groove is found to be broader than that of surface groove due to divergence effect. The B_x^{peak} amplitudes of both the surface and sub-surface grooves for all the structures have been calculated and are shown in Figure 4.4. The B_x^{peak} amplitude is found to be highest in the structure 1 and lowest in the structure 2 for both the defects. This is attributed mainly to the tangential magnetisation of the steel plate in the structure 1 meeting magnetic field lines perpendicular to the defect and causing more leakage of magnetic fields from the defects. Moreover, the excitation coils in the structures 2 and 3 are distributed against the localization of a single coil in the structure 1 leading to less resultant magnetic field of the component magnetic vector fields due to the distributed coils in the structures 2 and 3. Therefore, structure 1 is expected to provide the highest detection sensitivity. Hence, structure 1 has been chosen as the optimum structure for magnetisation of the steel plates.

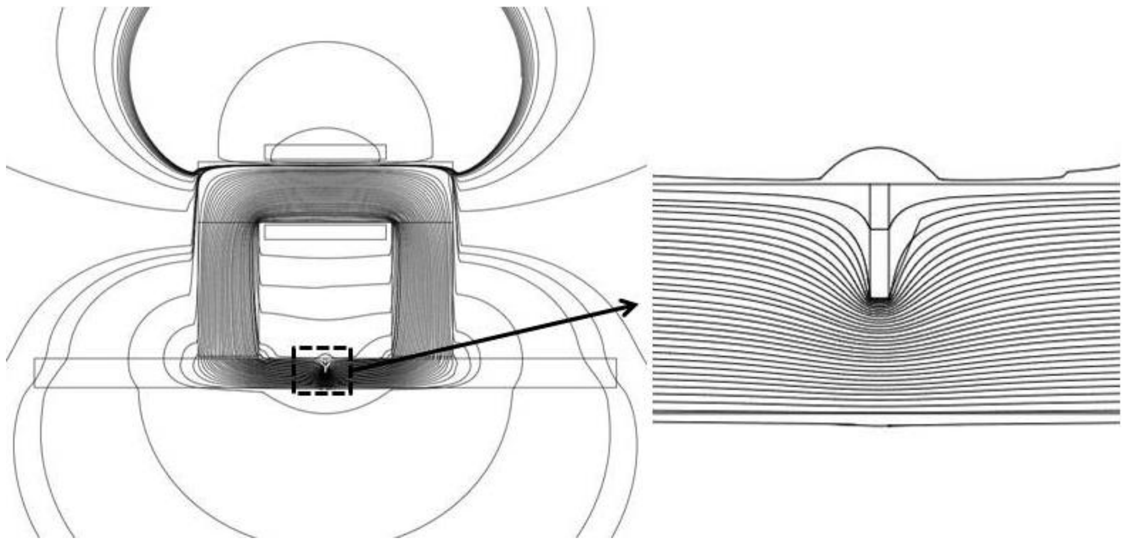

(a) Structure 1

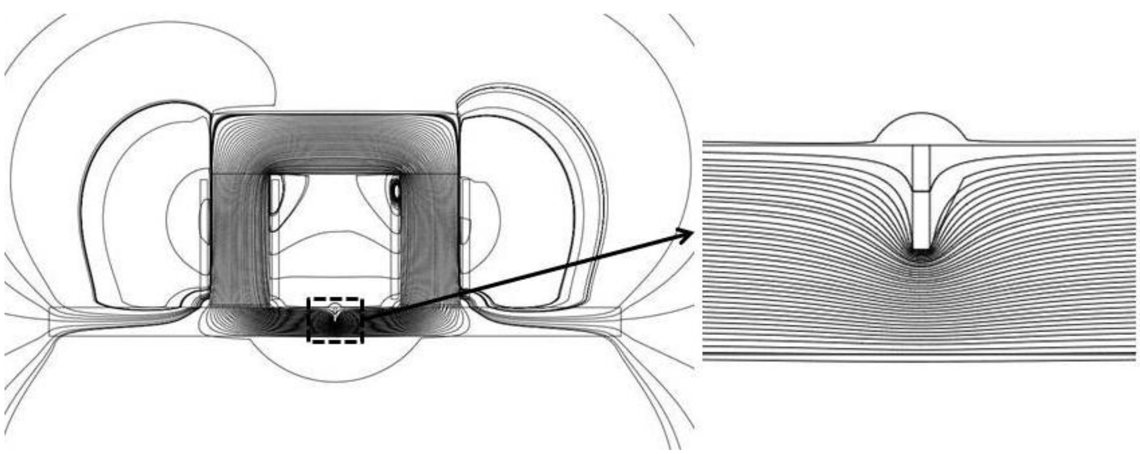

(b) Structure 2

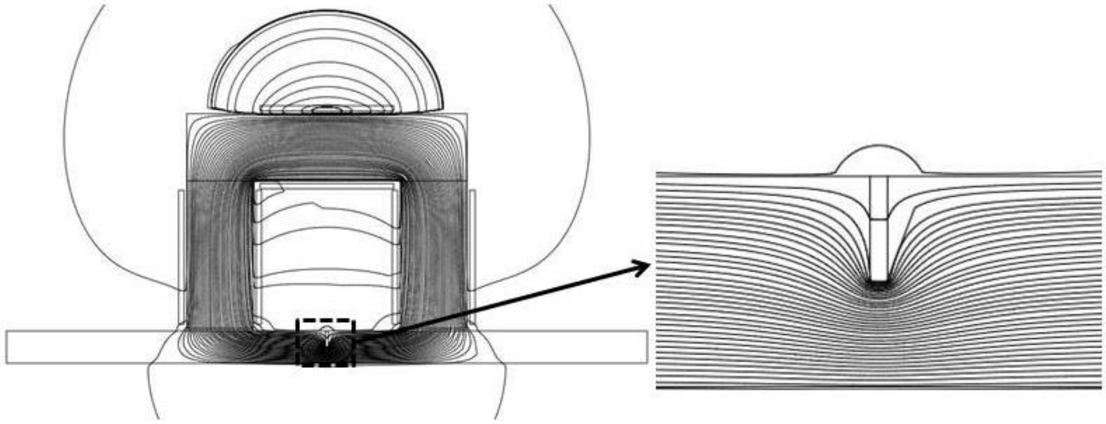

(c) Structure 3

Figure 4.2 Model predicted contour lines of B_x component of magnetic flux density from the surface groove for (a) structure 1, (b) structure 2 and (c) structure 3.

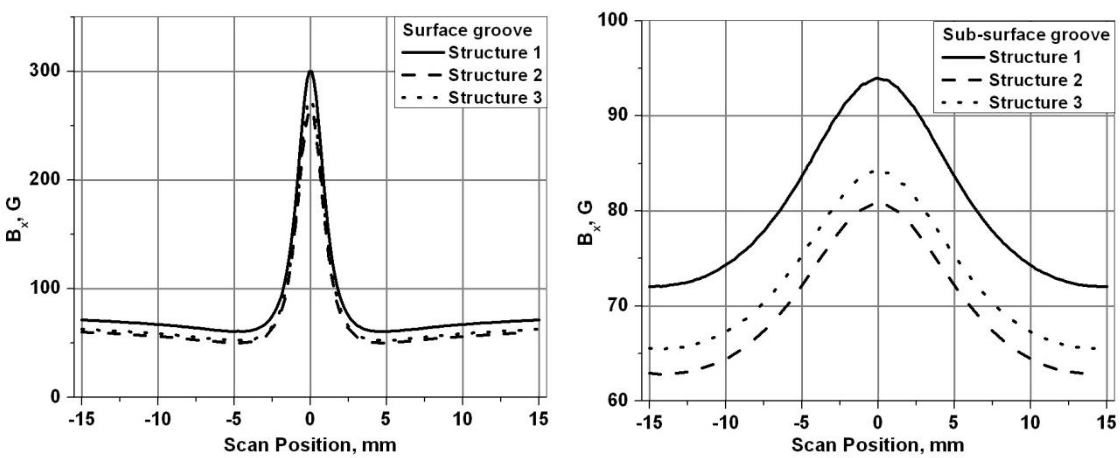

(a) (b)

Figure 4.3 Model predicted B_x component of MFL signals for (a) surface groove and (b) sub-surface groove of the three yoke structures.

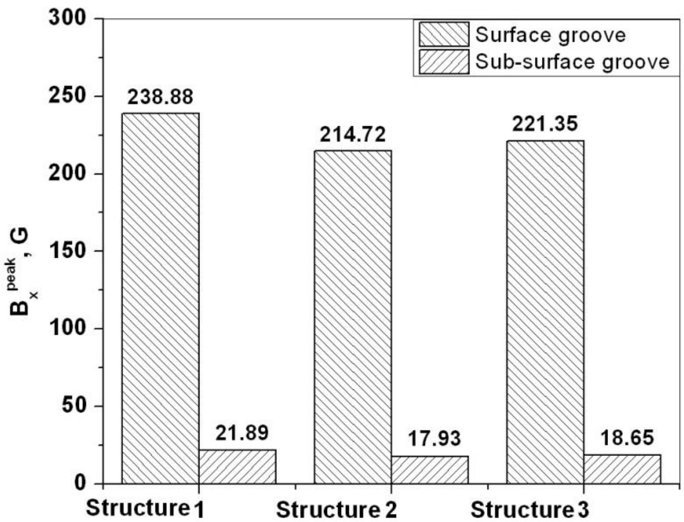

Figure 4.4 Model predicted B_x^{peak} amplitudes for surface and sub-surface grooves of the three yoke structures.

4.3.1 Optimization of Yoke Height

Optimization of yoke height (h_y) is important for enhanced detection of defects. The height of the yoke is optimized using B_x^{peak} amplitudes of the MFL signals of surface and sub-surface grooves for different heights from 55 mm to 95 mm in steps of 10 mm as shown in Figure 4.5(a). The B_x^{peak} amplitude is found to decrease with the increase in yoke height. This is attributed to the increase in length (L) of magnetic circuit with the increase in yoke height which in turn, increases magnetic reluctance ($\mathcal{R}$) given by $\mathcal{R}$=L/$\mu_0\mu_r$A (A, being the cross sectional area of the yoke). The increase in magnetic reluctance leads to reduction of magnetic flux (Φ=MMF/$\mathcal{R}$, MMF being the magnetomotive force which is equal to NI ampere-turns). However, the increase in reluctance is very small as the permeability of the mild steel yoke is very high. As a result, the B_x^{peak} amplitude is found to be almost constant for all heights of the yoke and this observation is similar to that reported in [26]. Hence, a height of 75 mm has been chosen as the height of the yoke.

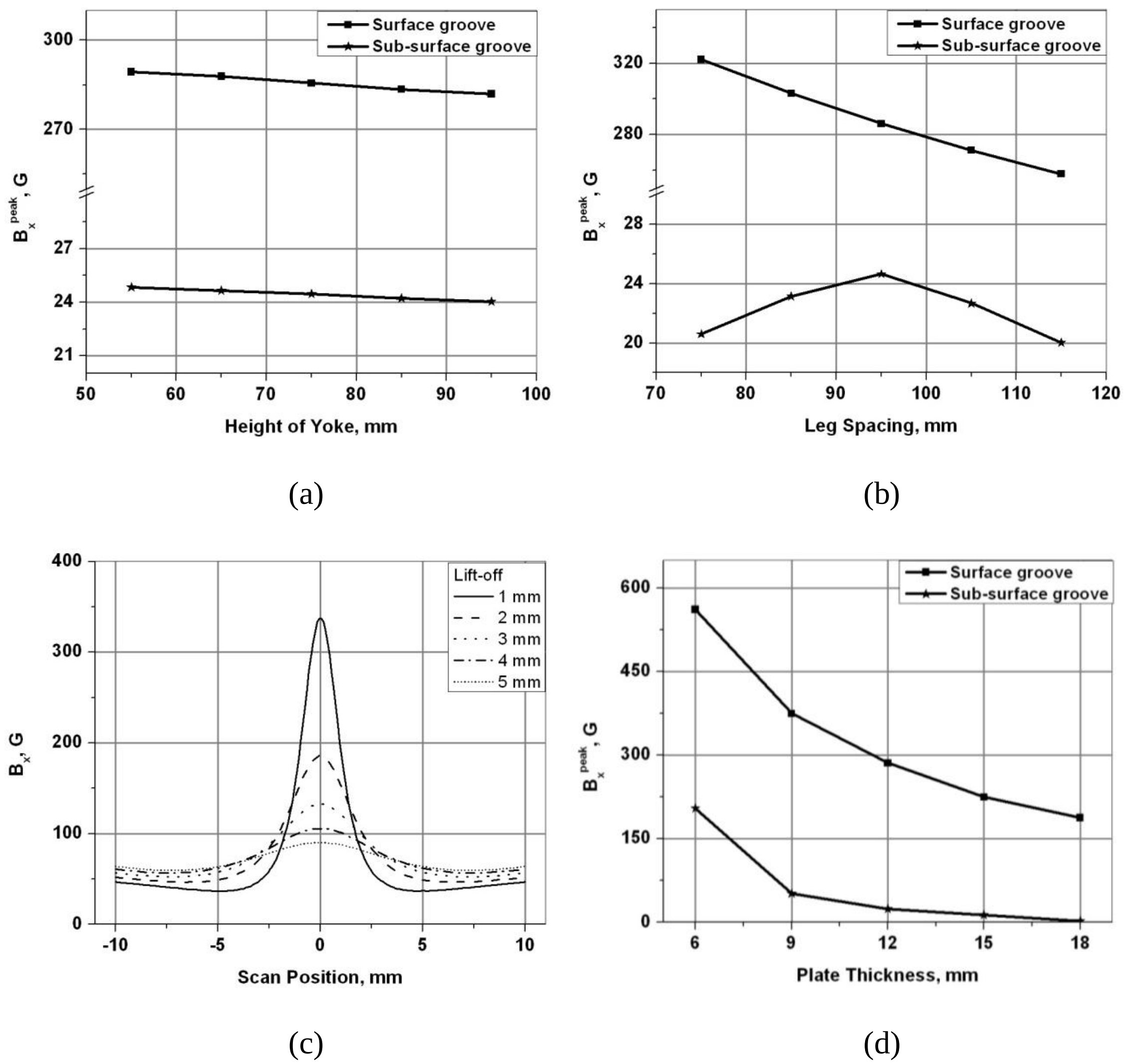

(a) (b)

(c) (d)

Figure 4.5 Model predicted variation of B_x^{peak} amplitudes with (a) height, (b) leg spacing of yoke, (c) lift-off and (d) plate thickness for the surface and sub-surface grooves.

4.3.2 Optimization of Leg Spacing

The leg spacing (s_y) of the yoke is optimized for obtaining uniform tangential magnetisation of the plate between the two legs of the yoke so that sufficient detectable magnetic fields are leaked out of the defects. The leg spacing is optimized using B_x^{peak} amplitudes of the MFL signals of the surface and sub-surface grooves for different leg spacing from 75 mm to 115 mm in steps of 10 mm as shown in Figure 4.5(b). The B_x^{peak} amplitude of the MFL signal for surface groove is found to decrease with the increase in leg spacing. This is primarily due to the increase in magnetic reluctance with the increase in leg spacing of the yoke which leads to reduction in magnetic flux (and hence, leakage magnetic flux) with the leg spacing. Similarly, the B_x^{peak} amplitude of the MFL signal for sub-surface groove is found to decrease with the leg spacing greater than 95 mm. However, at smaller leg spacing (< 95 mm), signal amplitude of the sub-surface groove is found to decrease due to less magnetic flux leading at the location of sub-surface groove and limited space for leaking of distributed and broad MFL signal from the sub-surface groove. Hence, a distance of 95 mm has been chosen as the optimum leg spacing of the yoke for this technique, as it enables detection of both surface and sub-surface defects. It also enables detection of leakage fields at higher lift-offs (Figure 4.5c). However, the optimization of the leg spacing and hence the yoke depends upon the thickness of the plate as shown in Figure 4.5(d). As can be seen, the MFL signal peak amplitudes of both the surface and sub-surface grooves decrease with the increase in plate thickness due to reduction in induced magnetic flux density with the increase in plate thickness.

4.3.3 Optimization of Magnetizing Current

The magnetising current is optimized for obtaining sufficient detectable leakage magnetic fields from both the surface and sub-surface defects. Figure 4.6 shows the model predicted B_x^{peak} amplitudes of MFL signals as a function of magnetising current. As can be seen, B_x^{peak} increases with the increase in magnetising current and the rate of increase of B_x^{peak} amplitude decreases at higher currents following the non-linearity of magnetization curve. However, at currents > 4 A there is a likelihood of saturation of GMR sensor for leakage fields from deep surface-breaking notches. In view of this, 4 A current is chosen as the optimum current in this study for detection of both surface and sub-surface defects. Thus, the optimized magnetising unit for MFL NDE of 12 mm thick steel plates is structure 1 with length 120 mm, width 50 mm, height 75 mm, leg spacing 95 mm, winding 300 turns and magnetising current 4 A. Experimental measurements have been made using this optimized magnetising yoke in this technique.

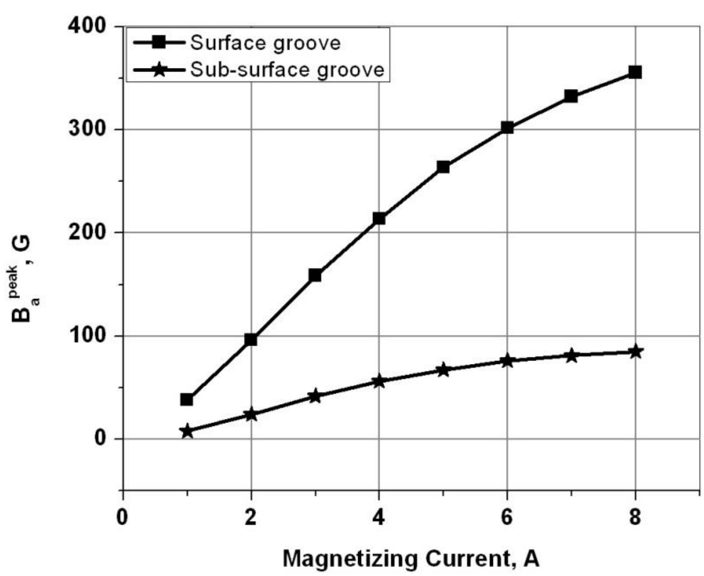

Figure 4.6 Model predicted B_x^{peak} amplitudes of MFL signals as a function of magnetising current.

4.4 Experimental Setup

The schematic of the experimental setup used for the MFL measurements on a carbon steel plate of cuboid geometry using the optimized yoke is shown in Figure 4.7. This consists of a yoke, GMR sensor, ferromagnetic specimen with defects, X-Y scanner, amplifier and personal computer. With electromagnetic yoke centered over the defects, measurements are made by scanning the GMR sensor across the defects in steps of 0.2 mm. At sensor location, the B_x component (along the scan direction) of the leakage magnetic flux is measured using the GMR sensor. The sensor output is first amplified by a low noise amplifier consisting of a differential amplifier, a notch rejection filter at 50 Hz followed by a low-pass filter of 100 kHz and a single ended variable gain amplifier with DC suppression for enhancing the signals. The variable gain amplifier is set such that it amplifies the sensor output 8 times. This output is digitized using a DAQ system of 16-bit A/D conversion card (PCI-1716) and then, stored in the computer for subsequent analysis.

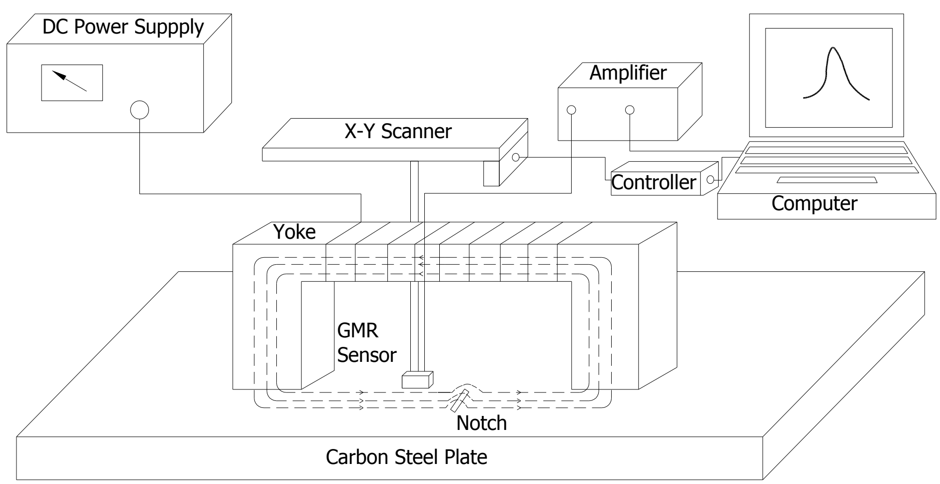

Figure 4.7 Schematic of experimental setup used for MFL measurements on carbon steel plate.

For this study, GMR bridge sensors (AA003-02) manufactured by NVE Associates are used. Because of the bridge circuit (Figure 4.8a), GMR sensor measures the differential output voltage of the two sensing elements as a function of resistance variation and ensures high stability with low noise. The GMR sensor has a maximum hysteresis of 4% unit [51]. The output characteristic of the GMR sensor for calibrated magnetic fields is shown in Figure 4.8(b). The sensitivity of the GMR sensor is found to be 260 VT^{-1} at 5 V biasing voltage and the linear response is within the range of 0.2 mT to 1.3 mT. This GMR sensor saturates at magnetic fields greater than 3 mT.

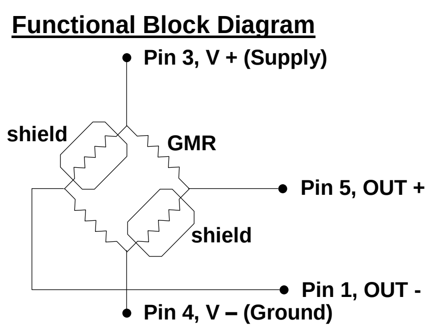

(a)

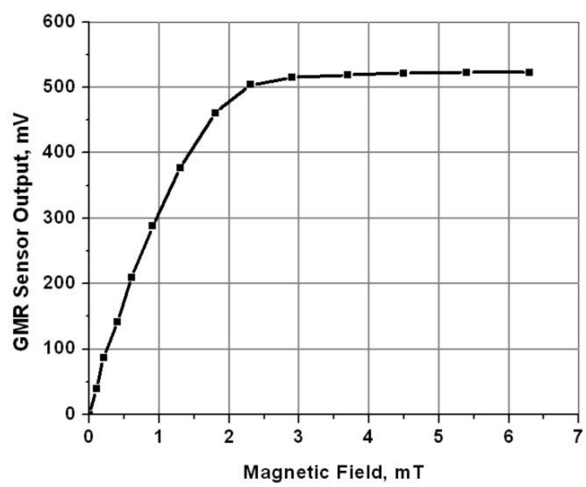

(b)

Figure 4.8 (a) Functional block diagram of GMR bridge sensor and (b) GMR sensor response characteristic.

4.5 Reference Defects

The specimens used in this study are five carbon steel plates (thickness, 12 mm) each having two 15 mm long electro-discharge machining (EDM) notches of widths of 0.5 mm and 1 mm as shown in Figure 4.9 and of different depths (Table 4.2). With the notches on the GMR sensor side and on the opposite of sensor side (plate inverted), surface (Figure 4.10a) and sub-surface notches (Figure 4.10b) are examined, respectively. In the case of sub-surface notches, a definite location *h* below the scanning surface exists for each notch. The physical lift-off between the GMR sensing layer and the specimen surface is 0.3 mm.

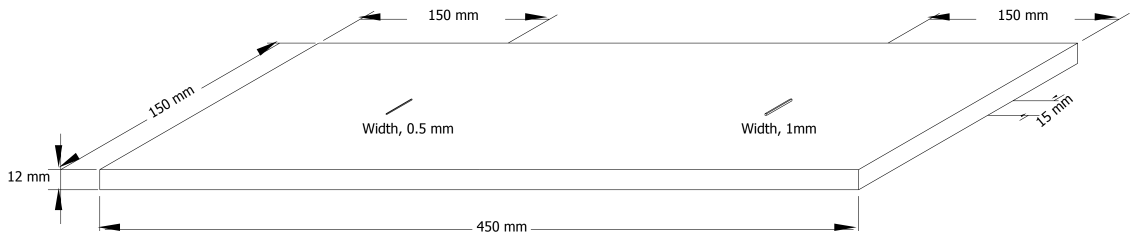

Figure 4.9 Carbon steel plate specimen with EDM notches.

Table 4.2 Details of surface and sub-surface notches in 12 mm thick carbon steel plates

Plate number	**Notch type**	**Length, l (mm)**	**Width, w (mm)**	**Depth, d (mm)**	**Location below surface, h (mm)**
Plate 1	Surface	15	0.5	1.10	0
			1	0.93	0
	Sub-surface	15	0.5	1.10	10.90
			1	0.93	11.07
Plate 2	Surface	15	0.5	1.74	0
			1	1.72	0
	Sub-surface	15	0.5	1.74	10.26
			1	1.72	10.28
Plate 3	Surface	15	0.5	3.38	0
			1	3.32	0
	Sub-surface	15	0.5	3.38	8.62
			1	3.32	8.68
Plate 4	Surface	15	0.5	5.84	0
			1	5.76	0
	Sub-surface	15	0.5	5.84	6.16
			1	5.76	6.24
Plate 5	Surface	15	0.5	8.84	0
			1	8.90	0
	Sub-surface	15	0.5	8.84	3.16
			1	8.90	3.10

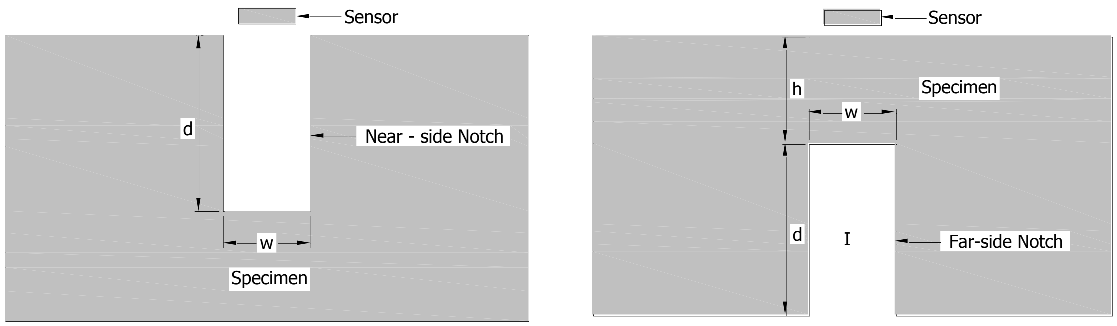

(a) (b)

Figure 4.10 Schematic showing (a) surface notch (near-side) and (b) sub-surface notch (far-side).

4.6 Experimental Results

4.6.1 Surface Defects

The GMR sensor output for surface notches of different depths for two different widths 0.5 mm and 1 mm, after background removal are shown in Figures 4.11(a) and 4.11(b) respectively. It can be seen that the GMR sensor detected all the surface notches and the intensity of GMR sensor output increases with notch depth due to higher magnetic reluctance from the deeper notches. However, when the notch depth increases beyond 5.84 mm, the leakage field becomes relatively insensitive to further increase in depth and this observation is in agreement with that reported in [3]. This is more prominently seen in Figure 4.11(a) in the case of 5.84 mm and 8.84 mm deep notches. With the increase in depth, an increase in lateral spread of the MFL signals has been observed. The amplitude of GMR signals from 0.93 mm deep (width 0.5 mm) and 1.1 deep (width 1.0 mm) surface notches are approximately 4 times the background signals from notch-free regions.

In order to assess the detection performance of the technique, signal and noise amplitudes have been measured and the signal-to-noise ratio (*SNR*) is determined for all the notches using *SNR=20log(S/N)*, where *S* is the amplitude of MFL signal of a notch and *N* is the amplitude of MFL signal in notch-free region (noise) of the plate. The SNR of the shallowest notch (0.93 mm deep) is found to be 12.1 dB.

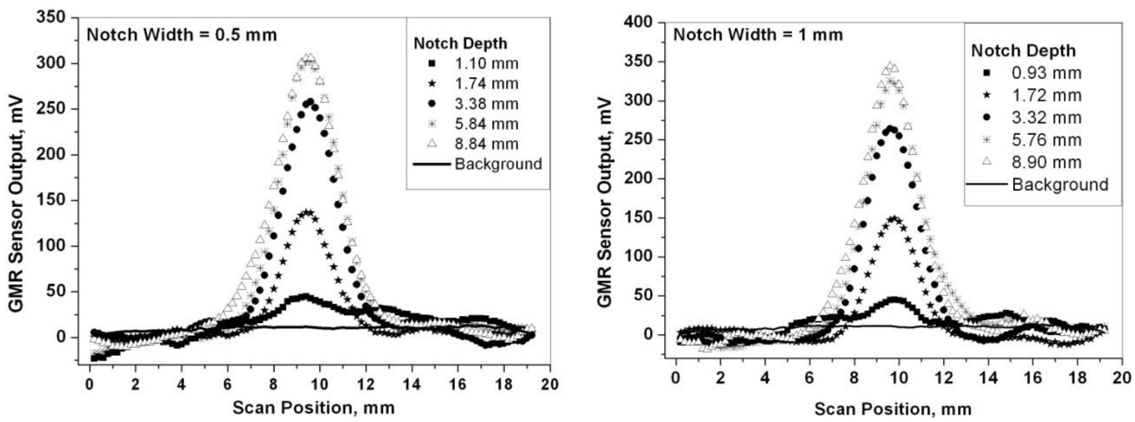

(a) (b)

Figure 4.11 GMR sensor signal output for various surface notches of (a) 0.5 mm width and (b) 1.0 mm width.

The GMR sensor signal amplitude as a function of surface notch depth for two different widths is shown in Figure 4.12. It is seen that the amplitude of MFL signal increases with notch depth and notch width. The influence of notch depth is seen more prominent than that of the notch width. The rate of increase in signal amplitude with notch depth showed nearly two-slope behavior as depicted in Figure 4.12 (dotted line). Larger slope is observed upto ~ 3 mm depth and thereafter, it is reduced. This reduction in the slope at higher values of notch depth is due to the significant contribution of induced volume magnetic charge density near the defect which leads to leakage of significant amount of magnetic flux to the other side of the plate. As expected, with increasing width of notch, there is an increase in MFL signal amplitude.

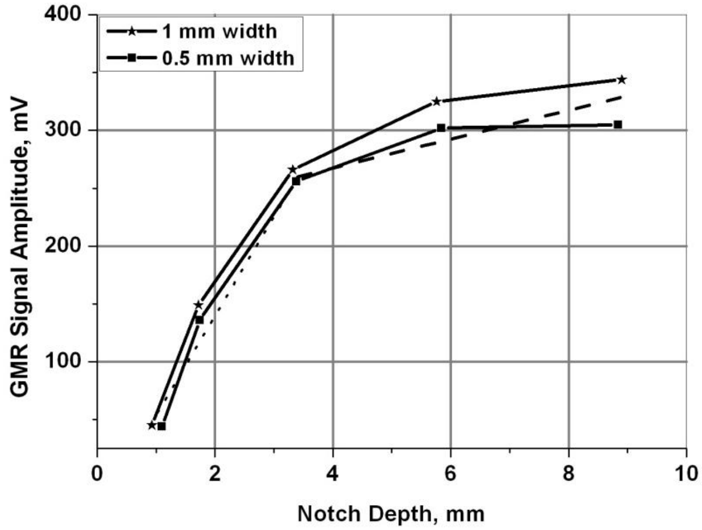

Figure 4.12 GMR signal amplitude as a function of depth for surface notches (dotted line shows the approximated two-slope behavior).

4.6.2 Sub-surface Defects

The GMR sensor output for sub-surface notches located at different depths for widths 0.5 mm and 1 mm are shown in Figures 4.13(a) and 4.13(b) respectively. It can be seen that GMR sensor detected sub-surface notch located at 11.07 mm (depth 0.93 mm) below the surface and this is a first time result. For this notch, the GMR signal is 3.92 times the background signal from the notch-free regions. This high sensitive detection of deep sub-surface notch is possible due to the optimization of high sensitive GMR sensor based MFL technique together with the low noise differential amplifier. The GMR sensor signal amplitude as a function of notch location below the surface is compared for two different notch widths and is shown in Figure 4.14. It can be observed that the leakage field strength is decreased with increase in notch location from the surface and as a result, the amplitude of the MFL signal is decreased. Once again, two-slope behavior is observed for the rate of decrease in signal amplitude with notch location. The GMR sensor signal amplitudes are found to be higher for wider notches. The lateral extent of signals is found to increase with increasing *h* due to the inherent divergence effect. The lateral extent of the signals can be reduced by decreasing the leg spacing of magnetising yoke (refer Figure 4.5b) and by increasing the magnetising current (refer Figure 4.6) which will also increase the background noise. However, from Figures 4.13 and 4.14, it is evident that resolution in depth and position evaluation becomes poor when *h* increases.

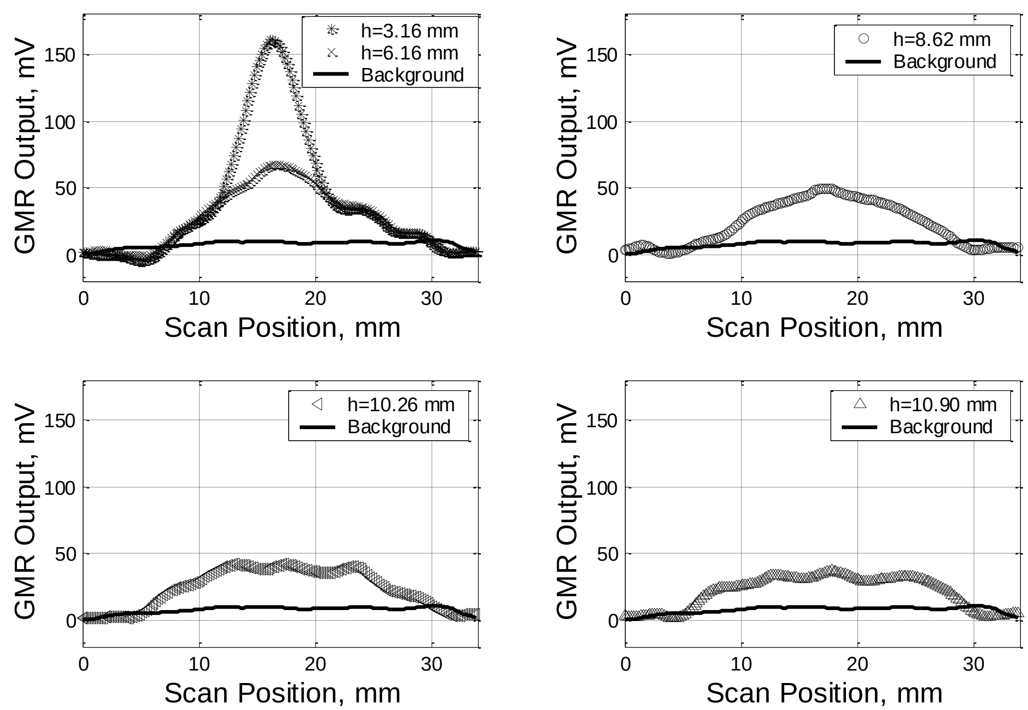

(a)

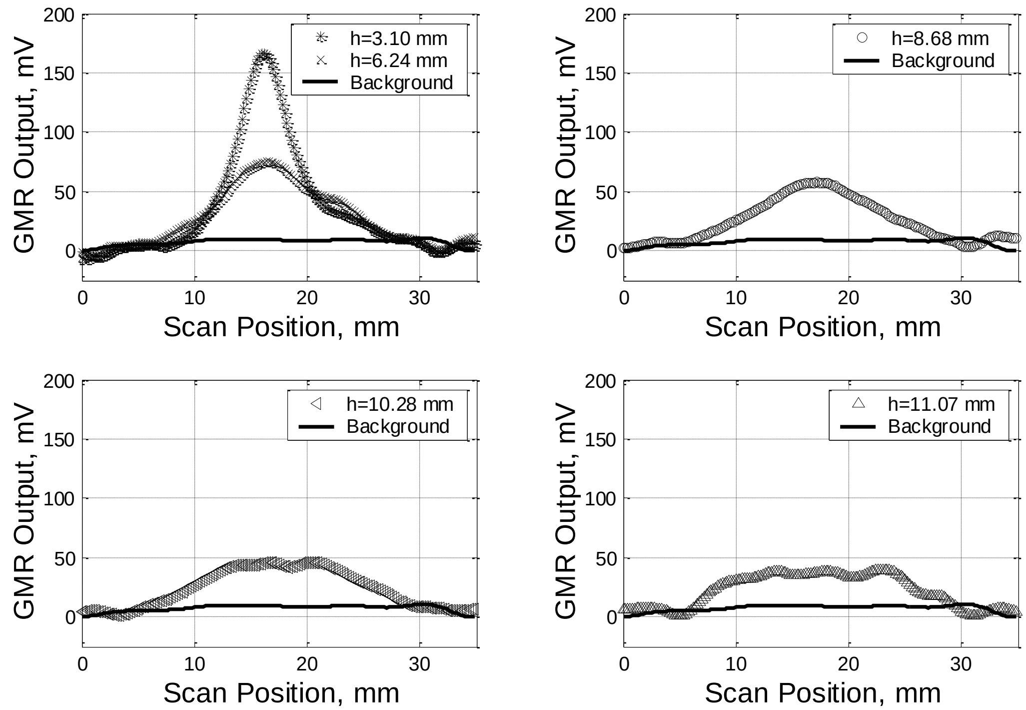

(b)

Figure 4.13 GMR sensor signal response for sub-surface notches of (a) 0.5 mm width and (b) 1.0 mm width located at different depths below surface.

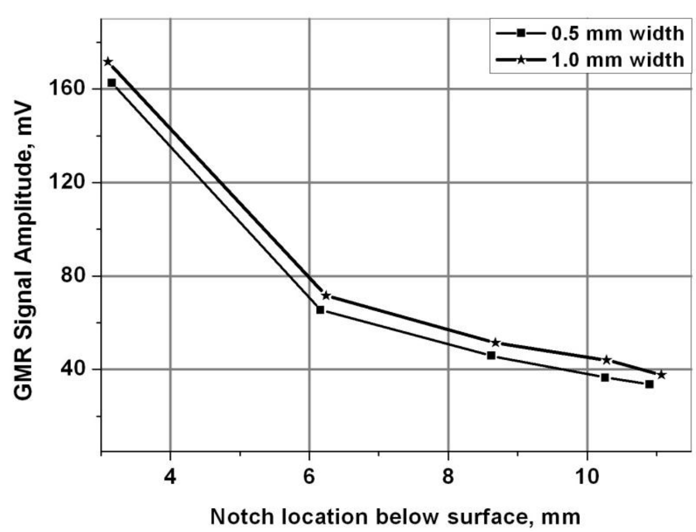

Figure 4.14 GMR sensor signal amplitude for sub-surface notches as a function of notch location below the surface.

4.6.3 Influence of Lift-off on MFL Signals

The influence of lift-off on the sensitivity of the MFL technique has been presented in this section. The response of the GMR sensor with lift-off (lifting only the GMR sensor from the plate surface) for sub-surface notches (length 15 mm, width 1 mm) located at different depths below surface is shown in Figure 4.15. As can be observed, the GMR sensor has detected all the notches upto 3 mm lift-off. At low lift-offs, the GMR signal amplitude decreases drastically and then, it decreases gradually. Thus, this section demonstrates that the optimized MFL technique can be used for non-contact and high sensitive detection of surface and sub-surface defects in the plates.

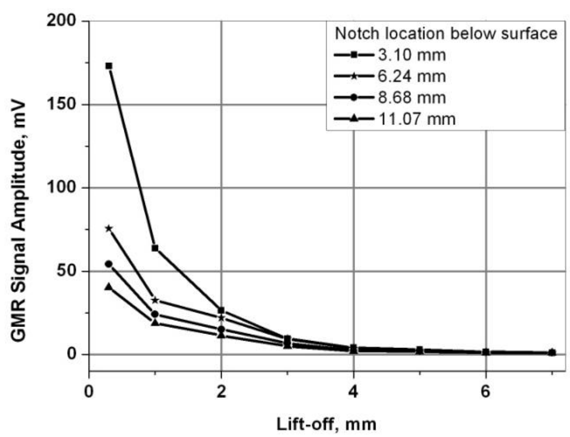

Figure 4.15 Variation of GMR signal amplitude with lift-off for different sub-surface notches in 12 mm thick carbon steel plates.

4.6.4 Influence of Inclined Defects on MFL Signals

The influence of inclined defects on the sensitivity of the MFL technique has also been studied. Figure 4.16(a) shows the response of the GMR sensor for notches (length 15 mm, width 2 mm, depth 6 mm) of 0º, 15º, 30º and 60º inclinations. As expected, MFL signals are found to be asymmetric for inclined notches. The intensity of MFL signals for the notches is found to decrease with increase in angle of inclination. Shift in signal peak amplitude of MFL signals is also observed. In order to classify inclined or non-inclined defects, the following nine parameters (shown in Figure 4.16b) are determined from the measured MFL signals:

i) Difference in peak amplitudes (B_{xl}^{peak} - B_{xr}^{peak})

ii) Full width at half maximum (FWHM)

iii) Rising slope

iv) Falling slope

v) Peak position

vi) Area under the signal

vii) Angle at signal peak

viii) Skewness and

ix) Kurtosis

In this study, the FWHM is taken as the full width at the half of the average peak amplitudes of B_{xl}^{peak} and B_{xr}^{peak}. The Skewness and Kurtosis are defined as [131],

$$Skewness = \frac{\sum_{i=1}^{N}(x_i-\mu)^3}{(N-1)\sigma^3} \text{ and } Kurtosis = \frac{\sum_{i=1}^{N}(x_i-\mu)^4}{(N-1)\sigma^4} - 3$$

where μ is the mean and σ is the standard deviation of the distribution with variable *x*.

Figure 4.16(c) shows the variation of difference in peak amplitudes (B_{xl}^{peak} - B_{xr}^{peak}) due to change in the inclination angle of the notches. It is observed that the asymmetry increases with the increase in angle of inclination. Skewness and kurtosis of the MFL signals of inclined notches have been calculated and determined the differential skewness and kurtosis with respect to the 0º inclination (non-inclined) notch. Figure 4.16(d) shows the variation of differential skewness as a function of angle of inclination of notches. As can be seen, the differential skewness increases with the increase in angle of inclination. However, kurtosis shows very little change for small angle of inclinations. Among the nine parameters, skewness has been found to be a better parameter for classification of inclined or non-inclined defects. Thus, the optimized MFL technique enables the sensitive detection of inclined defects through the asymmetric behavior of MFL signals. This has been verified with the model prediction which is discussed in the later section.

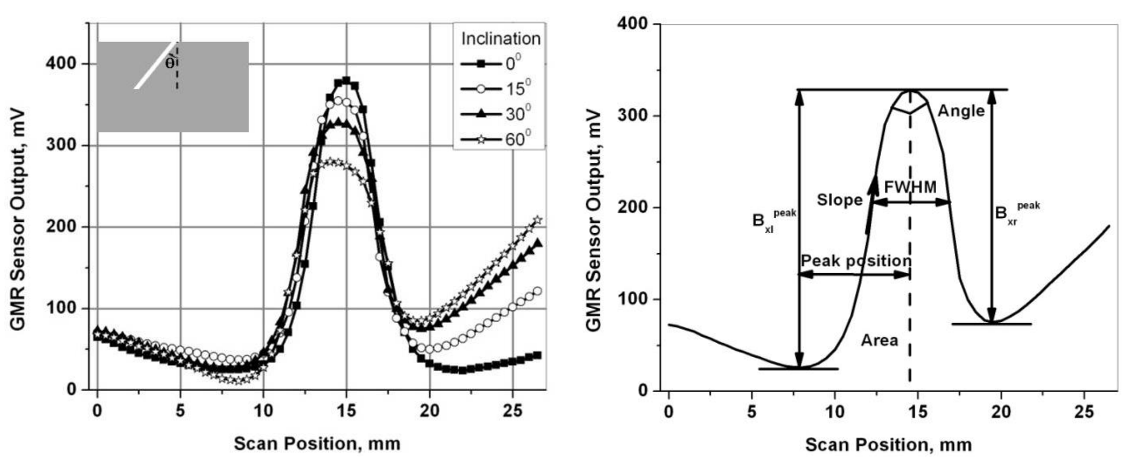

(a) (b)

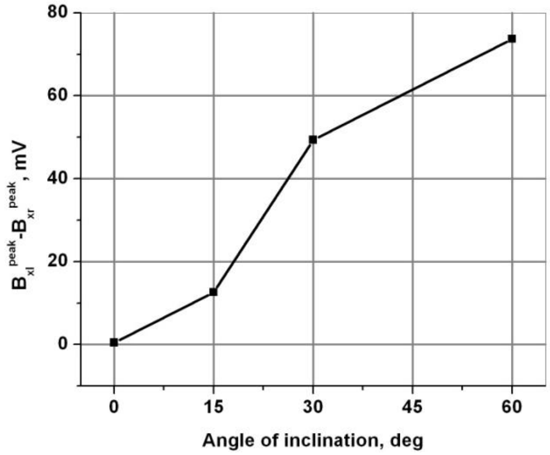

(c)

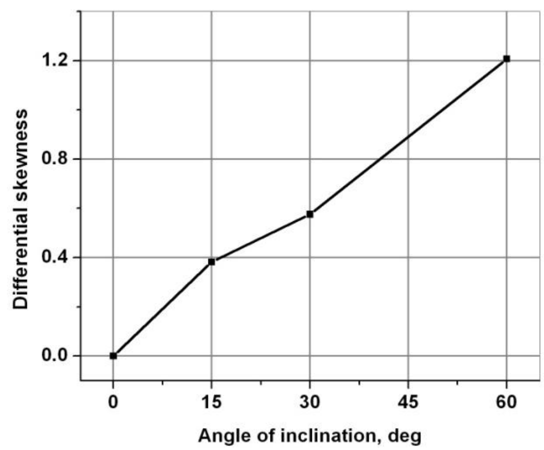

(d)

Figure 4.16(a) Measured GMR sensor signal response for inclined notches, (b) parameters determined from the measured MFL signals, (c) signal asymmetry and (d) differential skewness as a function of angle of inclination of notches.

4.6.5 Influence of Interacting Defects on MFL Signals

Figure 4.17(a) shows the response of the GMR sensor for interacting notches (length 15 mm, width 1 mm, depth 6 mm) with notch-to-notch separations of 2.5 4, 6, and 8 mm. As can be seen, the optimized MFL technique can resolve notches separated by a gap of 2.5 mm. The intensity of MFL signal decreases with the decrease in notch-to-notch separation due to the effect of mutual interaction. The separation of peak positions are nearly matching with the notch-to-notch separations. In order to distinguish interacting defects from non-interacting defects, ratio of average B_x^{peak} amplitudes of outer and inner flanks has been calculated and the result is shown in Figure 4.17(b). At low separations (2.5 mm and 4 mm), the notches are strongly interacting and then, it interacts weakly. Finally, the notches are not interacting at 6.7 mm separations. This observation is in agreement with the minimum of 5.6 mm times hole-to-hole separations measured at 1.5 mm lift-off using Hall sensors [132]. The variation is attributed to the decrease in signal amplitude and hence less separations at higher lift-offs. Further, the shape of B_x-B_z locus pattern is analyzed by measuring both B_x and B_z components of magnetic flux from defects using two separate GMR sensors. Locus patterns are observed to be distorted for interacting defects. Thus, the optimized MFL technique enables the sensitive detection of interacting defects through the ratio of peak amplitudes and distorted behavior of B_x-B_z locus pattern in MFL signals.

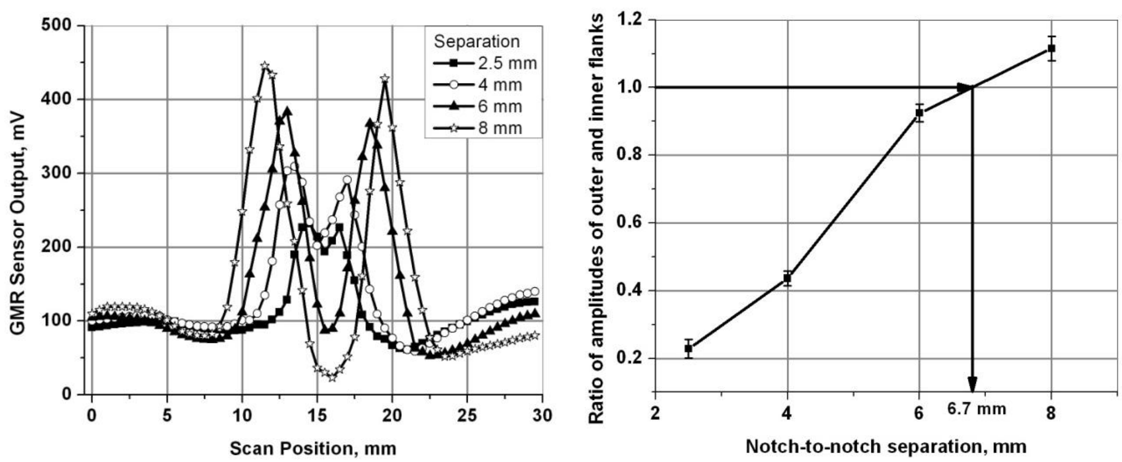

(a) (b)

Figure 4.17(a) Measured GMR sensor signal response for interacting notches and (b) ratio of peak amplitudes of outer and inner flanks as a function of notch-to-notch separations.

4.6.6 Validation

The model predicted characteristics of the MFL signals have been validated by experiments using a GMR sensor scanned over the plate. The comparison of model predicted and experimentally measured MFL signal amplitudes of sub-surface notches as a function of notch location below the surface is shown in Figure 4.18(a). As can be seen, the MFL signal amplitude decreases with the increase in notch location below the surface in both the cases. The rate of decrease in signal amplitudes with notch location showed different slope beyond 6.24 mm (notch depth, 5.76 mm ~ 50% wall loss) as the significant amount of flux is leaked to the other side of the plates. However, the experimentally measured MFL signal amplitudes of notches with notch location beyond 6.24 mm are found to be larger than that of the model predicted signal amplitudes. The difference in signal amplitudes beyond 6.24 mm location may be attributed to the change in lift-off during experimental measurement.

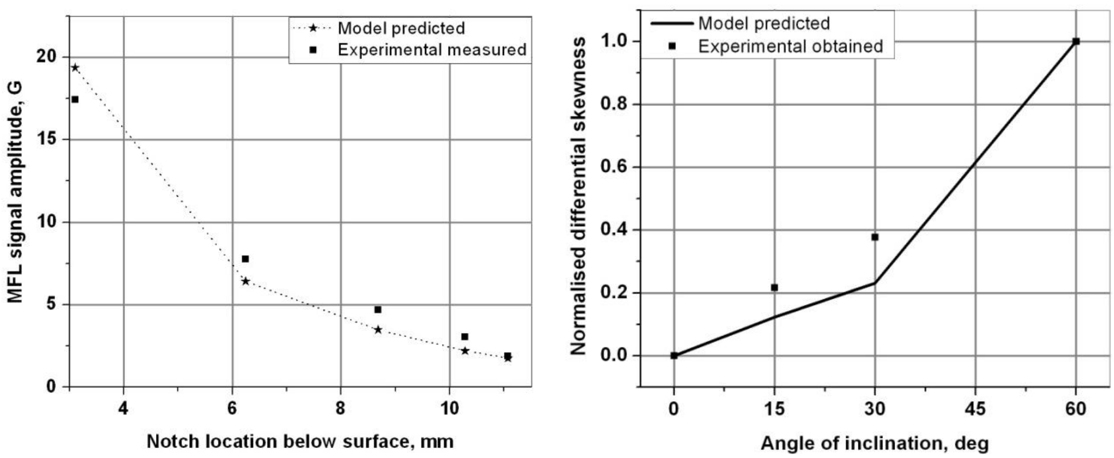

(a) (b)

Figure 4.18 Comparison between the model and experimentally obtained (a) MFL signal amplitude as a function of notch location below the surface for sub-surface notches and (b) differential skewness as a function of angle of inclination for inclined notches.

In the case of inclined defects, the model predicted and experimentally measured differential skewness values as a function of angle of inclination are compared in Figure 4.18(b). In both the cases, differential skewness increases with the increase in angle of inclination due to increase in asymmetry of MFL signals of inclined notches. Further, the differential skewness obtained from the experimental graph for 5º, 45º and 75º inclinations are found to be 0.07, 0.68 and 1.31 respectively while the differential skewness predicted from the 3D-FE model for 5º, 45º and 75º inclinations are 0.04, 0.61 and 1.39 respectively. At 5º inclination, the error for classification is 42% while, at 45º and 75º inclinations, the errors are 10% and 6% respectively. Thus, the angle of inclination (> 10º inclination) can be accurately classified using skewness.

4.7 Development of 2-dimensional GMR Array Sensors

For fast inspection of the carbon steel plates, sensing unit consisting of array sensors is essential to facilitate rapid scanning of surfaces with the coverage of a large area of the plate. Rigid 2D arrays of GMR sensors are attractive for fast inspection of the flat surface plates. Further, optimization of the number of GMR elements and locations of 2D arrays between the two legs of the electromagnetic yoke is inevitable for enhanced and reliable detection of defects. For optimization of the sensing unit, 3D-FE modeling has been performed. Equation 4.1 with the magnetic insulation boundary condition has been solved in three dimensions. The computation time for solving the equation 4.1 with 255528 numbers of tetrahedral elements is 21 minutes. Figure 4.19(a) shows the model predicted surface plot of B_x component of the magnetic flux density between the two legs of the yoke. As can be seen, the magnetic flux density is nearly uniform for an optimum area of 60×25 mm^2 (dotted region in Figure 4.19a).

The model predicted region can easily accommodate 16 GMR sensors. Hence, a 2D array of 4x4 GMR sensors has been fabricated (Figure 4.19b) and used for imaging of defects in the plate. Each sensor element in the array has a common power input of

5V, and the array has 16 differential outputs. The overall size of the sensor array is 20×17 mm^2. The centre-to-centre distances (pitch) between two consecutive sensors along the length and width directions are 5.5 mm and 4 mm respectively. The GMR sensors measure the B_x component of leakage flux from defects in the plate. The output from the array sensors is acquired and analyzed using a LabVIEW based data acquisition system incorporating averaging and low pass filter to minimize noise.

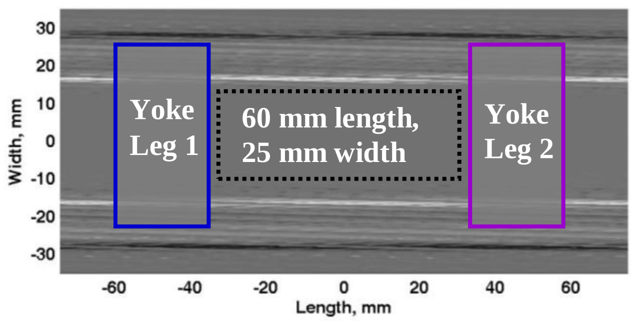

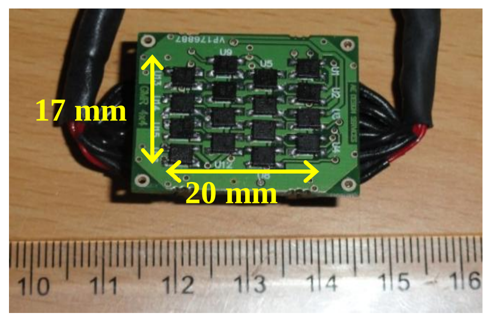

(a) (b)

Figure 4.19 (a) Model predicted magnetic flux density between the legs of the electromagnetic yoke (b) the photograph of fabricated 2D array of 4x4 GMR sensors.

The performance of the 2D array of 4x4 GMR sensors has been evaluated by measuring the B_x component of leakage fields from surface defects in the plate. Figure 4.20(a) shows the typical output of the 16 element GMR array sensor scanned across a notch (length 15 mm, width 1 mm and depth 3.32 mm). In Figure 4.20(a), we can see the output of all the 16 GMR sensors. As expected, the output of GMR sensors is found to be dependent on the position of the sensors. The GMR sensors output are processed and MFL image of the notch is obtained as shown in Figure 4.20(b). As can be seen, it is possible to obtain spatial information of the notch from the MFL image produced by a single line scanning of the sensor array over the notch.

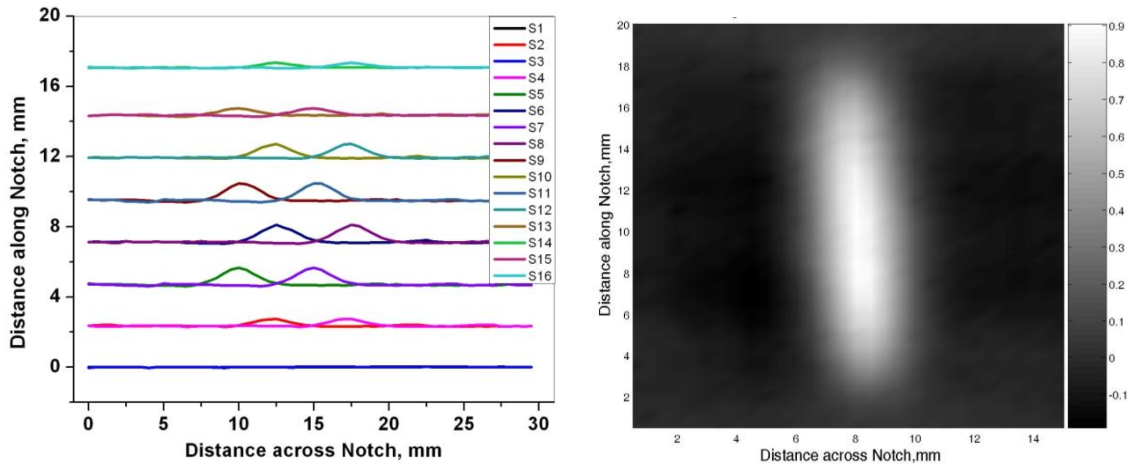

(a) (b)

Figure 4.20 (a) 16 element 2D GMR array sensor response for a 3.32 mm deep surface notch and (b) its corresponding MFL image.

4.8 Conclusions

- ✓ An MFL technique comprising of electromagnetic yoke and GMR array sensor has been proposed for high sensitive detection of surface and sub-surface defects in carbon steel plates of cuboid geometry. The structure of the magnetising yoke and the important parameters such as leg spacing, height and magnetising current of the yoke, number and location of GMR sensors used in the MFL technique have been optimized.
- ✓ The optimized technique is capable of detecting a shallow surface notch of 0.93 mm depth and a sub-surface notch located 11.07 mm below the measurement surface in 12 mm thick plate.

- ✓ Two-slope behavior is observed for the rate of change in GMR sensor signal amplitudes with notch depth for surface notches and notch location for sub-surface notches.
- ✓ The technique can be used for non-contact detection of surface and sub-surface defects in the plates upto 3 mm lift-off.
- ✓ Skewness has been found to be a better parameter for classification of inclined or non-inclined notches. It can classify inclined (>10º inclination) notches with an error of 10%.
- ✓ The technique can resolve notches separated by a gap of 2.5 mm.
- ✓ The model predicted features of the MFL signals have been experimentally validated for a few cases.
- ✓ A 2D array of 4x4 GMR sensors has been designed and fabricated for enabling rapid detection and imaging of defects in the carbon steel plate.

Chapter 5: Optimization of MFL Technique for Solid Cylindrical Geometry

5.1 Introduction

Ferromagnetic steel wire ropes of solid cylindrical geometry are widely used for material handling in mines and hauling of men in ski-lift operations [2, 133]. In wire ropes, two types of damage viz., local flaws (LF) and loss of metallic cross-sectional area (LMA) occur mainly due to corrosion and wear [29, 134]. LFs are external and internal discontinuities such as broken wires, cracks and corrosion pitting. Wire breaking can occur due to fatigue, inter-strand nicking or martensitic embrittlement. LMAs are distributed defects such as missing of wires caused by corrosion, abrasion and wear resulting in loss of cross-sectional area. Periodic inspection of wire ropes is important to ensure the structural integrity and to take corrective actions. Non-destructive inspection of wire ropes is challenging due to their heterogeneous structure, multiplicity, uncertainty of broken wires and hostile working environment.

Among various NDE techniques, visual and MFL techniques are widely used for monitoring the health of steel wire ropes [135-136]. Although visual inspection is simple and does not require special instrumentation, it is not suited for monitoring the internal deterioration of ropes. On the contrary, the MFL technique is capable of detecting both LF and LMA type defects in wire ropes [136]. In this particular application of MFL technique, wire ropes are locally magnetised using electromagnets or permanent magnets. If any defect is present in the rope, some amount of flux lines leak out of the surface around the defect. This leakage flux is measured using magnetic field sensors and is correlated to the size and location of the defects. A variety of procedures that use different types of sensors and magnetising devices have been reported for reliable detection of defects in wire ropes [22-23, 137-138]. Wang *et al.* [30] used flux gate sensors for detection of broken wires in a coal mine-hoist cable and a back propagation neural network for assessment of the position and number of broken wires in the cable. Jomdecha *et al.* [137] used printed circuit-shaped coils connected in series as field sensors placed in a solenoid coil magnetisation and reported the detection of 2 mm deep surface defects in a 38 mm diameter wire rope. Kalwa *et al.* [23, 138] developed MFL systems with magnetic concentrators and Hall and coil sensors for enhancing the detection sensitivity of defects in steel ropes. They suggested that measurement of the axial component is more versatile than the radial component for the detection of multiple defects in wire ropes.

One example of solid cylindrical geometry is track rope. Track ropes are a type of wire ropes used for transportation of coal in mining industries. One such rope system is operated for about 10 hours every day in Heavy Water Plant (HWP), Manuguru, to transport 3000 tons of coal with the help of 256 numbers of buckets, each carrying nearly 1.6 tons of coal. The track rope is stationary and is rigidly supported by towers at periodic intervals. The schematic of the cross-section of the track rope along with the design details is shown in Figure 5.1. The track rope has eight layers of stranded wires of different diameters. The six inner layers are round-type wires, while the outer two layers are Z-type wires. The round wires are locked by two Z wires to get the strength of the rope. The width of the outer surface of the first Z wire is 6.45 mm, and the gap width between two outer Z wires is 0.76 mm. During the operation of the rope system, the carriage wheels of the bucket come in contact with the top surface of the outer Z wire as shown in Figure 5.2(a). Prolonged use of the rope system is expected to cause abrasion and wear, resulting in LMA or LF type defects (Figure 5.2b). Also wire breakage and formation of fatigue cracks, pitting corrosion, inter strand nicking or martensitic embrittlement, etc. are likely to occur [21]. When more than two Z wires of the outer layer are broken, they will be separated from the adjacent layers, as shown in Figure 5.3. Therefore, detection of damage in track rope is essential to ensure the safety and also to plan the replacement or repair of the track rope, as part of the condition monitoring and life management programme.

This chapter discusses the model based optimization of MFL technique that uses saddle coils and flexible GMR array sensor proposed, for the first time, for inspection of artificial LFs and LMA defects in the 64 mm diameter steel track ropes.

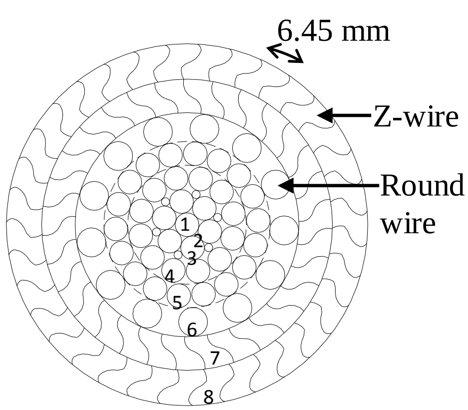

Layer	**Wire details**	**Wire dia. or thickness, mm**
1	1 centre wire	4.00
2	6 round wires	4.66
3	6 filler wires	1.93
4	12 round wires	4.33
5	18 round wires	4.27
6	13 round wires	4.95
7	32 Z-wires	5.50
8	34 Z-wires	6.48

Figure 5.1 The cross-section and design details of double locked track rope.

(a) (b)

Figure 5.2 (a) Photograph of the track rope system with bucket carrying coal and (b) local flaws and loss of metallic cross-sectional area on the outer surface of the track rope.

Figure 5.3 Breakage of wires at the outer surface of the track rope.

5.2 MFL Technique for Solid Cylindrical Geometry

An MFL technique that uses split-type saddle coils and flexible sensor arrays has been proposed, for the first time, for the inspection of track ropes of solid cylindrical geometry. Two saddle coils are used for uniform axial magnetisation of the rope. The current in the saddle coils is set in opposite direction to enable predominantly axial magnetisation of the rope region between the coils. A flexible GMR array sensor is used to measure the axial (B_a) component of leakage magnetic flux by scanning the sensor array and the magnetisation coils together as a single unit over the track rope. In order to enhance the sensitivity, each GMR sensor output is amplified, digitized and stored in the computer for subsequent analysis.

5.3 Modeling

Three different structures of coil based magnetising unit viz. solenoid, Helmholtz and saddle coils are possible for magnetisation of the track rope as shown in Figure 5.4. Among the structures, traditional solenoid (Figure 5.4a) and Helmholtz coil (Figure 5.4b) based magnetising units are not suited for practical field inspection as the movement of the coil is obstructed by the supporting towers. On the contrary, split-type saddle coils are convenient to move freely over the supporting towers. Moreover, most of damages occur only on the top surface of the rope which can be easily covered by the saddle coils. So, saddle coils (Figure 5.4c) based magnetisation unit has been chosen for inspection of 64 mm diameter steel track ropes.

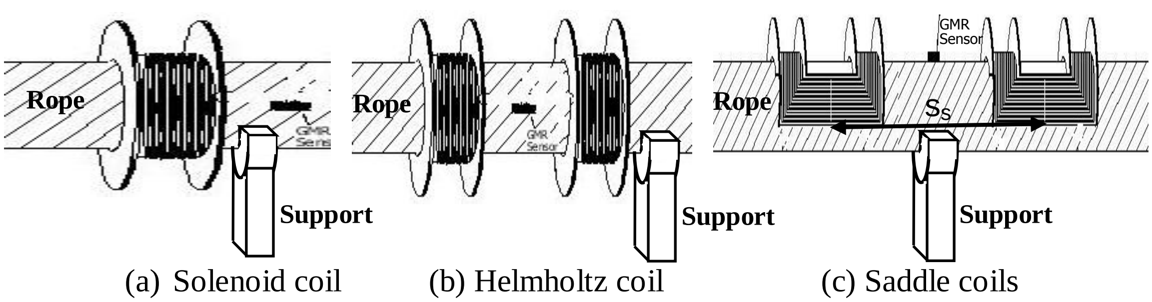

Figure 5.4 Three different structures of coil based magnetising unit for MFL NDE of track ropes.

5.3.1 Optimization of Magnetizing Current

3D-FE modeling has been performed to optimize the magnetising current flowing in the two saddle coils and to predict the leakage magnetic fields from LFs and LMA type defects in the track rope. Figure 5.5(a) shows the mesh generated for the geometry which consists of a track rope (length 300 mm, outer diameter 64 mm) and two saddle coils (length 120 mm, width 35 mm) each consisting of 90 turns with a cross sectional area of 20 x10 mm^2. Equation (5.1) has been solved in three dimensions using the finite element method.

$$\nabla \times \left(\frac{1}{\mu_0 \mu_r} \nabla \times A\right) = J \tag{5.1}$$

where *A* is the magnetic vector potential, μ_0 is the magnetic permeability of free space, μ_r is the relative permeability of steel and *J* is the current density.

For simplicity, in the model the track rope is assumed as a solid rod and GMR sensor as well as velocity effects are not modeled. The magnetising current in the saddle coils is taken as 5 A. Magnetic insulation (n×A=0) boundary condition is applied at the outer boundaries of the model. The iterative solver is used for solving equation (5.1). The computation time with 5673392 degrees of freedom is approximately 50 minutes for a dual-core 64 bit processor workstation with 8 GB primary memory.

The magnetic vector potential A is computed in the solution region and the axial component of the magnetic flux density between the two saddle coils is predicted. Figures 5.5(b) and 5.5(c) are the model predicted magnetic flux line contours for same and opposite directions of electric currents respectively. In the case of same direction of magnetising current, the magnetic flux lines are predominantly along the radial direction of the rope (Figure 5.5b). On the contrary, the magnetic flux lines are fairly uniform along axial direction of the rope for opposite direction of magnetising current (Figure 5.5c). This is attributed to the same direction of electric current in the nearest semicircular coils similar to the current direction in the Helmholtz coil. Hence, the magnetising current in the saddle coils is set in opposite directions to ensure axial magnetisation of the rope region between the saddle coils.

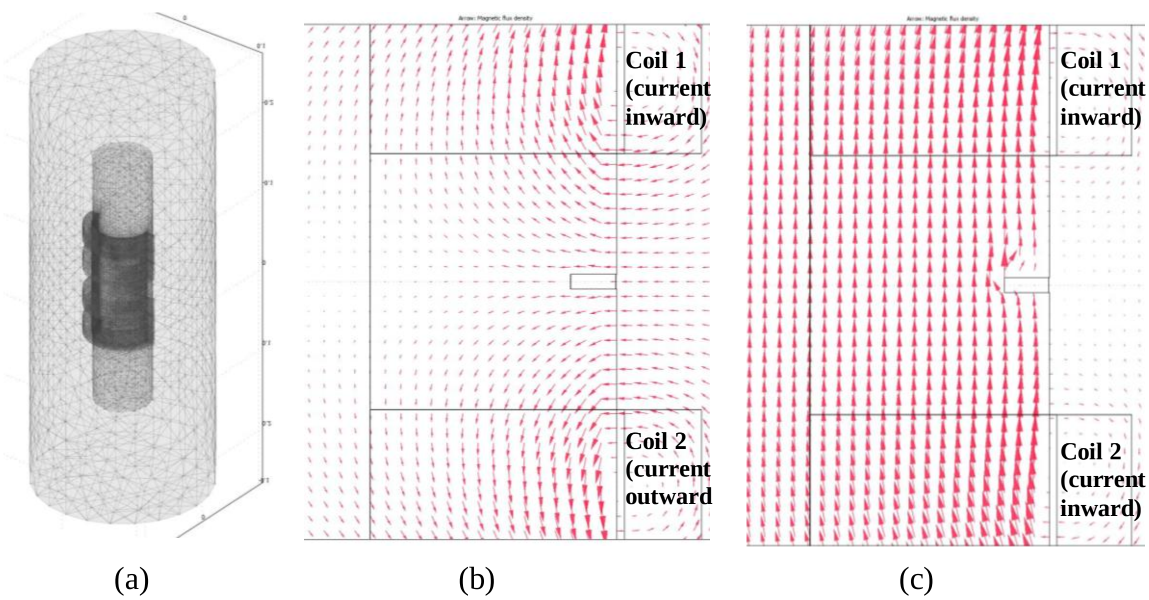

Figure 5.5 (a) 3D finite element mesh and model predicted magnetic flux line contours between the two saddle coils for (b) same and (c) opposite directions of electric currents.

The magnitude of magnetising current of the saddle coils is optimized for obtaining sufficient detectable leakage field signals from all the flaws considered. The current is optimized using the B_a^{peak} amplitudes of the MFL signals. The model predicted B_a^{peak} amplitudes of the shallowest axial notch (2.05 mm deep) and circumferential notch (1.94 mm deep) for different magnetising currents are shown in Figure 5.6(a). As can be seen, B_a^{peak} increases with the increase in magnetizing current for both notches due to higher magnetomotive force. However, there is likelihood of saturation of GMR sensor at currents greater than 5 A. Hence, a current of 5 A has been chosen as the optimum current for this technique.

5.3.1 Optimization of Inter-coil Spacing

The inter-coil spacing (s_s) between the two saddle coils is optimized for obtaining uniform axial magnetisation of the rope region between the two coils so that sufficient detectable magnetic fields were leaked out of the notches. It is optimized using B_a^{peak} amplitudes of the MFL signals for the notches. The typical B_a^{peak} amplitudes of the shallowest axial notch (2.05 mm deep) and circumferential notch (1.94 mm deep) for various coil spacing of 60 mm to 85 mm in steps of 5 mm are shown in Figure 5.6(b). The B_a^{peak} amplitudes of the MFL signals for both axial and circumferential notches are found to increase upto 75 mm spacing. At distances greater than 75 mm, the signal amplitudes are seen decreased due to reduction in magnetic field strength with the increase in inter-coil spacing of coils. Hence, a distance of 75 mm has been chosen as the optimum inter-coil spacing between the two saddle coils.

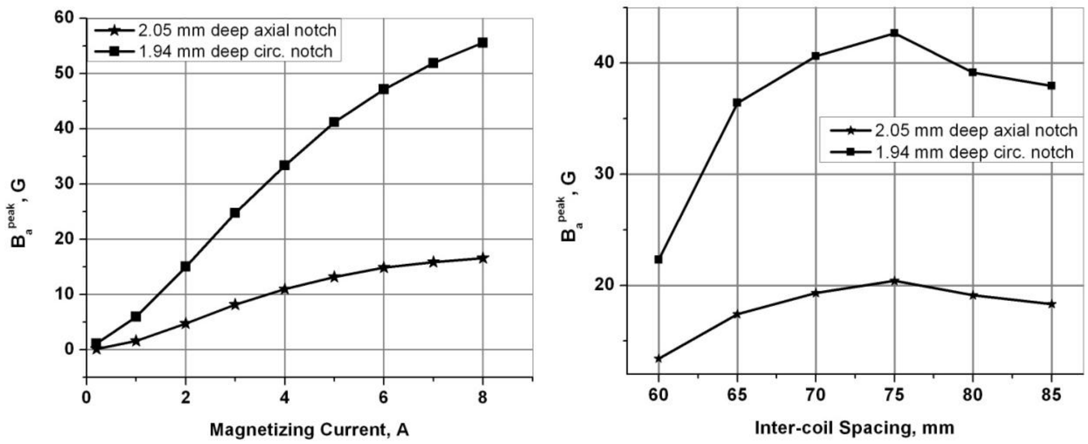

(a) (b)

Figure 5.6 Optimization of (a) magnetising current and (c) inter-coil spacing between the two saddle coils.

5.4 Experimental Setup

The experimental setup used for the MFL measurements on a track rope is shown in Figure 5.7. It consists of two saddle coils, variable DC power supply, track rope, GMR sensor, GMR field meter and a personal computer. Each saddle coil consists of 90 turns with a cross sectional area of 20x10 mm^2. The two saddle coils are separated by a gap of 75 mm. The current in the coils is set in opposite direction to enable predominantly axial magnetisation of the rope in the region between the coils. GMR bridge sensor (AA003-02) is kept at the middle of the saddle coils.

Measurements are made by moving the GMR sensor and saddle coils together as a single unit over the track rope in steps of 0.5 mm. A constant lift off of 0.3 mm is maintained between the GMR sensor and the track rope to avoid physical damage to the sensor. In order to enhance the sensitivity of GMR sensor, its output is amplified using a low-noise amplifier consisting of a differential amplifier, notch rejection filter at 50

Hz, 100 kHz low-pass filter and a single-ended variable gain amplifier. The variable gain amplifier is set such that it amplifies the sensor output by a factor of 10. The amplified GMR sensor output is digitized using a 2-channel data acquisition system (16 bit) and stored in the computer for further analysis.

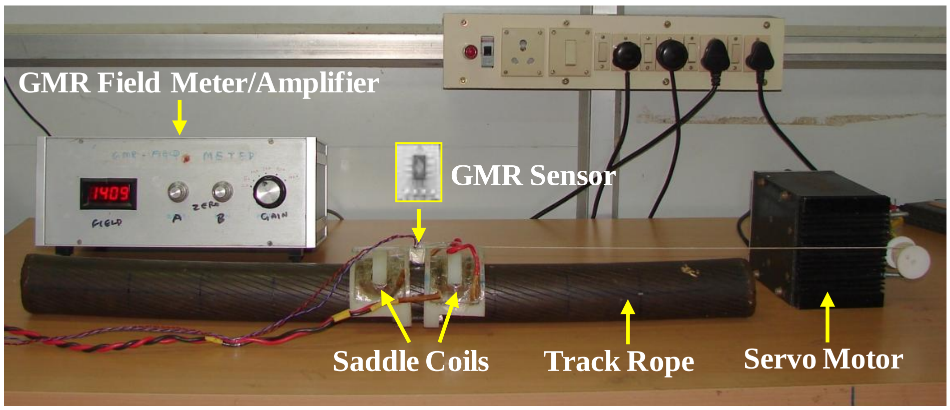

Figure 5.7 Experimental setup for the MFL testing of track ropes.

5.5 Reference Defects

LFs are simulated by EDM notches introduced on the outer surface of the track rope. Four axial notches (A, B, C, D) and four circumferential notches (E, F, G, H) of 5.5 mm length, 2.0 mm width and of different depths are machined. A schematic of the type and location of the notches is shown in Figure 5.8. The distance between the notches is maintained at 80 mm, which is slightly more than the length of magnetisation unit (75 mm) to avoid the mutual interaction of leakage fields from notches. The depths of the EDM notches measured using the replica technique are given in Table 5.1. One LMA-type defect (length 42.0 mm, width 9.2 mm, depth 3.0 mm) is simulated by removing the material from the outer surface of the Z-wire, and this depth is around 46.3% of the Z-wire diameter.

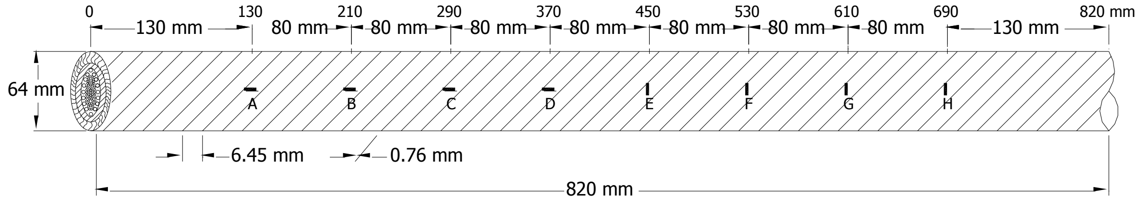

Figure 5.8 Schematic of the track rope having axial and circumferential machined artificial notches.

Table 5.1 Details of artificial EDM notches machined in the track rope (length 5.5 mm and width 2.0 mm)

Notch	**Notch Orientation**	**Notch Depth, mm**
A	Axial	2.05
B	Axial	4.11
C	Axial	5.86
D	Axial	7.91
E	Circumferential	1.94
F	Circumferential	3.88
G	Circumferential	5.90
H	Circumferential	8.24

5.6 Experimental Results

5.6.1 Local Flaws

The MFL signals of axial notches viz. A, B, C and D in the track rope are shown in Figure 5.9(a). The signal amplitude of the shallowest axial notch, A (2.05 mm deep) is approximately 4.9 times the background noise from the stranded structure of the track rope. The SNR for notch A is better than 14 dB. As can be observed, all the four axial notches are detected by the technique with two distinct peaks correlated to the edges of axial notches. Double peaks are seen in the signals of the axial notches due to the extended nature of the axial notches.

The MFL signals of circumferential notches viz. E, F, G and H in the track rope are shown in Figure 5.9(b). Once again, all four circumferential notches have been clearly detected. The signal amplitude of the shallowest 1.94 mm-deep circumferential notch, E is 7.5 times the background noise. The MFL signals of the circumferential notches in Figure 5.9(b) are seen sharp with a single peak, which is in contrast to that observed for the axial notches in Figure 5.9(a).

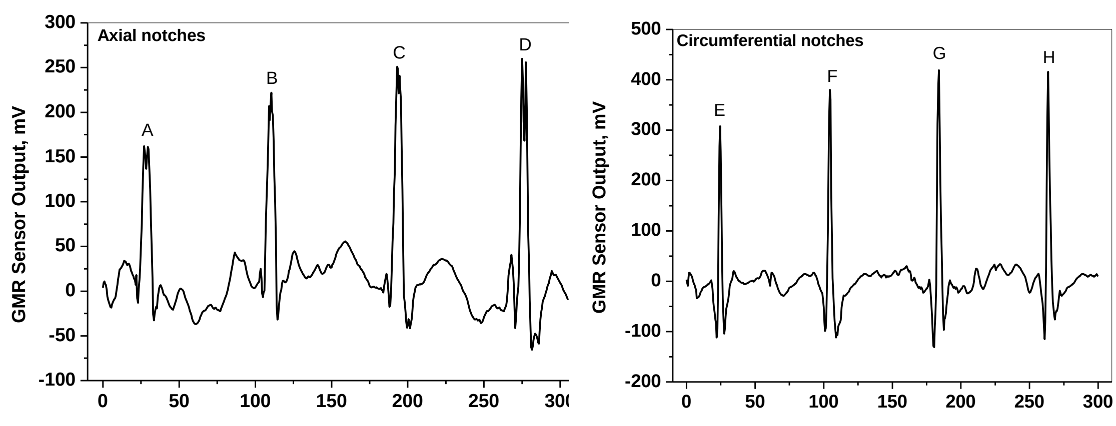

(a) (b)

Figure 5.9 MFL signals for (a) axial notches and (b) circumferential notches.

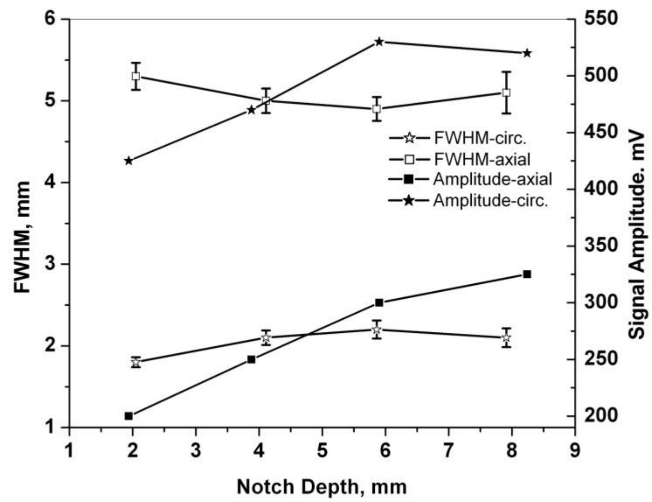

Figure 5.10 FWHM and signal amplitude for axial and circumferential notches.

In order to evaluate the detection and sizing capability of the technique, the peak amplitude and FWHM are determined for all the signals and the results are shown in Figure 5.10. The FWHM is determined after the Gaussian fitting of the data. The error in the determination of FWHM is ±0.1. In the case of the axial notches, the amplitude of the MFL signals is found to increase with notch depth and the FWHM is found to be nearly constant. In the case of the circumferential notches, the amplitude increases upto the 5.90 mm deep notch and then decreases, while the FWHM remains nearly constant. The decrease in the signal amplitude of notches deeper than outer diameter, i.e. 6.48 mm, is due to the penetration of a significant amount of magnetic flux into the inner layers of the rope and not reaching the GMR sensor to be detected. The signal amplitude is expected to be higher for a larger thickness of Z-wire and smaller diameter of the rope. It is also observed that the amplitude of the circumferential notches is nearly two times higher than that of the axial notches of similar depth. However, the FWHM of circumferential notches is found to be nearly two times lower than that of the axial notches. This is essentially due to the axial magnetisation of the track rope, resulting in higher leakage flux by the circumferential notches.

The performance of the MFL technique has been assessed for the detection of a fine circumferential saw cut (length 15 mm, width 0.5 mm, depth 2 mm), which simulates somewhat close to a tight surface fatigue crack. The MFL signal for the saw cut is shown in Figure 5.11. As can be observed, the technique could readily detect the tight saw cut with a very good SNR. The signal shape nearly matches with the signal shape of the circumferential notches (width 2 mm) of Figure 5.9(b). The signal amplitude is found to be less than that of circumferential notch E of similar depth due to the smaller width of the former.

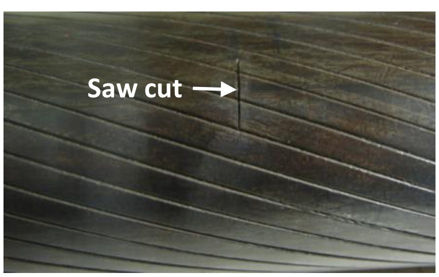

(a) (b)

Figure 5.11 (a) Photograph of the saw cut in the track rope and (b) the corresponding GMR sensor output.

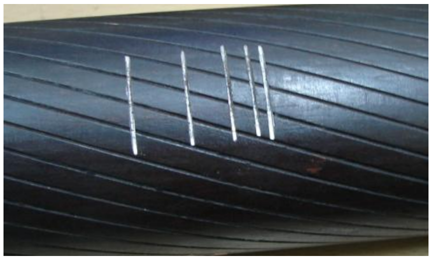

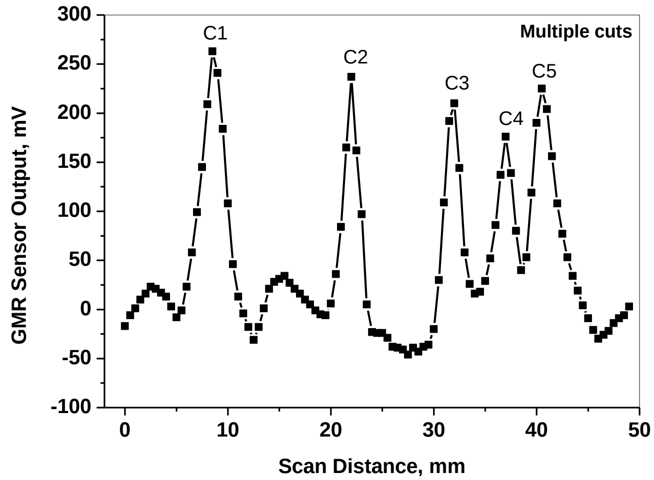

(a) (b)

Figure 5.12 (a) Photograph of 5 saw cuts separated by 13.5 mm, 10.0 mm, 5.5 and 3.2 mm distances and (b) the corresponding GMR sensor measured MFL signals.

Further, the resolution of the MFL technique has been evaluated by studying the signals of five saw cuts (C1, C2, C3, C4 and C5), each of length 23.2 mm, width 1.0 mm and depth 2.0 mm, separated by finite distances as shown in Figure 5.12(a). The MFL signals of the saw cuts are shown in Figure 5.12(b). It is found that the proposed technique is able to detect all the 5 saw cuts. The intensity of the leakage field is found to decrease with the decrease in separation between the saw cuts due to the effect of mutual interaction. The MFL technique is able to clearly distinguish the saw cuts separated by a gap of 3.2 mm. It may be noted here that a large variation in scanning speed and lift-off during testing may change the signal amplitude and hence the resolution of the technique.

5.6.2. Loss of Metallic Cross-sectional Area

The MFL signal of the simulated LMA (length 42.0 mm, width 9.2 mm and depth 3.0 mm) for scanning along the *AA* direction is shown in Figure 5.13. As can be observed, the technique is able to detect unambiguously the LMA in the track rope with good SNR. Following the dimension of the LMA, the MFL signal of LMA is found to be extended compared to the sharp signal of the LF. The signal amplitude of LMA is found to be 468.7 mV, which lies between the signal amplitude of circumferential and axial LFs. The FWHM of LMA is found to be 29.1 mV, which is unambiguously more than the FWHM of circumferential notches (~2.0 mm) and axial notches (~5.0 mm).

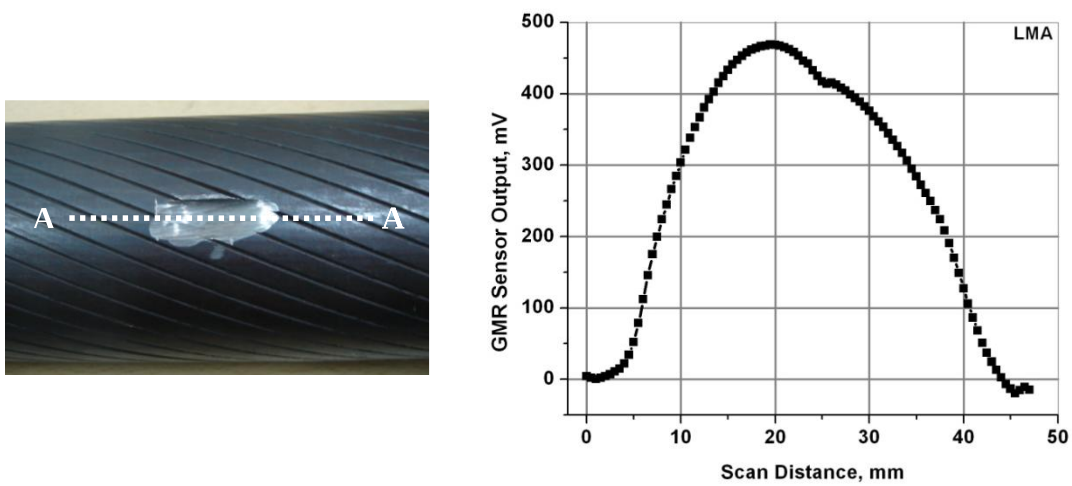

Figure 5.13 Photograph of LMA (42.0 mm length, 9.2 mm width and 3.0 mm depth) machined in the track rope and its GMR sensor response scanned along dotted line *AA* direction.

The proposed MFL technique can be used for condition monitoring of the track rope as it enables reliable detection of LF and LMA type flaws on the outer layer of the track rope. The high resolution of the technique is expected to enable effective detection of degradation on the track rope during periodic inspection and can help in prevention of premature retirement of track rope, through implementation of timely corrective actions.

5.6.3 Validation

The MFL signals of LFs and LMA type defects have been predicted using the model. Figure 5.14(a) shows the model predicted normalised MFL signals of the axial notch, C and the circumferential notch, G (5.5 mm length and 2 mm width) of similar depth. The MFL signals are normalised to the signal peak amplitude of the circumferential notch, G. It is found that the signal amplitude of the notch G is found to be 2 times higher than the notch C. However, FWHM of notch G is found to be 2 times lower than the notch C, essentially due to the axial magnetisation of the track rope. Figure 5.14(b) shows the MFL signals of notches C and G measured experimentally using a GMR sensor.

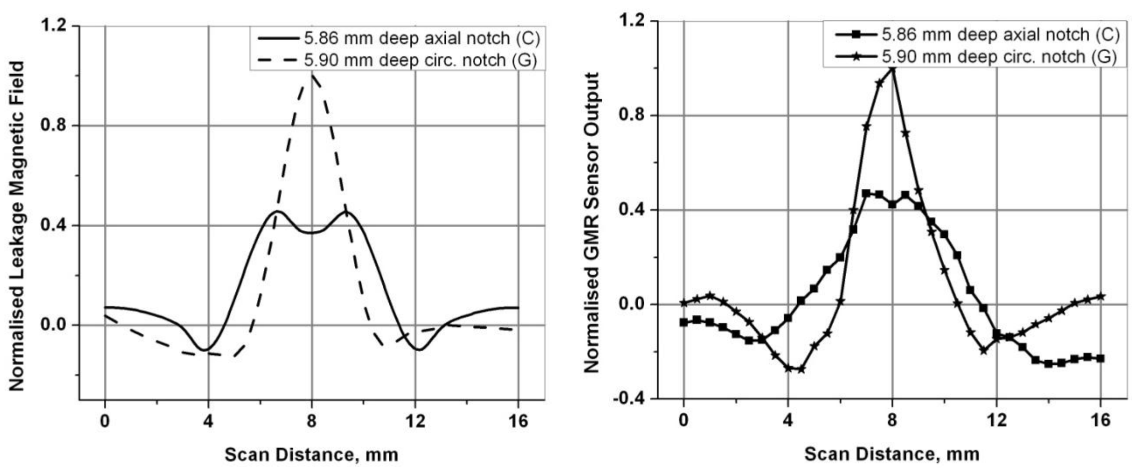

(a) (b)

Figure 5.14 (a) Model predicted MFL signals from the axial notch, C and the circumferential notch, G and (b) the corresponding experimentally measured GMR sensor response.

The model predicted signal amplitude of the circumferential LFs is compared with the experimentally obtained GMR signal amplitude in Figure 5.15(a). As can be seen, there is an increase in signal amplitude in both the cases, except for the experimental signal amplitude of the 8.24 mm deep notch. This attribute may be due to the fact that some of the magnetic field lines are leaked into the second Z layer. It must be noted that the rope is assumed as a single solid cylinder in the modeling, ignoring the noise arising from the anisotropy of 0.76 mm wide helical Z layer strands which will be studied in future.

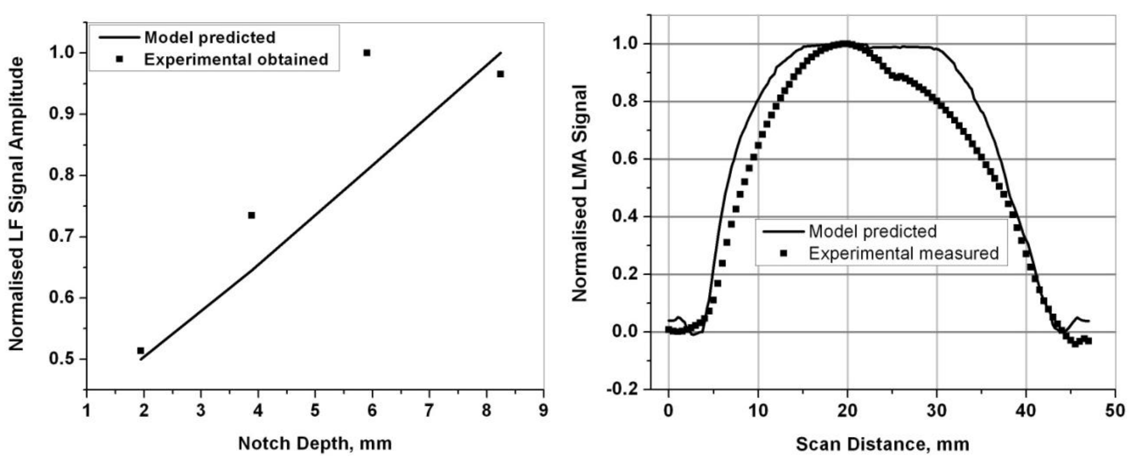

(a) (b)

Figure 5.15 Comparison of model predicted and experimentally measured (a) normalised MFL signal amplitude of circumferential LFs and (b) MFL signal of LMA.

The model predicted normalised leakage field profile of LMA is compared with the experimentally measured GMR output as shown along in Figure 5.15(b) and a good agreement has been observed.

5.6.4 Comparative Performance of Saddle Coils and Helmholtz Coil magnetisations

MFL signals of axial notches viz. A, B, C and D, obtained using Helmholtz coil magnetisation (Figure 5.16) are shown in Figure 5.17(a). The GMR sensor output for the shallowest axial notch, A (2.05 mm deep) is approximately 2.0 times the background noise that comes mainly from 0.76 mm wide stranded structure of the track rope. Similar to saddle coils magnetization (Figure 5.9a), all the four axial notches are detected by the technique with two distinct peaks correlated to the edges of axial notches. The signal amplitude in Helmholtz coil magnetisation is found to be ~ 4 times higher than that of saddle coils magnetisation. It is due to larger uniform axial magnetisation of the rope by the Helmholtz coil as compared to saddle coil magnetisation and hence more leakage flux occurs from the notches. However, the SNR of the shallowest axial notch, A (2.05 mm deep) for saddle coil (SNR=14 dB) is found to be ~ 2 times higher than that of Helmholtz coil (SNR=6 dB). This is attributed to the higher noise in the Helmholtz coil (only axial field) which arises due to stranded structure of the rope as compared to saddle coil (both axial and radial fields). In the case of Helmholtz coil magnetisation, both signal amplitude due to notch and noise amplitude due to stranded structure in the rope are found to be higher. In the case of saddle coil magnetisation, signal amplitude is found to decrease and the noise amplitude is also found to decrease significantly.

MFL signals of circumferential notches viz. E, F, G, and H, obtained using Helmholtz coil magnetisation are shown in Figure 5.17(b). Once again, all the four notches are detected and the GMR sensor response of circumferential notches is found to be sharp with a single peak as observed in the MFL signals using saddle coils magnetisation (Figure 5.9b). The signal amplitude of 1.94 mm deep notch, E is 3.2 times the background noise. The signal amplitude in Helmholtz coil magnetisation is ~ 5 times higher than that of saddle coils magnetisation. However, the SNR of the shallowest circumferential notch, E (1.94 mm deep) for saddle coil (SNR=18 dB) is found to be ~ 2 times higher as compared to that of Helmholtz coil (SNR=10 dB). Also, Helmholtz coil cannot be used for field inspection due to practical problems of supporting towers whereas saddle coils can be used. Moreover, most of damages occur only on the top surface of the rope which can be easily covered by the saddle coils. Thus, saddle coils is found to be better than Helmholtz coil for inspection of track ropes with half (top side) access.

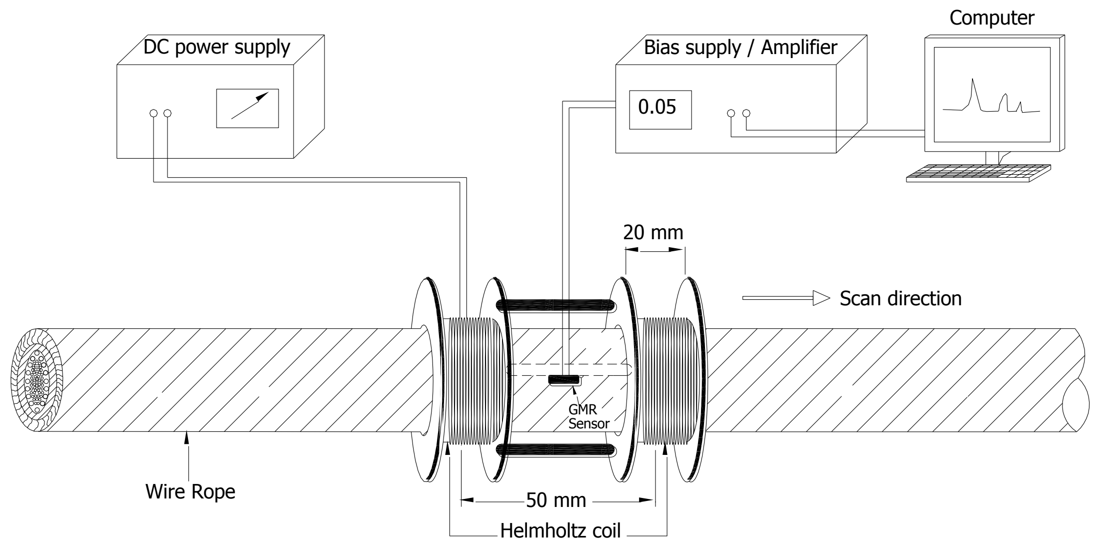

Figure 5.16 Schematic of Helmholtz coil magnetisation based MFL testing setup.

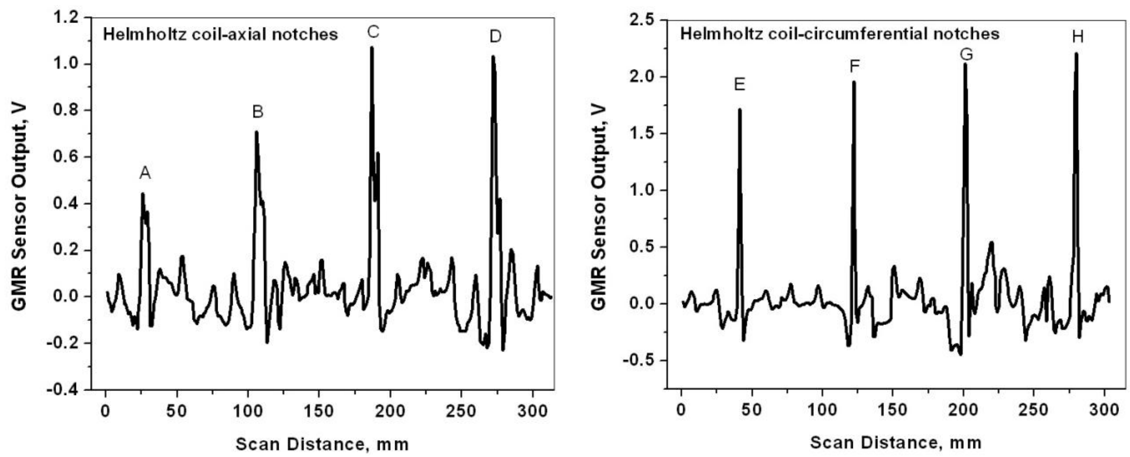

(a) (b)

Figure 5.17 MFL signals of (a) axial notches and (b) circumferential notches.

5.7 Development of Flexible 12 Element GMR Array Sensors

3D-FE modeling has been performed to optimize the number of GMR elements required to cover the top surface of the track rope and to determine the sensor locations. Figure 5.18(a) shows the model predicted axial component of the magnetic flux density between the two saddle coils. As can be seen, the magnetic flux density is fairly uniform for an optimum circumferential inter-coil distance of 80 mm that completely covers the expected damage region on the top surface of the Z-wire (dotted region in Figure 5.18a). This region can accommodate 12 GMR sensors. Hence, a flexible array of 12 GMR sensors has been designed, fabricated (Figure 5.18b) and used for detection of damage on the track rope.

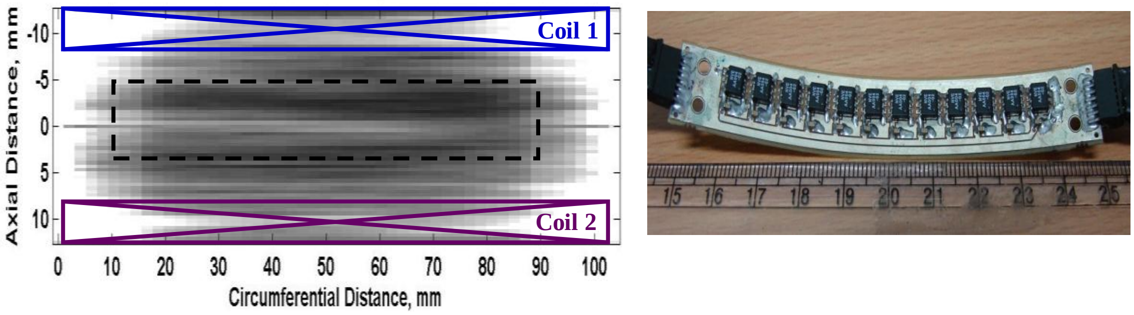

(a) (b)

Figure 5.18 (a) Model predicted magnetic flux density between the saddle coils along half of circumferential distance and (b) the fabricated flexible sensor array of 12 GMR sensors.

The performance of the flexible 12 element GMR array sensors has been evaluated by measuring the axial component of leakage fields from two LF and two LMA type defects in track rope. The two LFs are simulated by EDM notches of size 5.5 x 2.0 x 2.0 mm^3 (length x width x depth) oriented along axial and circumferential directions in the track rope, as shown in photographs 5.19(a) and 5.19(b). The two LMAs of sizes 42.0 x 9.0 x 3.0 mm^3 and 33.5 x 14.2 x 4.9 mm^3 are made along axial and circumferential directions respectively (refer Figures 5.19c and 5.19d).

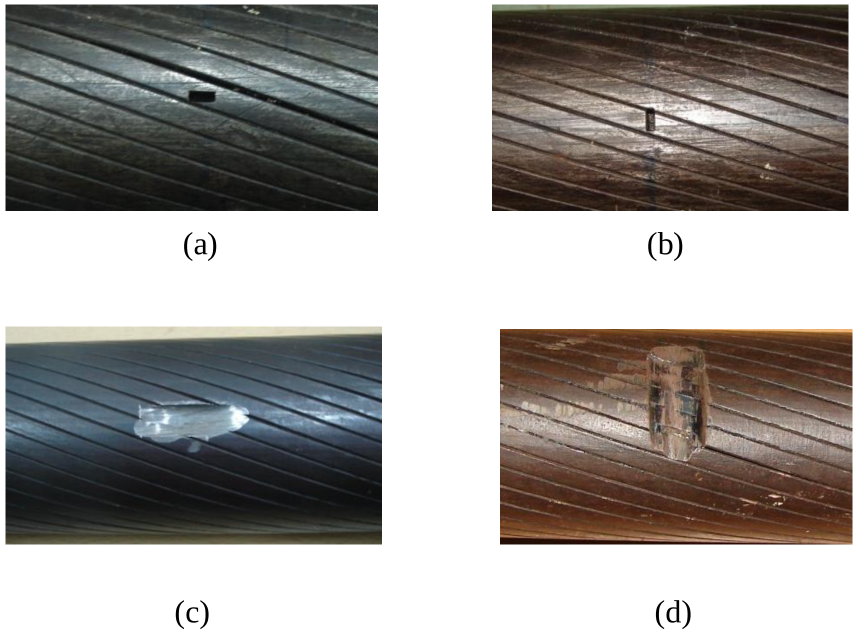

Figure 5.19 Photographs of (a) axial LF, (b) circumferential LF, (c) axial LMA and (d) circumferential LMA type defects in the track rope.

The MFL signals of the sensor array for the circumferential LF in the track rope are shown in Figure 5.20. As the length of the flaw is 5.5 mm, only two GMR sensors viz. S6 and S7 have shown the output of the leakage flux.

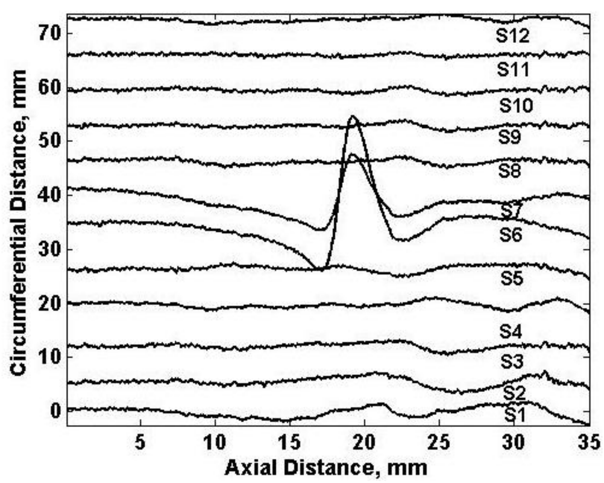

Figure 5.20 GMR sensor array response for a 5.5 mm long circumferential LF.

The GMR array sensor output has been processed for removing background noise and formatted to obtain images. The MFL images of axial and circumferential LFs shown in Figure 5.19 are shown in Figures 5.21(a) and 5.21(b) respectively. As compared to the MFL signals, it is possible to readily discern the spatial extent of the flaws from the MFL images produced by the sensor array. The MFL image of the axial LF is found to be extended as compared to that of the circumferential LF.

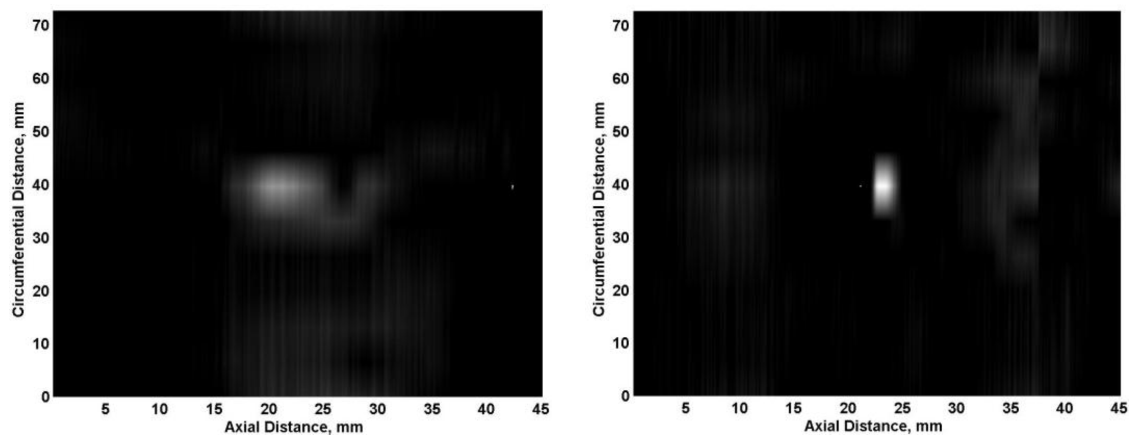

(a) (b)

Figure 5.21 MFL images for (a) axial and (b) circumferential LFs.

The MFL images of axial and circumferential LMAs are shown in Figures 5.22(a) and 5.22(b) respectively. As can be noted, the spatial extents of the LMAs could be readily felt from the images, despite some random noise. In the case of circumferential LMA, the output of three sensors viz. S5, S6 and S7 that are exactly over the LMA defect have been found saturated due to high leakage field.

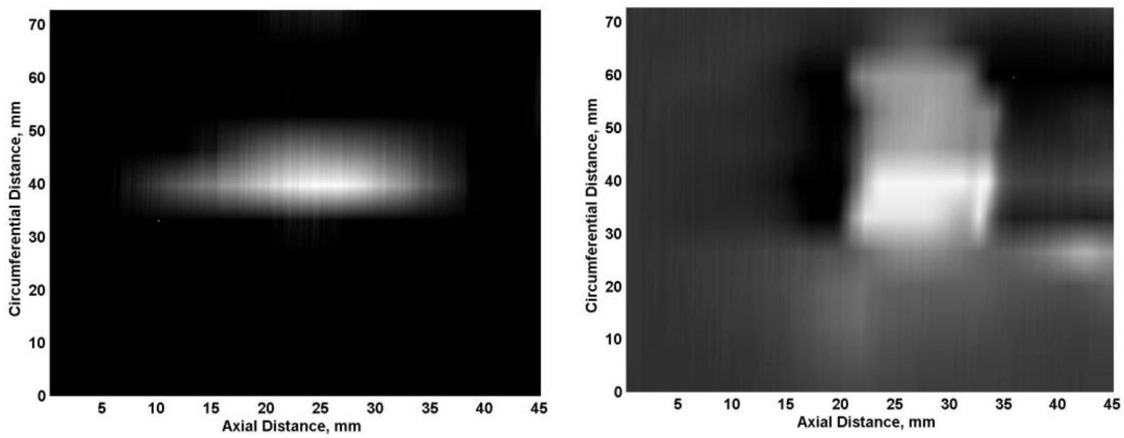

(a) (b)

Figure 5.22 MFL images of (a) axial LMA (42.0 x 9.0 x 3.0 mm^3) and (b) circumferential LMA (33.5 x 14.2 x 4.9 mm^3).

The flexible GMR sensor array has shown detection capability for both LF and LMA type defects oriented along the axial as well as circumferential directions. The sensor array has a fast detection speed along the length of the track rope and does not require circumferential scanning. The images of circumferential notches have been found to be sharp.

5.8 Conclusions

- ✓ This chapter proposes, first of its kind, saddle coils-GMR based MFL technique for condition monitoring of LF and LMA types of defects on the outer surface of 64 mm diameter steel track ropes.
- ✓ The optimized technique is able to detect both LF and LMA type defects in track ropes.

- ✓ 2.0 mm deep axial and circumferential notches (length, 5.5 mm, width, 2.0 mm) in the track rope are detected with SNR better than 14 dB.
- ✓ The technique is able to resolve flaws separated by a distance of more than 3.2 mm.
- ✓ Using the amplitude and FWHM of the MFL signals, it is possible to classify whether the flaw in the track rope is axial or circumferential.
- ✓ The model predicted characteristics of MFL signals for LF and LMA defects have been experimentally validated.
- ✓ A flexible 12 element GMR array sensor has been developed and used for fast detection and imaging of both types of defects in the track rope.
- ✓ The use of saddle coils-GMR array sensor based MFL technique is expected to result in reliable periodic condition monitoring of the track rope, enhance safety and incorporation of corrective measures that enable extension of life of the track ropes.

Chapter 6: Optimization of MFL Technique for Hollow Cylindrical Geometry

6.1 Introduction

MFL technique is widely used for inspection of hollow cylindrical geometry components such as oil and gas transmission pipelines [15-16] and tubes [24-25]. About 80% of pipeline inspection is carried out using Pipe Inspection Gauge (PIG). A detailed report has been submitted by Nestleroth *et al.* [15] for inspection of pipelines. MFL technique can reliably detect metal loss due to corrosion and, sometimes, gouging occurred in gas-pipelines. Apart from pipelines, small diameter ferromagnetic tubes are abundant in critical applications. Some examples are steam generator (SG) tubes in nuclear power plants and heat exchanger tubes in boiler and petrochemical industries. The inspection of these tubes is extremely important to prevent catastrophic failures and to extend their life. This chapter discusses the developmental study of MFL technique for inspection of SG tubes of Prototype Fast Breeder Reactor (PFBR) of 500 MWe being commissioned at Kalpakkam, India.

Steam generator is one of most critical components in sodium cooled PFBR. The main function of SG is to extract the reactor heat through secondary circuit and convert feed water into superheated steam in the tubes of SG. SG is a shell and tube, once through vertical (height 25 m) heat exchanger (Figure 6.1a) with sodium on the shell side and water on the tube side [139]. Any leakage in the sodium-water interface would lead to catastrophic failure by violent sodium-water exothermic reaction which makes the SG a critical component in determining the efficient running of the plant. Therefore, periodic ISI of SG tubes is essential to identify tube degradation at its incipient stage and take remedial action to ensure safe and reliable operation of the plant.

The structural material of SG tubes of PFBR is modified 9Cr-1Mo (Grade 91) steel which is ferromagnetic. This material has been chosen in view of its excellent high temperature creep and fatigue resistant properties and high thermal conductivity [140]. There are 547 tubes of outer diameter 17.2 mm and wall thickness (WT) 2.3 mm. Each tube has an expansion bend of radius 375 mm to accommodate differential thermal expansion. These tubes in the SG are stored as a bundle (Figure 6.1b) and generally clamped outside the tube by Inconel-718 which is non-magnetic. Therefore, ISI of these tubes is possible only from the inside of tube with limited accessible space. It should also be noted that most of the degradation in ferromagnetic SG tubes takes place on the outer surface of the tube, where they are more difficult to detect [141].

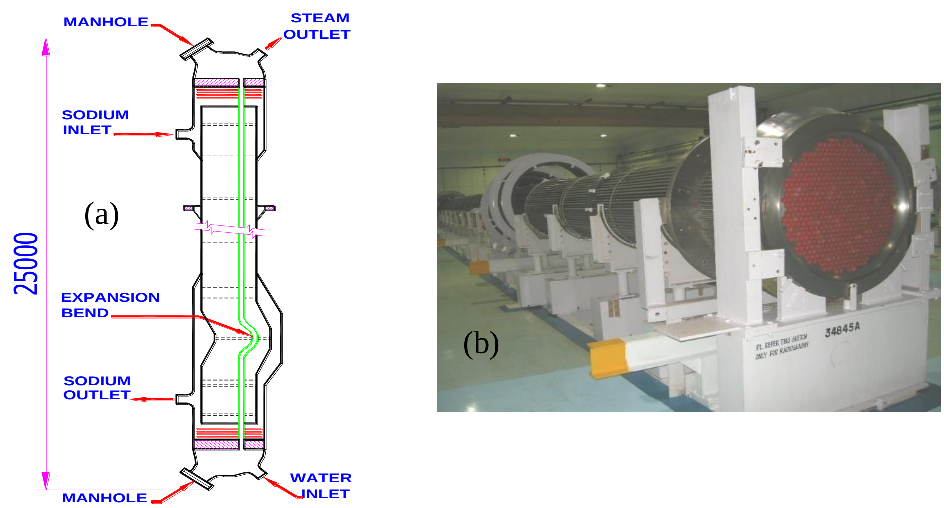

Figure 6.1 (a) Schematic of steam generator and (b) photograph of tube bundle assembly.

Several NDE techniques such as remote field eddy current (RFEC), partial saturation eddy current (PSEC), MFL, internal rotary ultrasonic inspection (IRIS), etc. are used for inspection of ferromagnetic heat exchanger tubes [2, 142-143]. The working principles, advantages and limitations of these techniques were reported in [2, 142]. Among these techniques, RFEC technique is widely used for ISI of ferromagnetic tubes due to equal sensitivity to both internal diameter (ID) and outer diameter (OD) defects and does not require large space for placing the RFEC probes [143-144]. RFEC technique is currently used for detection of defects in SG tubes of PFBR [116, 145]. Thirunavukkarasu *et al.* [116] showed detection of wall thinning of 10% WT, through hole of 2 mm diameter and circumferential notch of 1.15 mm depth (50% WT) using RFEC technique. This technique is capable of detecting uniform wall thinning and large volumetric defects. However, it has shown that the RFEC technique has poor sensitivity for the detection of localized cracks and shallow volumetric defects which are expected to occur during service. Moreover, RFEC signals are influenced by the presence of support structures and sodium deposits (non-magnetic and highly conducting) in the defective regions of the tube which affects the sizing capability of the technique [145]. Therefore, a complimentary NDE technique to RFEC is essential for getting additional information during ISI of SG tubes. Among the potential NDE techniques, MFL technique is best suited for this purpose as it can detect both shallow surface and deep sub-surface defects in ferromagnetic materials.

M. J. Bergander [146] reported MFL testing of ferromagnetic heat exchanger tubes using permanent magnet for magnetisation and pair of induction coils for measurement of localized defects and gradual wall thinning in the tubes. Gotoh *et al.* [147-148] proposed alternating MFL technique for inspection of outer side defects on SUS 430 steel tube (OD 25 mm and WT 1.5 mm). They used an inner coil of low frequency of about 60 Hz for excitation and a search coil for detection of defects and showed detection of 0.5 mm (33% WT) deep circumferential defects. Krzywosz *et al.* [149] used induction coils and Hall sensors to measure the leakage magnetic fields from outer side erosion and holes in 19.05 mm OD carbon steel tube. They reported that MFL testing is limited to a tubing size where ID is at least six times the nominal wall thickness due to the physical constraints of the magnet size. Any inspection of tubes exceeding the above criteria will result in reduced sensitivity, especially to OD flaws. However, the ID (12.6 mm) of the SG tube in PFBR is about 5.5 times its wall thickness (2.3 mm) which exceeds the above criteria. This demands the use of high sensitive magnetic field sensors such as GMR sensors for detection of feeble magnetic fields especially from outer side defects. Moreover, detail on the optimization of MFL technique for small diameter tubes is scarce in the literature, although some details are reported for large diameter pipelines [112-115].

This chapter presents the optimization of GMR based MFL technique, proposed for detection of localized defects in small diameter (OD 17.2 mm) SG tubes of hollow cylindrical geometry. The performance of the technique has been evaluated by measuring the axial (B_a) component of leakage fields from localized outer side defects in the SG tube. The details of the model based optimization of MFL technique and the experimental measurement using GMR sensor are discussed.

6.2 MFL Technique for Hollow Cylindrical Geometry

The schematic of the MFL technique proposed for inspection of small diameter SG tubes of hollow cylindrical geometry is shown in Figure 6.2. It consists of two bobbin coils, a variable DC power supply, tandem GMR array sensors, differential amplifiers and a personal computer. The bobbin coils wound on a ferrite core is used for axial magnetisation of the tube. The bobbin coils has the advantages over the permanent magnet for allowing change in the magnetising current and also not adhering to the tube. The use of ferrite core concentrates the magnetic field lines along central axis of the tube and hence, reduces the compression of leakage fields due to direct magnetising fields. In addition, the two ends of the ferrite core are attached with ferrite rings which act as magnetic flux guiding device, by concentrating more magnetic field lines into the tube. This enhances the sensitivity of leakage field from the defects in the small diameter tube. The separation between the bobbin coils ensures predominantly uniform axial magnetisation of the tube region between the two coils. Two tandem GMR array sensors are kept at the middle of the bobbin coils with a phase shift as shown in Figure 6.2.

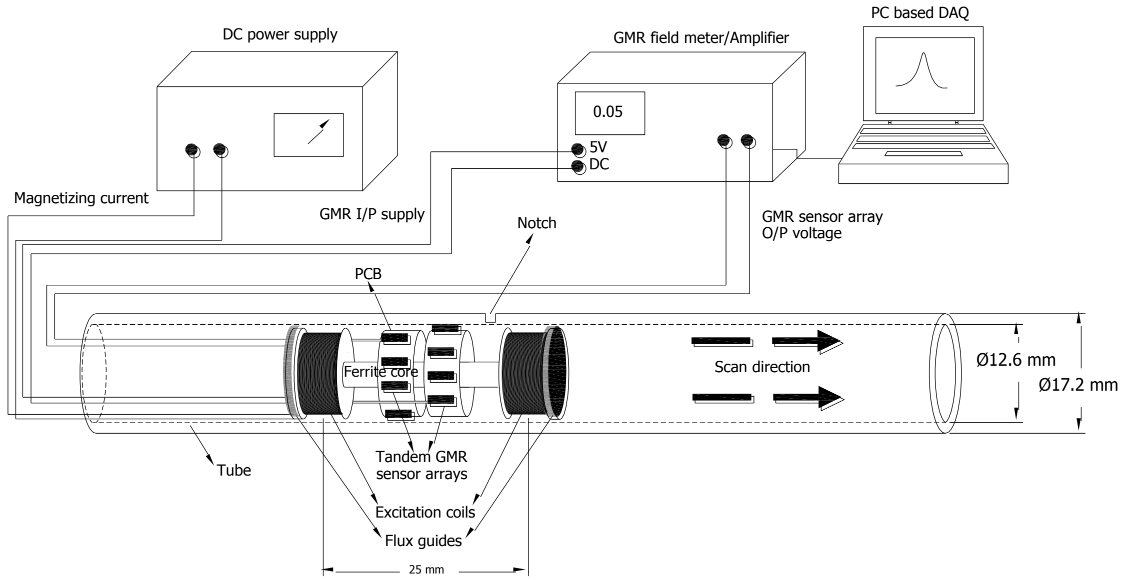

Figure 6.2 MFL technique proposed for small diameter SG tubes of hollow cylindrical geometry.

The axial component of the leakage flux from defects in the tube is measured using the GMR array sensors by moving the GMR array sensors and magnetisation coils together as a single unit inside the tube. In order to enhance the sensitivity of GMR sensors, its outputs are filtered and amplified. The amplified GMR sensor outputs are digitized and stored in the computer for subsequent analysis.

6.3 Modeling

2D-axis symmetry FE modeling has been performed to optimize the magnetising unit comprising of two bobbin coils used in the MFL technique for hollow cylindrical geometry i.e. SG tube. Firstly, the structure of the excitation coils has been optimized for enhanced detection of defects in the tube. Three different core structures (Figure 6.3) of bobbin coils are considered for magnetisation of the SG tube. Structure 1 (Figure

6.3a) is the air core bobbin coils. Structure 2 (Figure 6.3b) is the ferrite core coils. Structure 3 (Figure 6.3c) has extra flux guiding devices at the two ends of the ferrite core. In order to detect both the ID and OD defects, ID and OD defects of 50% WT (1.15 mm deep in 2.3 mm thick tube) have been considered for the optimization of the magnetisation coils. The B_a component of MFL signal at the sensor location has been predicted for all the three structures and compared their peak amplitudes (B_a^{peak}) for obtaining the optimal structure.

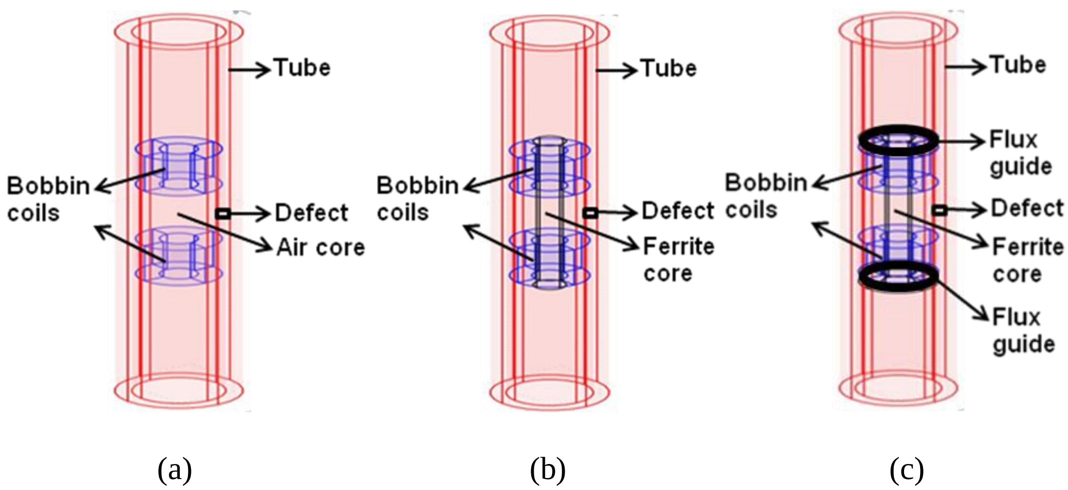

Figure 6.3 Three different core structures of bobbin coils based magnetising unit for MFL NDE of small diameter hollow cylinder.

The following equation (6.1) has been solved in two dimensions using the FE method:

$$\nabla \times \left(\frac{1}{\mu_0 \mu_r} \nabla \times A\right) = J \tag{6.1}$$

where A is the magnetic vector potential, μ_r is the relative permeability and J is the current density.

Table 6.1 gives the parameters used in the modeling of MFL technique for SG tubes of PFBR.

Table 6.1 Parameters used in the FE modeling of MFL technique.

Bobbin coils	No. of coils: 2 No. of turns of each coils: 70 Cross-sectional area: 10x3.4 mm^2 Current: 1.25 A Conductivity: 5.98×10^{7} S/m
Ferrite	Length: 40.2 mm, Diameter: 4.8 mm Relative permeability: 1000 Conductivity: 1.0×10^{-5} S/m
SG tube	Length: 100 mm, Outer diameter: 17.2 mm Wall thickness: 2.3 mm Relative permeability: B-H loop Conductivity: 4.03×10^{6} S/m
Defect (notch)	Dimensions: 1x1.15 mm^2
Boundary condition	Magnetic insulation ($n \times A=0$)
No. of mesh elements	105748
Size of mesh element at defect	0.00002 m
Degrees of freedom	211591
Solver	MUMPS (direct solver)
Computation time	24.43 s in dual core 64 bit processor workstation with 8 GB primary memory

The model predicted surface and normalised arrow plots of axial component of leakage field from the OD notch for three different core structures of bobbin coils are shown in Figures 6.4(a)-6.4(c). Among the three structures, ferrite core with flux guide (Figure 6.4c) has the highest value of B_a in the tube as the magnetic field lines generated by the two coils are drastically increased by the ferrite core together with the guiding of magnetic field lines into the tube. The significant increase of the flux density has also been seen in the surface plot (Figure 6.4c) of flux density of the ferrite with guide structure as compared to that of flux density of the ferrite core alone. This is attributed to the shorter magnetic path provided by the flux guide made up of ferrite. In the air core structure (Figure 6.4a), the leakage magnetic flux from the notch is masked by the direct magnetising field as the tube ID is very small (12.6 mm).

Figures 6.5(a) and 6.5(b) show the model predicted B_a component of MFL signals for the ID notch and OD notch respectively at the sensor location for the three core structures. The leakage magnetic fields from both the ID and OD notches are clearly seen with the use of ferrite core as compared to the air core structure. This observation is due to the concentration of magnetic field lines along the central axis of the tube by the ferrite core and hence reduction of compression of leakage fields due to direct magnetising fields. The intensity of the MFL signal is found to be highest in the ferrite core with flux guide structure for both the notches. This can be clearly seen from the B_a^{peak} amplitudes of the three core structures for both the notches (Figure 6.6). It can be noted that the signal B_a^{peak} amplitude increases by 4 times with the use of flux guide, in addition to the ferrite core. Hence, two bobbin coils wound on ferrite core together with flux guide structure has been chosen as the best magnetising unit for magnetisation of the SG tubes of hollow cylinder geometry.

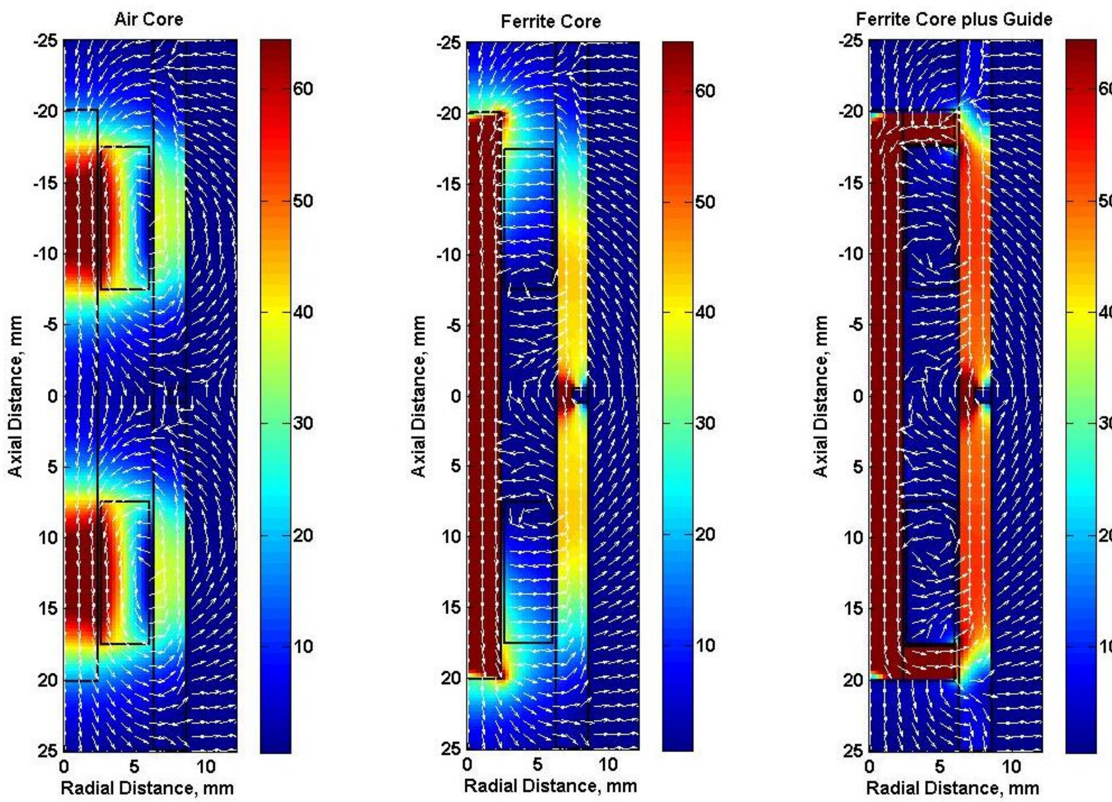

(a) (b) (c)

Figure 6.4 Surface and arrow plots of magnetic flux density from a 1.15 mm deep OD notch for (a) air core, (b) ferrite core and (c) ferrite core with flux guide.

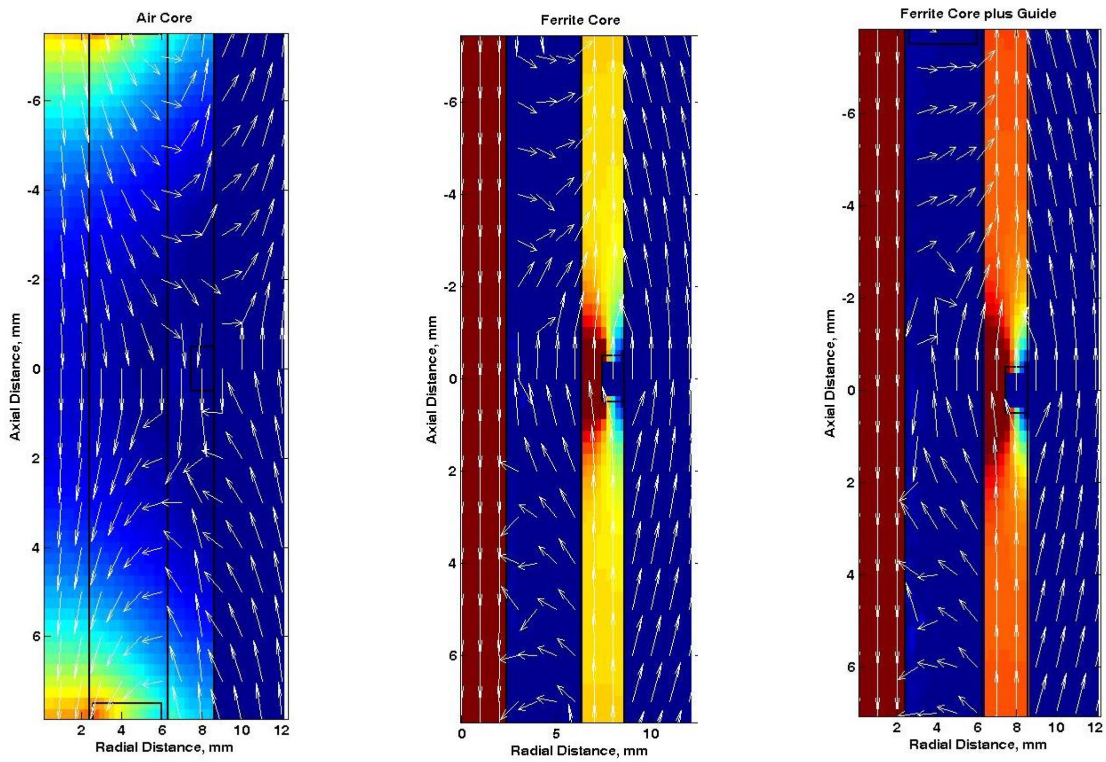

(d) (e) (f)

Figure 6.4 Surface and arrow plots of magnetic flux density from a 1.15 mm deep OD notch (near defect) for (d) air core, (e) ferrite core and (f) ferrite core with flux guide.

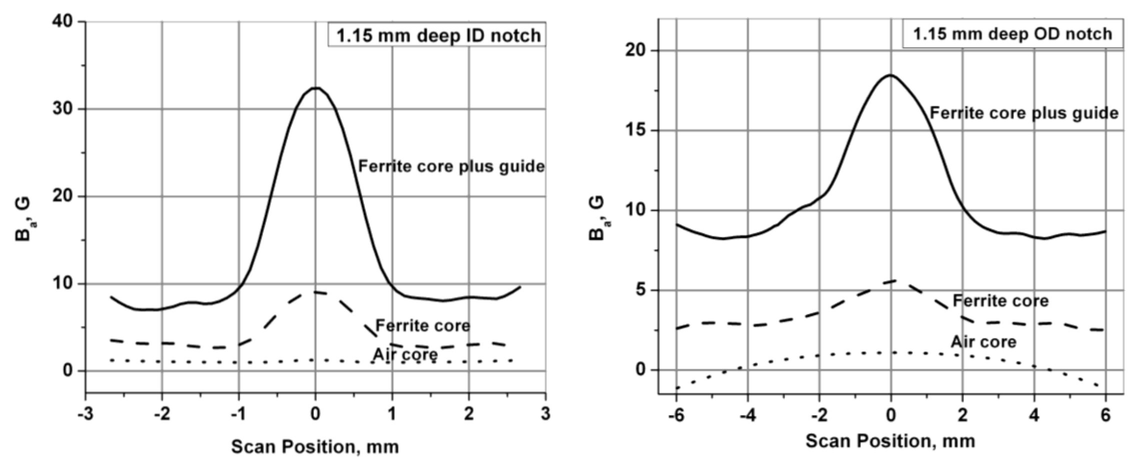

(a) (b)

Figure 6.5 Model predicted B_a component of MFL signals for (a) ID notch and (b) OD notch of three magnetising coil structures.

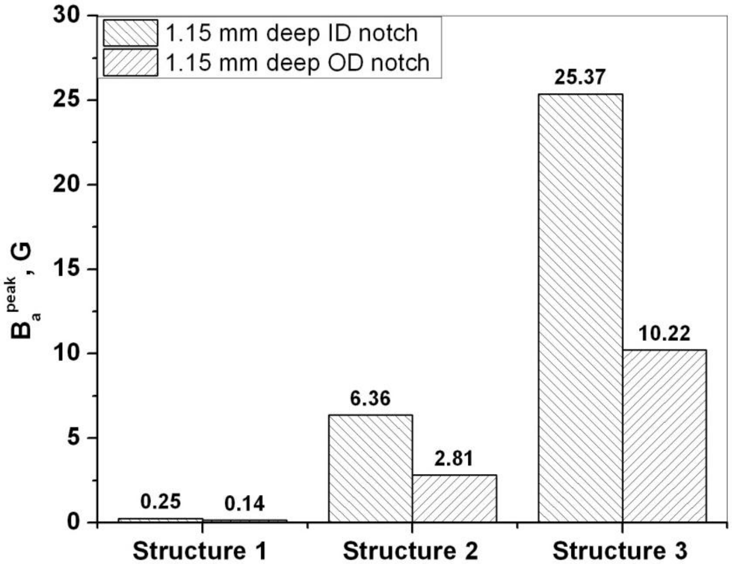

Figure 6.6 Model predicted B_a^{peak} amplitudes of MFL signals for ID and OD notches of three magnetising coil structures.

6.3.1 Optimization of Inter-coil Spacing

The inter-coil spacing (s_c) between the two bobbin coils is optimized for obtaining uniform axial magnetisation of the tube region between the two coils so that sufficient detectable magnetic fields were leaked out of the notch. The axial component of leakage fields is computed for various coil spacing of 15 mm to 40 mm in steps of 5 mm. The inter-coil spacing is optimized using B_a^{peak} amplitudes of the MFL signals for both ID and OD notches as shown in Figure 6.7(a). The B_a^{peak} amplitude of the MFL signal for ID notch is found to decrease with the increase in inter-coil spacing. This is primarily due to the reduction in magnetic field strength with the increase in inter-coil spacing of the coils. On the other hand, the B_a^{peak} amplitude of the MFL signal for OD notch is found to increase upto 25 mm spacing. At distances greater than 25 mm, the signal amplitude is seen decreased due to increase in magnetic reluctance with inter-coil spacing. Hence, a distance of 25 mm has been chosen as the optimum inter-coil spacing between the two bobbin coils for this technique.

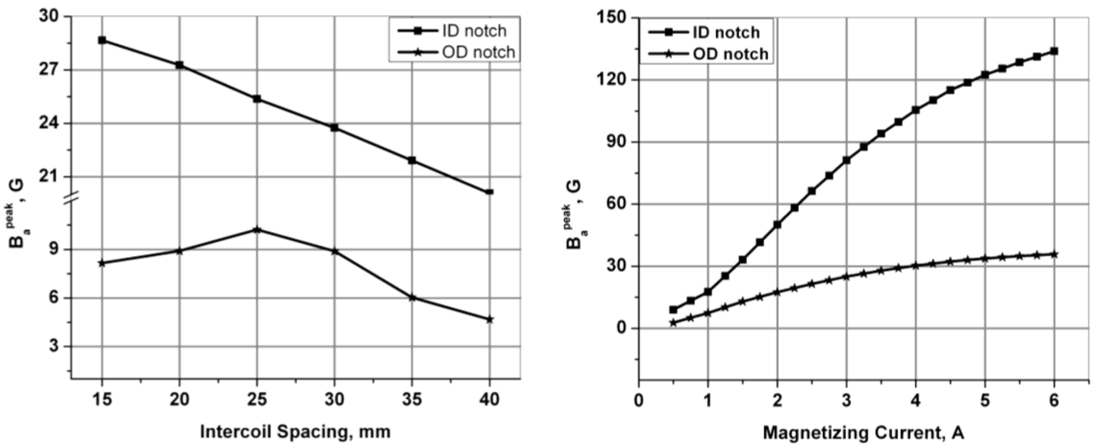

(a) (b)

Figure 6.7 Optimization of (a) inter-coil spacing between the two bobbin coils and (b) magnetising current.

6.3.2 Optimization of Magnetizing Current

The magnetising current is optimized to i) obtain sufficient detectable leakage magnetic fields from all the notches considered in the study, ii) avoid the overheating of the coils due to continuous current and iii) minimize the demagnetization requirement of the SG tube. Figure 6.7(b) shows B_a^{peak} amplitudes of the MFL signals as a function of magnetising current for both ID and OD notches. As can be seen, B_a^{peak} increases with the increase in magnetising current for both notches and starts the saturation magnetization of the SG tube at currents 5 A. However, the bobbin coils starts getting heated up at currents greater than 2.5 A. In order to enable inspection of the SG tubes for a longer duration without cooling the coils and to minimize the demagnetization requirement of the SG tube, the magnetizing current of 1.25 A is used. Experimental measurements have been made using these optimized magnetising coils in this technique.

6.4 Experimental Setup

The experimental setup used for the MFL measurements of SG tube using GMR sensor is shown in Figure 6.8(a). It consists of two bobbin coils, a variable DC power supply, a GMR sensor, a differential amplifier and a personal computer. The bobbin coils consisting of two circular coils of 68 turns each separated by 25 mm is used for axial magnetisation of the tube. The coil outer diameter is made 11.5 mm to fit inside the tube. Each coil has cross-sectional area of 10 x 3 mm^2 and wind on a 4.8 mm diameter ferrite core. The ferrite core acts as a magnetic flux guiding device by concentrating the magnetic field lines along central axis of the tube and hence, reduces the compression of leakage fields due to direct magnetising fields. The GMR sensor is kept at the middle of the bobbin coils as shown in Figure 6.8(b). The GMR bridge sensor (AAL002-02) is used in this study. The axial component of the leakage flux from defects in the tube is measured using the GMR sensor. Measurements are made by moving the GMR sensor and magnetisation coils together as a single unit inside the tube with a speed of 2 cm/s. A constant fill factor of 91.3% is maintained between the GMR sensor and the ID surface of tube to avoid physical damage of the sensor. In order to enhance the sensitivity of GMR sensor, its output is filtered and amplified 20 times using a low-noise differential amplifier. The amplified GMR sensor output is digitized using a 16 bit DAQ system and stored in the computer for subsequent analysis.

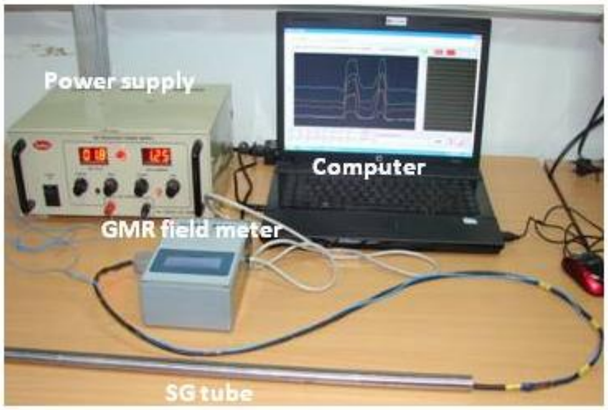

(a)

(b)

Figure 6.8 (a) Experimental setup for MFL testing of SG tube and (b) photograph of GMR sensor based MFL probe.

6.5 Reference Defects

The specimens used in this study are three straight SG tubes T1, T2 and T3 (length 1000 mm, OD 17.2 mm and WT 2.3 mm) with artificial reference defects. Localized defects are simulated by notches and flat bottom holes (FBH) introduced on the outer surface of the SG tubes T1 and T2 using EDM machining. Four circumferential notches (A, B, C and D) of length 5 mm, width 1 mm and different depths are machined on the outer side of tube T1. Four flat bottom holes (E, F, G and H) of diameter 2 mm and different depths are machined on the outer side of tube T2. Four through holes (I, J, K and L) of different diameters are also machined into the tube T3. The depths of EDM notches and FBHs and diameters of through holes measured by replica technique are given in Table 6.2.

Table 6.2 Depths of reference defects in SG tubes

S. No.	Tube No.	Defect	Defect type	Defect depth/diam., mm	% Wall thickness
1	T1	A	Notch	0.54	23.65%
2	T1	B	Notch	0.75	32.65%
3	T1	C	Notch	1.19	51.83%
4	T1	D	Notch	1.50	65.22%
5	T2	E	FBH	0.22	09.57%
6	T2	F	FBH	0.56	24.30%
7	T2	G	FBH	1.14	49.70%
8	T2	H	FBH	1.40	60.65%
9	T3	I	Through hole	1.08	100%
10	T3	J	Through hole	2.03	100%
11	T3	K	Through hole	2.77	100%
12	T3	L	Through hole	3.10	100%

6.6 Experimental Results

6.6.1 Localised Defects

The MFL signals of axial component of leakage fields of outer side circumferential notches viz. A, B, C and D in the tube T1 measured by the GMR sensor, after background removal, are shown in Figure 6.9(a). As can be observed, all the four circumferential notches can be detected. The signal amplitude for the shallowest notch A (0.54 mm deep, 23.65% WT) is approximately 2.9 times the background signals from notch-free regions. The SNR of the shallowest notch A (0.54 mm deep, 23.65% WT) is found to be 9.2 dB. As expected, the signal amplitude is found to increase with the increase in notch depth.

The MFL signals of axial component of leakage fields of flat bottom holes viz. E, F, G and H in the tube T2 are shown in Figure 6.9(b). The technique detected three FBHs F, G and H, except the shallowest FBH, E (0.22 mm deep, 9.57% WT). The signal amplitude of the hole, F (0.56 mm deep, 24.30% WT) in the tube is approximately 1.8 times the background signals from defect-free regions and its SNR turns out to be 5.1 dB. Thus, the optimization of the MFL technique together with the use of GMR sensors and differential amplifier enables to lower the minimum detectable depth from 40% WT hole in 2.77 mm thick ferromagnetic carbon steel tube [142] to 24% WT hole in 2.3 mm thick ferromagnetic SG tube in MFL technique. The signal amplitude increases with the increase in depth of holes.

The MFL signals of axial component of leakage fields of through holes viz. I, J, K and L in the tube T3, after background removal, are shown in Figure 6.9(c). Once again, the technique detected all the four holes. The SNR of the smallest hole, I (diameter 1.04 mm) in the tube is found to be approximately 6.8 dB.

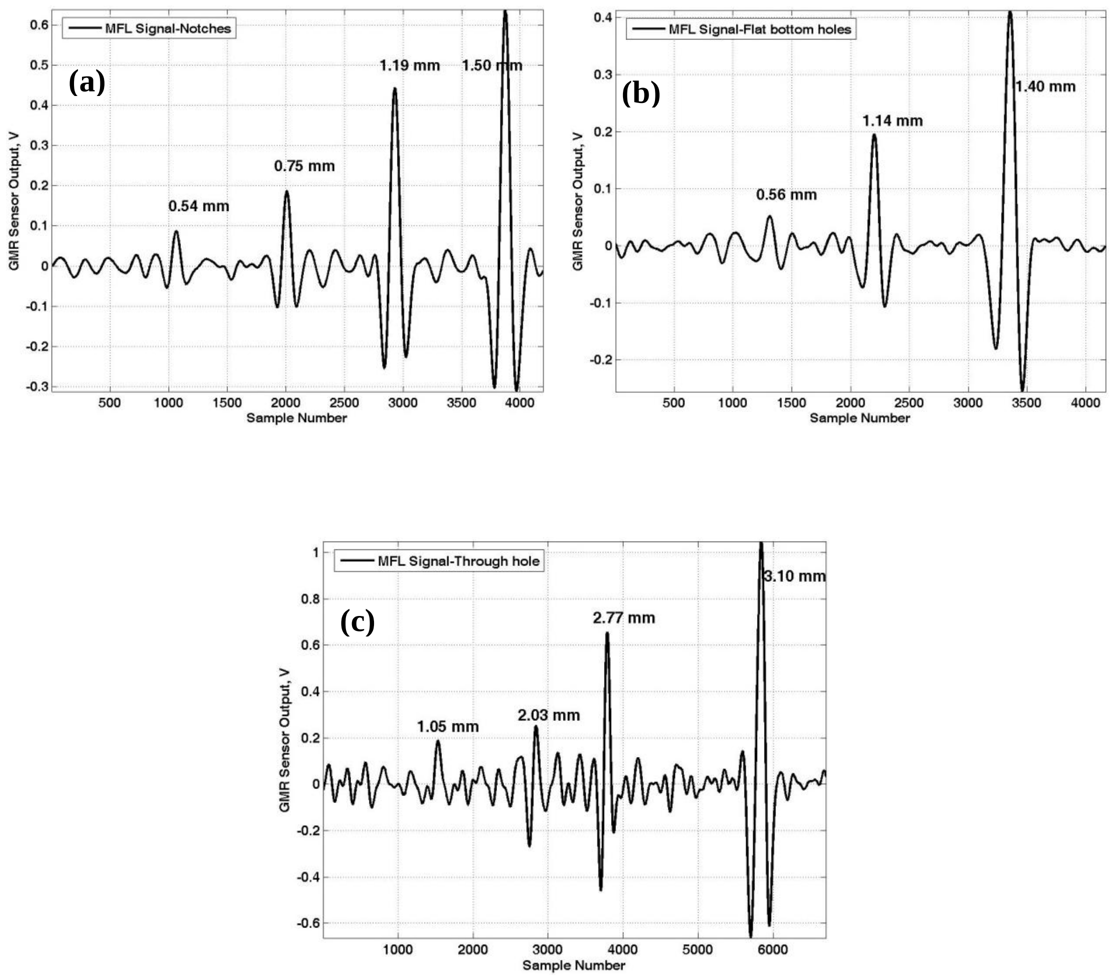

Figure 6.9 GMR sensor response for outer side (a) EDM circumferential notches, (b) flat bottom holes and (c) through holes in SG tube.

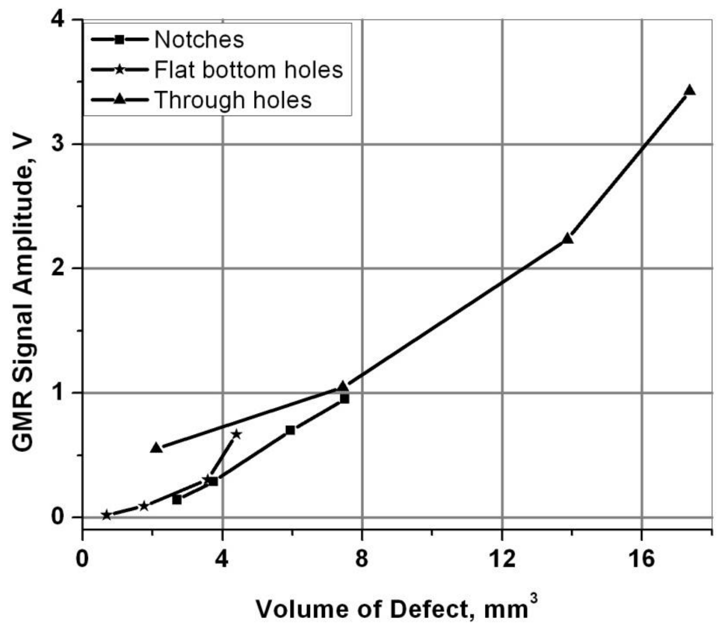

Figure 6.10 GMR sensor signal amplitude as a function of volume of defects.

In order to compare the detection sensitivity of the MFL technique for the three types of defects viz. notches, FBHs and through holes, peak amplitudes of MFL signals have been determined by taking the difference of peak and valley of MFL signals. The peak amplitudes of MFL signals of the three types of defects are plotted as a function of volume of defects, as shown in Figure 6.10. The peak amplitude increases almost linearly with increase in volume of defect in all type of defects. Among the three types of defects, the peak amplitude of through holes is found to be maximum for the similar volume of defects. This observation is attributed to the higher reluctance with 100% WT in through holes compared to the notches and FBHs and the MFL signal amplitude depends upon more on depth as compared to length and width of defects [100].

The optimized GMR based MFL technique can be used for ISI of the SG tubes as it enables reliable detection of OD defects in the SG tube. It is expected that the technique will detect ID defects with larger signals than OD defects as the field strength on the ID side is higher than OD side. The use of GMR sensors with low noise differential amplifier also enables to lower the minimum detectable depth of defects in tubes with lower IDT ratio that were previously considered undetectable. The technique does not require full saturation of the tube unlike in saturation eddy current technique. The instrumentation is less expensive and much simpler as compared to RFEC technique [146]. The high sensitivity of the technique is expected to enable effective detection of both ID and OD defects in small diameter ferromagnetic tubes.

6.6.2 Influence of Support Plate on MFL Signals

The influence of support plate (Figure 6.11a) on MFL signal has also been analyzed. Figure 6.11(b) shows the MFL signals of the 1.08 mm diameter hole with and without the support plate. As can be seen, the MFL signals of holes are not significantly influenced by the presence of support plate outside the SG tube. To verify the experimental observation, FE modeling has been carried out simulating the situation. Model predicted MFL signals of the hole with and without support plate is plotted together with the experimental result in Figure 6.11(b). As can be seen, there is a good agreement between the model predicted and experimental MFL signals. In both cases, no significant change in the MFL signals is observed by the presence of support plate. This is attributed to the non-magnetic (μ_r = 1.001) behavior of the Inconel-718 support plate resulting similar field contour lines in the tube with and without plate as shown in Figure 6.12(a) and 6.12(b) respectively. It can also be expected that the electrically conductive non-magnetic sodium deposits, if present, in the defective regions of the SG tubes will also not influence the defect sensitivity of the technique. This will avoid the use of multi-frequency excitation and associated signal and image processing techniques to remove the influence of support plate and sodium deposits on RFEC signals [112, 145]. Further, the MFL technique can be advantageously used to identify the support plate and sodium deposits by comparing to RFEC signals.

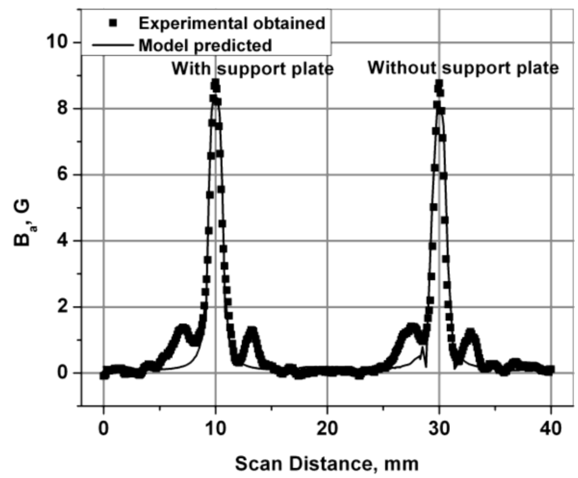

(a) (b)

Figure 6.11 (a) Photograph of the SG tube with support plate (Inconel-718) and (b) comparison of experimentally obtained and model predicted MFL signals for a 1.08 mm diameter hole in tube with and without the support plate.

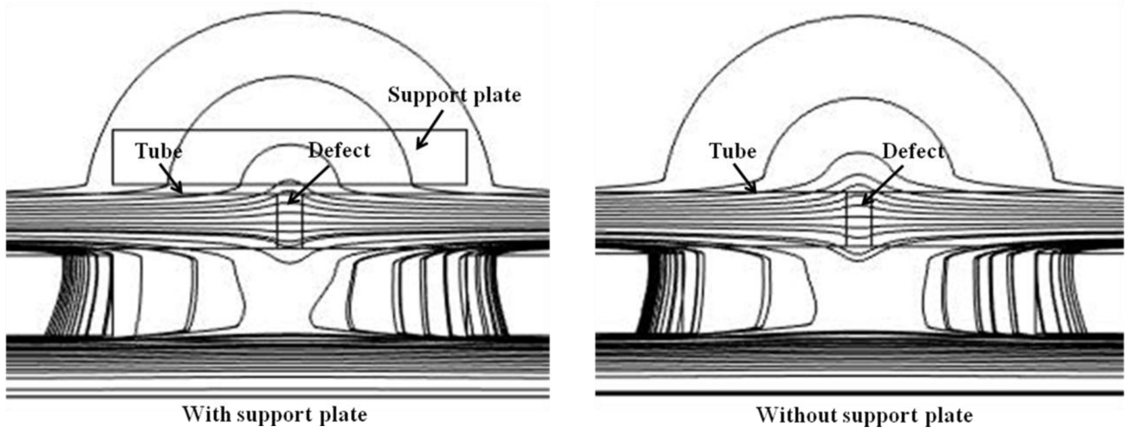

(a) (b)

Figure 6.12 Model predicted contour plots of magnetic flux density (a) with and (b) without the support plate.

6.6.3 Validation

The experimental MFL signals have been validated with the model predicted MFL signals. The experimentally obtained GMR signal amplitude of the circumferential notches (length 5 mm, width 1 mm and depths 0.54, 0.75, 1.19 and 1.50 mm) is compared with the model predicted signal amplitudes in Figure 6.13. A good agreement is seen between the trends of model predicted and experimental MFL signal amplitudes. In both the cases, the B_a^{peak} amplitude increases with the increase in notch depth. The model predicted B_a^{peak} amplitude values are within 20% of the experimental values. The deviation between the model and experimental values can be attributed to the flux concentration intrinsically present in the GMR sensor and magnetic anisotropy in the tube material.

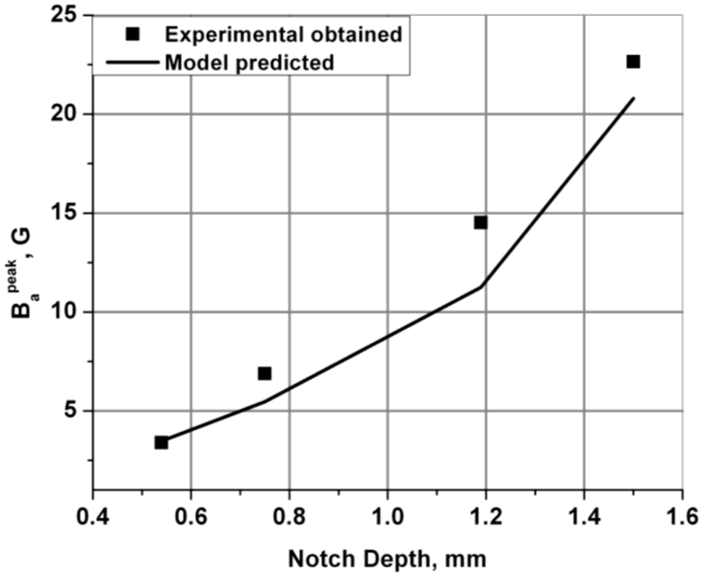

Figure 6.13 Comparison of experimentally obtained and model predicted MFL signal amplitude of circumferential notches.

6.7 Development of Flexible 5 Element GMR Array Sensors

In order to identify the number of GMR elements and locations of flexible GMR array sensors between the two bobbin coils, 3D-FE modeling has been performed. Figure 6.14(a) shows the model predicted B_a component of the magnetic flux density between the two bobbin coils. As can be seen, the magnetic flux density is nearly uniform for an optimum area of 36x13 mm^2 (dotted region in Figure 6.14a). This region can accommodate two arrays, each of 5 GMR sensors. Hence, a flexible array of 5 GMR sensors has been fabricated (Figure 6.14b) and used for imaging of defects in the tube. Each sensor element in the array has a common power input of 5 V, and the array has 5 differential outputs. The overall size of the sensor array is 34×9 mm^2. The centre-to-centre distance (pitch) between two consecutive sensors is 5.5 mm. The GMR sensors measure the B_a component of leakage flux from defects in the SG tube. The sensors' outputs are acquired and analyzed using a LabVIEW-based data acquisition system incorporating averaging and low pass filter to minimize noise.

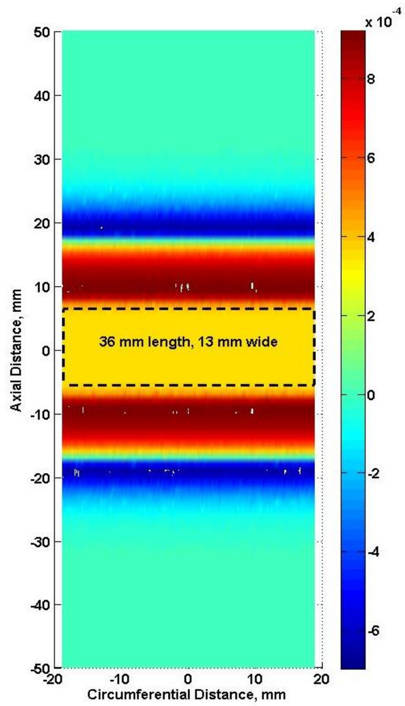

(a)

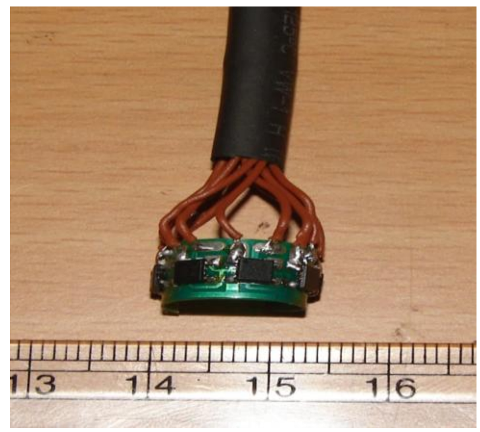

(b)

Figure 6.14 (a) Model predicted magnetic flux density between the two bobbin coils (b) the photograph of fabricated flexible array of 5 element GMR sensors.

The performance of the GMR array sensor based MFL probe has been evaluated by measuring the axial component of leakage fields from localized defects in the SG tube. Typical GMR array response of localized holes of diameter in the range of 1.1 mm to 3.1 mm is shown in Figure 6.15. The array sensor has reliably detected 1.1 mm diameter hole in the tube with SNR better than 5 dB. The GMR sensor output increases with the increase in diameter of holes.

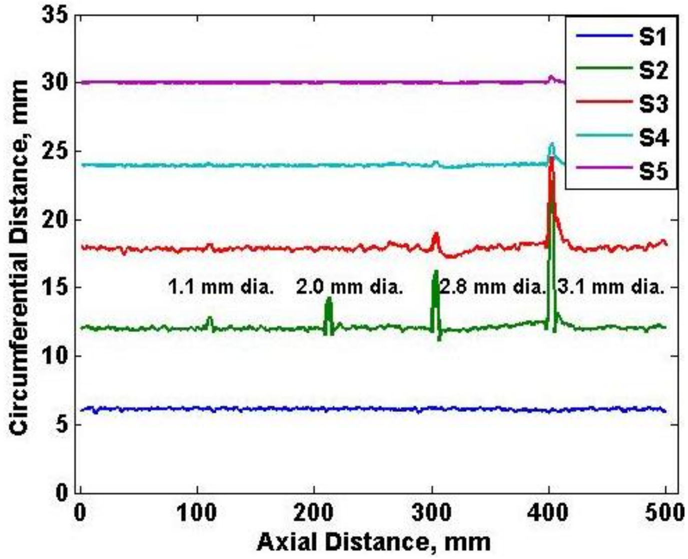

Figure 6.15 Response of 5 element GMR array sensor for through holes of 1.1, 2.0, 2.8 and 3.1 mm diameter.

6.8 Conclusions

- ✓ In this chapter, MFL technique comprising of specially designed bobbin coils wound on a ferrite core and GMR array sensors has been proposed for detection of localized defects in small diameter hollow cylindrical tubes such as SG tubes of PFBR. FE modeling has been performed to optimize the best structure of the bobbin coils based magnetising unit, number and location of GMR sensors used in the MFL technique.
- ✓ The optimized MFL technique is capable of detecting outer side 0.54 mm deep (23.65% WT) EDM circumferential notch and 0.56 mm deep (24.30% WT) flat bottom hole in the SG tube with a SNR better than 5 dB.
- ✓ The study confirms that the presence of support structures of the SG tube is not influenced on MFL signals.

- ✓ A flexible 5 element GMR array sensor has been fabricated and its performance has been found satisfactory, enabling fast detection of 1.1 mm holes in the SG tubes.

Chapter 7: Generalized Approach Proposed for Model Based Optimization

7.1 Comparative Performance of MFL Techniques for the Three Different Geometries

It is found from chapters 4, 5 and 6 that MFL techniques are different depending upon the geometry and accessibility of the components to be inspected. For optimization of the MFL techniques for three different geometries, the FE modeling based approach has been found to be effective. It enhances the detection sensitivity of the MFL techniques by optimizing the best configuration of magnetising and sensing units. However, the detection sensitivities of the MFL techniques are different for different geometry components. Table 7.1 shows the comparative performance of MFL techniques for the three different geometries. From the studies, it appears that yoke with sensor array unit will enable high sensitive detection of defects in all the three geometries by way of SNR, resolution and sub-surface detectability. However, it appears that the speed of testing is slow in the yoke magnetization compared to the coil based magnetizations.

Two important aspects of MFL technique viz. magnetising unit and sensor unit must be tailored to suit the geometry of the component. In the case of carbon steel plate of cuboid geometry, electromagnetic yoke of only one magnetising coil which is wound around its bow shows the best magnetising structure. For track ropes of solid cylindrical geometry with top side access, split type saddle coils is found to be optimal magnetising structure, although the Helmholtz coil provides excellent uniform axial magnetic fields for MFL inspection of ropes with full access. In the case of SG tubes of hollow cylindrical geometry, ferrite cored bobbin coils with the flux guide show the very good detectability compared to other coils.

The number and locations of GMR sensors depend upon the test geometry and area of coverage. Rigid array sensor is sufficient for cuboid geometry while flexible array sensors are necessary for curved surfaces and cylindrical geometries.

Table 7.1 Comparative performance of MFL techniques for the three different geometries

Aspect	**Cuboid**	**Solid Cylinder**	**Hollow Cylinder**
Magnetisation unit	Electromagnetic yoke	Saddle coils	Bobbin coils
Magnetisation field	Strong (~1.1 T)	Weak (~0.8 T)	Weak (~0.7 T)
Sensing unit	2D array of 4x4 GMR sensors	1D flexible array of 12 GMR sensors	1D flexible tandem arrays, each of 5 GMR sensors
Detectability	Surface notch: 0.5 mm deep Sub-surface notch: 1 mm deep located at 11 mm	Surface LF: 1 mm deep Surface LMA: 3 mm deep	OD notch: 0.5 mm deep Hole: 1 mm diameter
SNR (1 mm deep surface defect)	12 dB	7 dB	10 dB
Spatial resolution	2.5 mm	3.2 mm	3 mm
Imaging	Possible	Possible	Possible

7.2 Generalised Approach

Based on the experience gained from the study of model based optimization of MFL techniques for three different geometries viz. cuboid, solid cylinder and hollow cylinder, a generalized approach has been proposed. As the geometry of the objects are different and their dimensions vary, 50% WT deep defects are proposed as a guideline, in order to optimize the magnetizing unit and detectability by the GMR sensor. Figure 7.1 shows the flowchart of the proposed approach. The approach employed consists of the following steps:

i) For a given test geometry, select the magnetising unit by considering the accessibility and dimension of the test object.

ii) Simulate 50% WT deep defects in object and predict MFL signals

iii) Optimize each parameters of the magnetising unit to detect these defects, keeping saturation of GMR sensor in perspective.

iv) Optimize the number and location of array sensing unit by predicting uniform magnetic flux density between the two poles of magnetising unit.

v) Fine tuning the parameters based on the test conditions.

It may be noted that the magnetising unit and its optimum test parameter values depend upon the dimension of the object to be inspected. For example, the ferrite cored bobbin coils used for magnetization of hollow cylindrical geometry is limited to ID more than 12 mm and WT upto 6 mm. If the ID of the tube is less than 12 mm, the leakage field will be completely masked by the direct magnetizing field. Similarly, if the WT of the tube is more than 6 mm for relatively small ID tubes, the magnetization level would be quite small to detect defects.

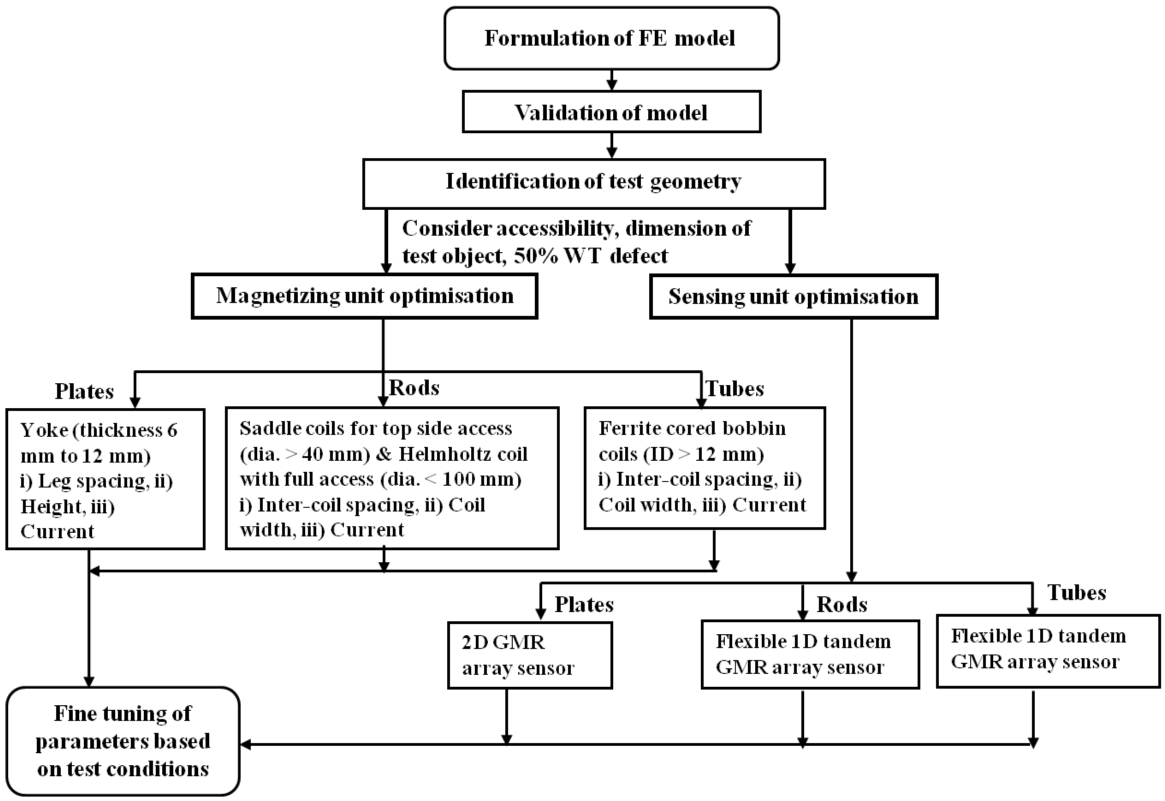

Figure 7.1 Flowchart of the generalized approach for optimization of MFL techniques.

Chapter 8: Conclusions

The present thesis reported finite element model based optimization of GMR array sensor based MFL techniques of ferromagnetic components for different geometries using FE modeling. The major observations made from the study are highlighted in this chapter.

This thesis has demonstrated the possibility of optimizing the MFL techniques for different geometries using FE modeling without extensive physical testing. The optimization approach is shown to be efficient and effective for high sensitivity detection of defects in ferromagnetic components.

MFL techniques are different depending upon the geometry and accessibility of the components to be inspected. In the case of carbon steel plate of cuboid geometry, MFL technique comprising of electromagnetic yoke (leg spacing 95 mm, height 75 mm, magnetizing current 4 A) with coil wound around the bow of the yoke and 2D rigid array of 4x4 GMR array sensor has found to be optimum. Using the model optimized parameters, an experimental MFL setup consisting of electromagnetic yoke, GMR sensor and selective amplifier has been developed for detection of defects in the plates. The GMR sensor based technique is capable of detecting a shallow surface notch of 0.93 mm depth and a sub-surface notch located at 11.07 mm below the measurement surface in 12 mm thick plate. A 2D array of 4x4 GMR sensors has been designed and fabricated for rapid imaging of the defects in the plate with the possibility to obtain spatial information of the defect.

On the study of inclined and interacting defects, it reveals that skewness is a better parameter for classification of inclined or non-inclined defects. It can classify the inclined (>10º inclination) notches with an error of about 10%. The B_x^{peak} amplitude appears to be a better parameter for classification of interacting or non-interacting defects.

For the first time, a split type saddle coils-GMR array sensor based MFL technique has been proposed for inspection of 64 mm diameter steel track ropes of solid cylindrical geometry with half (top) side access. The technique has been optimized using FE modeling for enabling reliable detection of both LF (depth 2 mm) and LMA type defects that form in the ropes. In addition, the technique is able to resolve flaws separated by a distance of more than 3.2 mm. Using the amplitude and FWHM of the MFL signals, it is possible to classify whether the flaw in the track rope is axial or circumferential. Using the FE model optimized parameters, a flexible GMR array sensor has been developed for fast detection of LF and LMA type defects in the steel track rope. The array sensor shows very good performance enabling fast detection and imaging of both types of defects in the track rope.

An MFL technique comprising of specially designed ferrite cored bobbin coils with flux guide and GMR array sensors has been proposed for detection of localized defects in small diameter steam generator tubes of PFBR. The inter-coil spacing of the bobbin coils is found to be optimum at 25 mm for 17.2 mm OD and 2.3 WT tubes. The experiment results reveal that the MFL technique is capable of detecting outer side 0.54 mm deep (23.65% WT) EDM circumferential notch and 0.56 mm deep (24.30% WT) flat bottom hole in the SG tube with a SNR better than 5 dB. It is also found that the support structures do not affect the MFL signals and this avoids the need for the use of additional techniques for processing RFEC signals. In addition, a flexible 5 element GMR array sensor has been fabricated based on the outcome of the FE modeling results and this has enabled detection and imaging of 1.1 mm holes in the SG tubes with a SNR of 7 dB, as compared to 5 dB by RFEC technique.

Based on the analysis of observations from the three different geometries, a generalized approach has been proposed for MFL NDE of ferromagnetic components.

Chapter 9: Future Work

The works presented in this thesis aim at generalization of model based optimization of MFL techniques for ferromagnetic components of different geometries. It details the optimization of GMR array sensor based MFL techniques for three different geometries and provides a generalized approach. However, the study is not exhaustive and further research is still needed to improve the performance of the MFL techniques. In the present research work, the MFL inspection system is assumed static. However, the system is moving with constant velocity and the velocity of MFL inspection system influences the shape and magnitude of MFL signal. Therefore, it would be beneficial to introduce the velocity term in equation (3.5) and solve to study the influence of velocity variations on MFL signals in different geometries.

As the DC MFL technique only relies on one measurement feature, i.e. the magnetic field leakage intensity, the technique provides limited information about the defects detected in terms of location and sizing. In order to enhance the information obtained from different depths in the testing component, the use of pulsed excitation (instead of DC) in the MFL technique may be beneficial. This may enable analysis of MFL signals in both time and frequency domains to obtain location and sizing of defects, especially in the thickness direction.

Although non-linearity of B-H characteristics has been considered in the present thesis, the accuracy of the model can be further enhanced by taking into account of the anisotropy of true wire strand of the rope.

The GMR array sensors used in the present thesis are on-chip sensors in which each GMR sensor is packaged with an IC chip. This reduces the spatial resolution of the MFL technique. In order to enhance the detection sensitivity and spatial resolution, off-chip GMR array sensors in which the sensors in the form of die mounted on the PCBs, are very attractive.

Another potential area of research is the development of multi-dimensional GMR array sensors for measuring all the 3 components of leakage fields from defects in ferromagnetic components. It will also be interesting to develop automatic intelligent image fusion algorithms for the measured 3 components to enable effective detection of defects and interpretation of data.

Automated detection, classification and accurate sizing of defects in ferromagnetic components using MFL techniques is still an open area of research. Inversion algorithms, artificial neural networks, genetic algorithms, etc. may be useful for this purpose.

References

[1] "Nondestructive testing handbook, second edition: Vol. 10, Nondestructive testing overview", Columbus, OH: American Society for Nondestructive Testing, 1996.

[2] S. S. Udpa and P. O. Moore, "Nondestructive testing handbook", Vol. 5- Electromagnetic testing, ASNT 3rd Edition, 2004.

[3] D. E. Bray and R. K. Stanley, "Nondestructive evaluation, a tool for design, manufacturing, and service", McGraw-Hill, 1989.

[4] P. J. Shull, "Nondestructive evaluation: theory, techniques and applications", Marcel Dekkar, Inc., New York, 2002.

[5] B. Raj, T. Jayakumar and M. Thavasimuthu, "Practical nondestructive testing", Third Edition, Narosa Publishing House, New Delhi, 2007.

[6] B. P. C. Rao, "Practical eddy current testing", Narosa Publishing House, New Delhi, 2007.

[7] J. Blitz, "Electrical and magnetic methods of nondestructive testing", Adam Hilger publication, 1991.

[8] W. Lord, "Electromagnetic methods of nondestructive testing", Gordon and Breach Science Publishers, London, 1985, 175-304.

[9] D. J. Lovejoy, "Magnetic particle inspection: a practical guide", Chapman & Hall, 1993.

[10] D. C. Jiles, "Review of magnetic methods for nondestructive evaluation (Part 2)", *NDT International*, 23 (2), 1990, 83-92.

[11] P. Ramuhalli, L. Udpa, and S. S. Udpa, "Electromagnetic NDE signal inversion by function-approximation neural networks", *IEEE Trans. Magn*., 38 (6), 2002, 3633-3642.

[12] V. Lunin, V. Barat and D. Podobedov, "Neural network-based crack parameterization using wavelet preprocessing MFL signal", *Review of Progress in Quantitative Nondestructive Evaluation,* Vol. 20, ed. by D. O. Thompson and D. E. Chimenti.

[13] D. L. Atherton, "Magnetic inspection is key to ensuring safe pipelines," *Oil Gas J*, 87 (32) 1989, 52-61.

[14] N. Kasai, K. Sekine and H. Maruyama, "Non-destructive evaluation method for far-side corrosion type flaws in oil storage tank bottom floors using the magnetic flux leakage technique", *Journal of the Japan Petroleum Institute*, 46 (2), 2003, 126-132.

[15] J. B. Nestleroth and T. A. Bubenik, "Magnetic flux leakage (MFL) technology for natural gas pipeline inspection: The Gas Research Institute", February 1999. (http://www.battelle.org/pipetechnology/ MFL/MFL98Main.html).

[16] Md. Afzal and S. Udpa, “Advanced signal processing of magnetic flux leakage data obtained from seamless gas pipeline”, *NDT &E International*, 35, 2002, 449-457.

[17] F. I. Al-Naemi, J. P. Hall and A. J. Moses, “FEM modeling techniques of magnetic flux leakage-type NDT for ferromagnetic plate inspections”, *Journal of Magnetism and Magnetic Materials*, 304, 2006, 790-793.

[18] D. H. Saunderson, “The MFL tank floor scanner - a case history”, *IEE colloquium on non-destructive evaluation*, 1988.

[19] N. R. Pearson, M. A. Boat, R. H. Priewald, M. J. Pate, J. S. D. Mason, “Practical capabilities of MFL in steel plate inspection”, *Proc. 18th World Conference on Nondestructive Testing*, 16-20 April 2012, Durban, South Africa.

[20] Z. Liu, Y. Kang, X. Wu and S. Yang, “Study on local magnetisation of magnetic flux leakage testing for storage tank floors”, *Insight*, 45 (5), 2003, 328-331.

[21] H. R. Weischedel and R. P. Ramsey, “Electromagnetic testing, a reliable method for the inspection of wire ropes in service”, *NDT International*, 22 (3), 1989, 155-161.

[22] W. Hong-yao, H. Gang and T. Jie, ‘Research on detection device for broken wires of coal mine-hoist cable’, *Journal of China University Mining & Technology*, 17 (3), 2007, 376-381.

[23] E. Kalwa and K. Piekarski, ‘Design of Hall-effect sensors for magnetic testing of steel ropes’, *NDT International*, 22 (5), 1987, 295-301.

[24] W. Stumm, “Tube testing by electromagnetic NDT methods”, *Nondestructive Testing*, 7, 1974, 251.

[25] F. Förster, “Nondestructive inspection of tubing and round billets by means of leakage flux probes”, *British Journal of NDT*, 19, 1977, 26.

[26] S. Xiao-chun, H. Song-ling and Z. Wei, “Optimization of the magnetic circuit in the MFL inspection system for storage-tank floors”, *Russian Journal of Nondestructive Testing*, 43 (5), 2007, 326-331.

[27] D. C. Jiles, “Introduction to magnetism and magnetic materials”, Chapman & Hall Publishing, 1994.

[28] M. Katoh, N. Masumoto, K. Nishio and T. Yamaguchi, “Modeling of the yoke-magnetisation in MFL-testing by finite elements”, *NDT & E International*, 36, 2003, 479-486.

[29] Ch. Ravi Kumar, B. P. C. Rao, T. S. Abhilash, G. Rajaram, T. Jayakumar and B. Raj, “Generic HEMT structure wafer Hall-magnetic sensors for magnetic flux leakage imaging

for NDE of magnetic steels", *Proc. of Int. Conf. on Materials for Advanced Technologies*, Singapore, July 2007.

[30] G. S. Park and E.S. Park, "Improvement of the sensor system in magnetic flux leakage-type nondestructive testing (NDT)", *IEEE Trans. Magn.*, 38 (2), 2002, 1277-1280.

[31] B. P. C. Rao, T. Jayakumar, 'Discontinuity characterization using electromagnetic methods', *Journal of Nondestructive Testing & Evaluation*', 1 (2), 2002, 23-29.

[32] H.-J. Krausea and M.v. Kreutzbruck, "Recent developments in SQUID NDE", *Physica C*, 368, 2002, 70-79.

[33] R. J. P. Bain, G. B. Donaldson, S. Evanson, G. Hayward, in: H. D. Hahlbohm, H. Lubbig (Eds.), SQUID'85, *Proc. 3rd International Conference on Superconducting Quantum Devices*, deGruyter, Berlin, 1985, 841-846.

[34] Y. Li, J. Wilson and G. Y. Tian, "Experiment and simulation study of 3D magnetic field sensing for magnetic flux leakage defect characterization", *NDT & E International*, 40, 2007, 179-184.

[35] J. Wilson and G. Y. Tian, "3D magnetic field sensing for magnetic flux leakage defect characterization", *Insight*, 48 (6), 2006, 357-359.

[36] L. Chen, P.W. Que, and T. Jin, "A giant-magnetoresistance sensor for magnetic-flux-leakage nondestructive testing of a pipeline", *Russian Journal of Nondestructive Testing*, 41 (7), 2005, 462-465.

[37] W. S. Singh, B. P. C. Rao, S. Vaidyanathan, T. Jayakumar and Baldev Raj, "Detection of leakage magnetic flux from near-side and far-side defects in carbon steel plates using giant-magnetoresistive sensor", *Measurement Science and Technology*, 19, 2008, 015702 (8pp).

[38] W. Cui, S. Huang, W. Zhao and J. F. Burd, "The effect of defect location on the finite element modeling of defect MFL fields", *Insight*, 48 (7), 2006, 402-405.

[39] R. K. Amineh, N. K. Nikolova, J. P. Reilly and J. R. Hare, "Characterization of surface-breaking cracks using one tangential component of magnetic leakage field measurements", *IEEE Trans. Magn.*, 44 (4), 2008, 516-524.

[40] R. E. Beissner, G. A. Matzkanin and C. M. Teller, "NDE applications of magnetic leakage field methods, a state-of-the-art survey", *NTIAC Report 80-1*, Southwest Research Institute, January 1980.

[41] R. S. Popovic, J. A. Flanagan and P. A. Besse, "The future of magnetic sensors", *Sensors and Actuators A*, 56, 1996, 39-55.

[42] A. C. Bruno, "SQUIDs and inverse problem techniques in nondestructive evaluation of metals", *Brazilian Journal of Physics*, 31 (4), 2001, 587-596.

[43] W. G. Jenks, S. S. H. Sadeghi, and J. P. Wikswo, “SQUIDS for nondestructive evaluation”, *J. Phys. D: Appl. Phys.*, 30, 1997, 293-323.

[44] A. C. Bruno, R. Schifini, G. S. Khuner, C. H. Barbosa, J. P. Wikswo and C. S. Camerini, “New magnetic techniques for inspection and metal-loss assessment of oil pipelines”, *Journal of Magnetism and Magnetic Materials*, 226, 2001, 2061-2062.

[45] H. Hauser, G. Stangl, W. Fallmann, R. Chabicovsky and K. Riedlin, “Magnetoresistive Sensors (Online)”, http://educypedia.karadimov.info/library/Hauser.pdf

[46] www.nobelprize.org/nobel_prizes/physics/laureates/2007/advanced-physicsprize2007.pdf

[47] M. N. Baibich, J. M. Broto, A. Fert, F. Petroff, P. Eitenne, G. Creuzet, A. Friederich and J. Chazelas, “Giant magnetoresistance of (001) Fe/ (001) Cr magnetic superlattices”, *Phys. Rev. Lett.*, 61 (21), 1988, 2472-2475.

[48] G. Binasch, P. Grünberg, F. Saurenbach and W. Zinn, “Enhanced magneto-resistance in Fe-Cr layered structures with antiferromagnetic interlayer exchange”, *Physical Review B*, 39 (7), 1989, 4828-4830.

[49] S. Solomon, “Sensors handbook”, 2^{nd} Edition, McGrawHill, 2009.

[50] C. H. Smith and R. Schneider, “Magnetorestive sensors for nondestructive evaluation”, *10th SPIE International Symposium*, Nondestructive Evaluation for Health Monitoring and Diagnostics, Conference 5770, 2003.

[51] Introduction to NVE GMR sensors, www.nve.com

[52] B. Wincheski, J. Simpson, M. Namkung, D. Perey, E. Scales and R. Louie, “Development of giant magneto-resistive inspection system for detection of deep fatigue cracks under airframe fasteners”, *Review of Progress in Quantitative NDE*, (AIP Conf. Proc.) 21A, 2001, 1007-1014.

[53] A. Yashan, W. Bisle and T. Meier, “Inspection of hidden defects in metal-metal joints of aircrafts structures using eddy current technique with GMR sensor array”, *9th European Conf. Non-Destructive Testing*, Berlin, September 2006.

[54] Z. Zeng, Y. Deng, X. Liu, L. Udpa, S. S. Udpa, B. E. C. Koltenbah, R. H. Bossi and G. Steffes, “EC-GMR data analysis for inspection of multilayer airframe structures”, *IEEE Trans. Magn.*, 47 (12), 2011, 4745-4752.

[55] K. Chomsuwan, S. Yamada, M. Iwahara, “Bare PCB inspection system with SV-GMR sensor eddy-current testing probe”, *IEEE Sens. J.,* 7, 2007, 890-896.

[56] B. Sasi, B. P. C. Rao, S. Thirunavukkarasu, T. Jayakumar and B. Raj, “Eddy current-GMR sensor for nondestructive detection of deep-surface defects”, *Proc. of Nat. Sym. on Physics and Technology of Sensors*, Mumbai, Feb. 2007, 273-275.

[57] A. Yashan, R. Becker and A. Klein, "Detection of small inclusions in thin steel sheets by magnetic flux leakage technique", Proc. *8th Eur. Conf. Non-Destructive Testing,* Barcelona, June, 2002.

[58] M. Kreutzbruck, A. Neubauer, M. Pelkner and V. Reimund, "Adapted GMR Array used in Magnetic Flux Leakage Inspection", *Proc. 18th World Conference on Nondestructive Testing,* 16-20 April 2012, Durban, South Africa.

[59] T. Chady and G. Psuj, "Data fusion from multidirectional remanent flux leakage transducers for NDT of stress and fatigue loaded steel samples", *IEEE Trans. Magn.*, 44, 2008, 3285-3288.

[60] S. M. Saxby, "Magnetic testing of iron", *Engineering,* 5, 1868, 297.

[61] I. J. Flaherty, "History of magnetic particle testing", *Materials Evaluation,* 8 (8), 1990, 1010-1022.

[62] A. V. deForest, "Magnetic testing of iron and steel", *Iron & Steel,* May 1932, 170.

[63] F. B. Doane, "Magnaflux inspection for cracks and seams", *Iron Age,* Sept. 1933.

[64] T. Zuschlag, "Method and apparatus for testing rails or the like", US Patent 1, 896, 737, 1933.

[65] G. Dobmann, "Magnetic leakage flux techniques in NDT a state-of-the-art survey of the capabilities for defect detection and sizing", *Electromagnetic Methods of Nondestructive Testing,* Edited by William Lord, Ed. Gordon and Breach, 1985, 71-95.

[66] C. Mandache and L. Clapham, "A model for magnetic flux leakage signal predictions", *J. Phys. D: Appl. Phys.*, 36, 2003, 2427-2431.

[67] J. Hwang, J. Jun, S. Choi, Ch. Kim, K. Ogawa and J. Lee, "A study of magnetic charge per unit area of dipole model for the NDE", *Key Engineering Materials,* 353-358, 2007, 2371-2374.

[68] N. N. Zatsepin and V. E. Shcherbinin, "Calculation of the Magnetostatic Field of Surface Defects. I. Field Topography of Defect Models", *Defektoskopiya,* 5, 1966, 50-59.

[69] V. E. Shcherbinin and A. I. Pashagin, "Fields of defects on the inner and outer surfaces of a tube during circular magnetisation", *Sov. J. NDT.,* 8, 1972, 134.

[70] V. E. Shcherbinin and A. I. Pashagin, "Influence of the extension of a defect on the magnitude of its magnetic field", *Sov. J. NDT.,* 8, 1972, 441.

[71] V. E. Shcherbinin and A. I. Pashagin, "Effect of the boundaries of the specimen on the defect field", *Defektoskopiya,* 2, 1976, 85-89.

[72] I. A. Novikova and N. V. Miroshin, "Investigation of the fields of artificial open flaws in a uniform constant magnetic field", *Defectoskopia,* 4, 1973, 95-101.

[73] F. Förster, "Nondestructive inspection by the method of magnetic leakage fields", *Defektoskopiya*, 11, 1982, 3-25.

[74] F. Förster, "Theoretische and experimentelle Ergebnisse des magnetischen Streuflusserfahrens'', *Materialprufung*, 23, 1981, 372-378.

[75] Y. Zhang, K. Sekine and S. Watanable, "Magnetic leakage field due to sub-surface defects in ferromagnetic specimens'', *NDT & E International*, 28 (2), 1995, 67-71.

[76] C. Edwards and S. B. Palmer, "The magnetic leakage field of surface-breaking cracks", *J. Phys. D: Appl. Phys.*, 19, 1986, 657-673.

[77] D. Minkov, T. Shoji, "Method for sizing of 3-D surface breaking flaws by leakage flux", *NDT & E International*, 31 (5), 1998, 317-324.

[78] D. Minkov, J. Lee and T. Shoji, "Study of crack inversions utilizing dipole model of a crack and Hall element measurements", *Journal of Magnetism and Magnetic Materials*, 217, 2000, 207-215.

[79] S. Lukyanets, A. Snarskii, M. Shamonin, V. Bakaev, "Calculation of magnetic leakage field from a surface defect in a linear ferromagnetic material: an analytical approach", *NDT & E International*, 36, 2003, 51-55.

[80] S. M. Dutta, F. H. Ghorbel and R. K.Stanley, "Dipole modeling of magnetic flux leakage", *IEEE Trans. Magn.*, 45 (4), 2009, 1959-1965.

[81] S. M. Dutta, F. Ghorbel and R. Stanley, "Simulation and analysis of 3-D magnetic flux leakage," *IEEE Trans. Magn.*, 45 (4), 2009, 1966-1972.

[82] B. Bruder, "Magnetic leakage fields calculated by the method of finite differences", *NDT International*, 18 (6), 1985, 353-358.

[83] D. L. Atherton, and M. G. Daly, "Finite element calculations of magnetic flux leakage detector signals", *NDT International*, 20, 1987, 235-238.

[84] R. Palanisamy and W. Lord, "Finite element modeling of electromagnetic NDT phenomena", *IEEE Trans. Magn.*, Mag-15 (6), 1979, 1479-1481.

[85] N. Normann, F. J. Borgermann and H. H. Mende, "Simple boundary element method for three dimensional magnetostatic problems", *IEEE Trans. Magn.*, Mag-21 (3), 1985, 1235-1239.

[86] K. Bruce, "A hybrid magnetic field solver using a combined finite element/boundary element field solver", *Proc. UK magnetic society conference. Advanced electromagnetic modelling & CAD for industrial application*; February 19, 2003, 1-8.

[87] B. C. Cretu, O. Mihalache, G. Preda, F. Hantila, Z. Chen and K. Miya, "2D and 3D simulations of MFL signals for non-linear magnetic materials", *Applied Electromagnetics III, Japan Society of Applied Electromagnetics and Mechanics*, 2001, 37-40.

[88] X. Liang, Z. Zhiwei, S. Balasubramaniam, L. Udpa, "Element-free galerkin method for static and quasi-static electromagnetic field computation", *IEEE Trans. Magn.,* 40 (1), 2004, 12-20.

[89] Y. Li, G. Y. Tian, Steve Ward, "Numerical simulation on magnetic flux leakage evaluation at high speed", *NDT &E International,* 39, 2006, 367-373.

[90] Z. Zakaria, M. S. Mansor, A. H. Jahidin, M. S. Azlan and R. A. Rahim, "Simulation of magnetic flux leakage analysis using FEMM software", *Proc. IEEE Symposium on Industrial Electronics and Applications (ISIEA 2010)*, October 3-5, 2010, Penang, Malaysia, 481-486.

[91] W. Cui, S. Huang, W. Zhao and J. F. Burd, "The effect of defect location on the finite element modeling of defect MFL fields", *Insight*, 48 (7), 2006, 402-405.

[92] Z. Huang and P. Que, "Three modeling methods in MFL testing", *17th World Conference on Nondestructive Testing*, 25-28 Oct 2008, Shanghai, China.

[93] J. H. Hwang and W. Lord, "Finite element modeling of magnetic field-defect interactions", *ASTM Journal of Testing & Evaluation*, 3 (1), 1975, 21-25.

[94] W. Lord and J. H. Hwang, "Defect characterization from magnetic leakage fields", *British J. NDT.,* 19, 1977, 14-18.

[95] W. Lord, J.M. Bridges, W. Yen and R. Palanisamy, "Residual and active leakage fields around defects in ferromagnetic materials", *Material Evaluation*, 36, 1978, 47.

[96] D. L Atherton, and W. Czura, "Finite element calculations on the effects of permeability variation on magnetic flux leakage signals", *NDT International*, 20, 1987, 239-241.

[97] D. L. Atherton, "Finite element calculations and computer measurements of magnetic flux leakage patterns for pits", *British Journal of Nondestructive Testing*, 30 (3), 1988, 159-162.

[98] N. Ida, W. Lord, "3-D Finite Element Predictions of Magnetostatic Leakage Fields", *IEEE Trans. Magn.*, Mag-19 (5), 1983, 2260-2265.

[99] H. Zuoying, Q. Peiwen, C. Liang, "3D FEM analysis in magnetic flux leakage method", *NDT & E International,* 39, 2006, 61-66.

[100] F. Ji, Ch. Wang, S. Sun and W. Wang, "Application of 3-D FEM in the simulation analysis for MFL signals", *Insight*, 51 (1), 2009, 32-35.

[101] L. Chen, P. Que, Z. Huang and T. Jin, "Three-dimensional finite element analysis of magnetic flux leakage signals caused by transmission pipeline complex corrosion", *Journal of the Japan Petroleum Institute*, 48 (5), 2005, 314-318.

[102] V. Babbar and L. Clapham, "Modeling the effects of pit corner geometry on magnetic flux leakage signals", *Research in Nondestructive Evaluation*, 17, 2006, 161-175.

[103] W. Mao, L. Clapham, David L. Atherton, "Effects of alignment of nearby corrosion pits on MFL", *NDT &E International*, 36, 2003, 111-116.

[104] R. C. Ireland, C. R. Torres, "Finite element modeling of a circumferential magnetizer", *Sensors and Actuators A*, 129, 2006, 197-202.

[105] S. Yang, Y Sun, L. Udpa, S. S. Udpa and W. Lord, "3D simulation of velocity induced fields for nondestructive evaluation application", *IEEE Trans. Magn.*, 35 (3), 1999, 1754-1756.

[106] D. Zhiye, R. Jiangjun, P. Ying, Y. Shifeng, Z. Yu, G. Yan and L. Tianwei, "3-D FEM simulation of velocity effects on magnetic flux leakage testing signals", *IEEE Trans. Magn.*, 44 (6), 2008, 1642-1645.

[107] S. Leonard and D. L. Atherton, "Calculations of the effects of anisotropy on magnetic flux leakage detector signals", *IEEE Trans. Magn.*, 32 (3), 1996, 1905-1909.

[108] K. S. Ryu, D. L. Atherton and L. Clapham, "Effect of pit geometry and bulk stress on near- and far-side calculated MFL signals", *J. Phys. D: Appl. Phys.*, 35, 2002, 2693-2697.

[109] V. Babbar, B. Shiari and L. Clapham, "Mechanical damage detection with magnetic flux leakage tools: modeling the effect of localized residual stresses", *IEEE Trans. Magn.*, 40 (1), 2004, 43-49.

[110] V. Babbar, J. Bryne and L. Clapham, "Mechanical damage detection using magnetic flux leakage tools: modeling the effect of dent geometry and stresses", *NDT &E International*, 38, 2005, 471-477.

[111] M. Katoh, K. Nishio and T. Yamaguchi, "FEM study on the influence of air gap and specimen thickness on the delectability of flaw in the yoke method", *NDT & E International*, 33, 2000, 333-339.

[112] G. S. Park, P. W. Jang and Y. W. Rho, "Optimal design of a non-destructive testing system to maximize magnetic flux leakage", *Journal of Magnetics*, 6 (1), 2001, 31-35.

[113] G. S. Park and E. S. Park, "Improvement of the sensor system in magnetic flux leakage-type nondestructive testing", *IEEE Trans. Magn.*, 38 (2), 2002, 1277-1280.

[114] D. Mackintosh, M. Schmidt, C. Claveria, T. Carey and G. Moorhouse, "Magnetic design of a flux leakage assembly for pipes", *Materials Evaluation*, 2005, 329-334.

[115] E. Norouzi and H. Ravanbod, “Optimization of the flux distribution in magnetic flux leakage testing”, *Insight,* 51 (10), 2009, 563-567.

[116] S. Thirunavukkarasu, B. P. C. Rao, T. Jayakumar and Baldev Raj, “Techniques for processing remote field eddy current signals from bend regions of steam generator tubes of prototype fast breeder reactor”, *Annals of Nuclear Energy*, 38, 2011, 817-824.

[117] J. Jin, “The finite element method in electromagnetic”, *John Wiley & Sons*, Inc. Publication, New York, 2002.

[118] M. V. K. Chari and S. J. salon, “Numerical methods in electromagnetism”, *Academic Press,* 2000.

[119] W. Lord, “Applications of numerical field modeling to electromagnetic methods of nondestructive testing”, *IEEE Trans. Magn*., Mag-19 (6), 1983, 2437-2442.

[120] N. Ida, “Numerical modeling for electromagnetic non-destructive evaluation”, Chapman & Hall, California, 1995.

[121] L. Udpa, G. Katragadda and W. Lord, “Finite element modeling and defect characterization for gas transmission pipelines”, *Proc. of 14th World Conference on Non-destructive Testing*, India, December 8-13, 1996, 269-274.

[122] J. P. A. Bastos and N. Sadowski, “Electromagnetic modeling by finite element methods”, Marcel Dekker, Inc. publisher, New York, 2003.

[123] I. S. Duff, A. M. Erisman and J. K. Reid, “Direct methods for sparse matrices, Clarendon Press, Oxford, 1986.

[124] A. Greenbaum, “Iterative methods for solving linear systems”, *SIAM*, Philadelphia, 1997.

[125] COMSOL: Multiphysics modeling and simulation, *http://www.comsol.com.*

[126] J. A. Straton, “Electromagnetic theory”, McGraw-Hill, New York, 1941.

[127] N. R. Pearson, M. A. Boat, R. H. Priewald, M. J. Pate and J. S. D. Mason, “A study of MFL signals from a spectrum of defect geometries”, *18th World Conference on Nondestructive Testing*, 16-20 April 2012, Durban, South Africa

[128] N. B. Cameron, “Recommended practice for magnetic flux leakage inspection of atmospheric storage tank floors”, *Health and safety executive UK*, 2006.

[129] A. R. Ramirez, J. S. D. Mason and N. Pearson, “Experimental study to differentiate between top and bottom defects for MFL tank floor inspections”, *NDT & E International,* 42, 2009, 16-21.

[130] V. F. Muzhitskii and D. A. Kudryavtsev, “Some problems in determining the optimum sizes of magnetizing systems based on permanenet magnets”, *Russian Journal of Nondestructive Testing*, 40 (2), 2004, 124-129.

[131] "Engineering statistics handbook", April 2012, http://www.itl.nist.gov/div898/handbook/eda/section3/eda35b.htm.

[132] C. Mandache, B. Shiari and L. Clapham, "Defect separation considerations in magnetic flux leakage inspection", *Insight,* 47 (5), 2005, 269-273.

[133] D. Basak, "Performance comparison of drive ropes in a cable belt conveyor system using an NDT technique", *Insight,* 51 (8), 2009, 439-441.

[134] A. S. Mironenko and V. V. Sukhorukov, "Non-destructive testing of steel wire ropes in Russia", *Insight*, 40 (6), 1998, 395-397.

[135] H. R. Weischedel, "The inspection of wire ropes in service: a critical review", *Materials Evaluation*, 43, 1985, 1592-1605.

[136] N. Sumyong, A. Prateepasen and P. Kaewtrakulpong, "Influence of scanning velocity and gap distance on magnetic flux leakage measurement", *ECTI Transactions on Electrical Engineering, Electronics and Communications*, 5 (1), 2007, 118-122.

[137] C. Jomdecha and A. Prateepasen, "Design of modified electromagnetic main-flux for steel wire rope inspection", *NDT & E International*, 42, 2009, 77-83.

[138] E. Kalwa and K. Piekarski, "Design of inductive sensors for magnetic testing of steel ropes", *NDT International*, 20 (6), 1987, 347-353.

[139] S. C. Chetal, V. Balasubramaniyan, P. Chellapandi, P. Mohanakrishnan, P. Puthiyavinayagam, C. P. Pillai, S. Raghupathy, T. K. Shanmugham and C. Sivthanu Pillai, "The design of the prototype fast breeder reactor", *Nuclear Engineering and Design*, 236, 2006, 852-860.

[140] B. Raj, S. L. Mannan, P. R. Vasudeva Rao and M. D. Mathew, "Development of fuels and structural materials for fast breeder reactors", *Sadhana,* 27 (5), 2002, 527-558.

[141] C. V. Dodd, W. E. Deeds and L. D. Chitwood, "Eddy current inspection of ferromagnetic materials using pulsed magnetic saturation, *Material Evaluation*, 46 (12), 1988, 1592-1597.

[142] H. M. Sadek, "NDE techniques for the examination of heat exchangers and boiler tubes – principles, advantages and limitations", *Insight,* 48 (3), 2006, 181-183.

[143] K. Krzywosz and G. Dau, "Comparison of electromagnetic techniques for nondestructive inspection of ferromagnetic tubing", *Materials Evaluation,* 48 (1), 1990, 42-45.

[144] D. D. Mackintosh, D. L. Atherton, T. R. Schmidt and D. E. Russell, "Remote field eddy current for examination of ferromagnetic tubes", *Materials Evaluation*, 54 (6), 1996, 652-657.

[145] S. Thirunavukkarasu, B. P. C. Rao, S. Vaidyanathan, T. Jayakumar and Baldev Raj, “Influence of sodium deposits in steam generator tubes on remote field eddy current signals”, *International Journal of Pressure Vessels and Piping*, 85 (4), 2008, 211-218.

[146] Mark J. Bergander, “NDT Solution: Flux Leakage Examination of Ferrous Heat Exchanger Tubing”, *Materials Evaluation*, 44 (7), 1986, 811-812.

[147] Y. Gotoh and N. Takahashi, “Three-dimensional FEM analysis of electromagnetic inspection of outer side defects on steel tube using inner coil”, *IEEE Trans. Magn.*, 43 (4), 2007, 1733-1736.

[148] Y. Gotoh, H. Fujioka and N. Takahashi, “Proposal of electromagnetic inspection method of outer side defect on steel tube with steel support plate using optimal search coils”, *IEEE Trans. Magn.*, 47 (5), 2011, 1006-1009.

[149] K. Krzywosz and J. L. Cagle, “Comparison of three electromagnetic NDE procedures using realistic feedwater heater mock-ups”, *Materials Evaluation*, 51 (2), 1993, 132-139.